Science Advances
AAAS

Supplementary Materials for

A reference tissue atlas for the human kidney

Jens Hansen *et al.*

Corresponding author: Evren U. Azeloglu, evren.azeloglu@mssm.edu; Ravi Iyengar, ravi.iyengar@mssm.edu; Matthias Kretzler, kretzler@med.umich.edu; Olga G. Troyanskaya, ogt@genomics.princeton.edu

Sci. Adv. **8**, eabn4965 (2022)
DOI: 10.1126/sciadv.abn4965

The PDF file includes:

Figs. S1 to S20
Legends for tables S1 to S13
Supplemental Information
References

Other Supplementary Material for this manuscript includes the following:

Tables S1 to S13

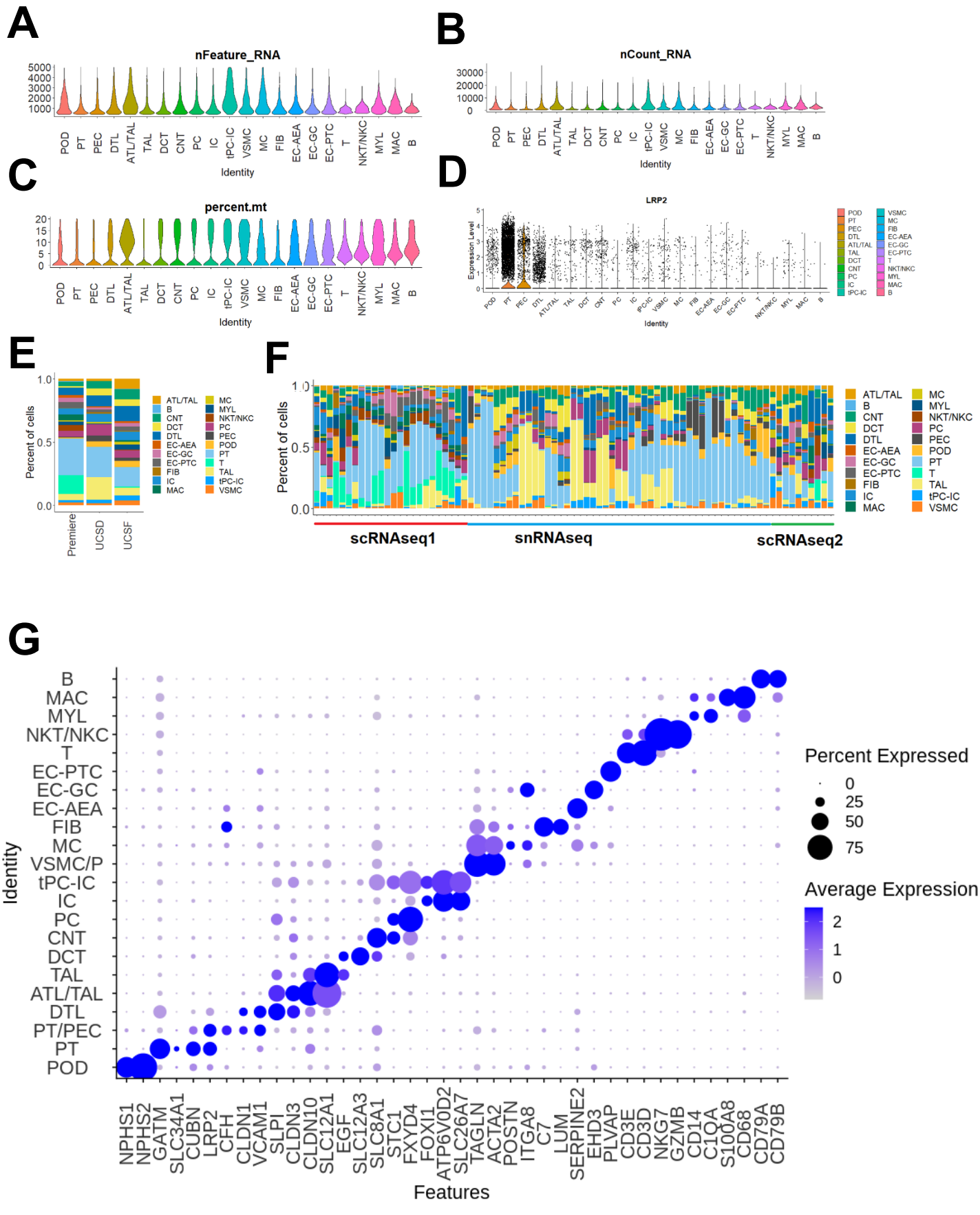

Supplemental Figure S1

Supplemental Figure S1: Quality control of the integrated cluster analysis. (A) Violin plot showing the mitochondrial read percentage per cell in the single cell/nuclei integrated object. **(B)** Violin plot showing the number of genes per cell in the single cell/nuclei integrated object. **(C)** Violin plot showing the number of UMIs per cell in the single cell/nuclei integrated object. To exclude potential doublets from the analysis, cells with greater than 5000 genes per cell were filtered out. **(D)** Feature plot showing the expression of UMOD in all cells from the two single cell and one single nucleus data from the three tissue interrogation sites. UMOD is one of the highly abundant mRNA expressed in loop of Henle that is usually present as ambient mRNA due to cell breakage while dissociation. The feature plots show specific high expression of UMOD in loop of Henle cells. The ambient mRNA expression of UMOD in other cell types is relatively low. **(E)** Plot showing the proportion of cells in the cell types identified in the two single cell and the single nuclei data from the three tissue interrogation sites. **(F)** Plot showing the proportion of cells in the cell types identified in each of the sample studied for single /single nuclei assays. **(G)** Dot plot of cell type specific marker genes.

A

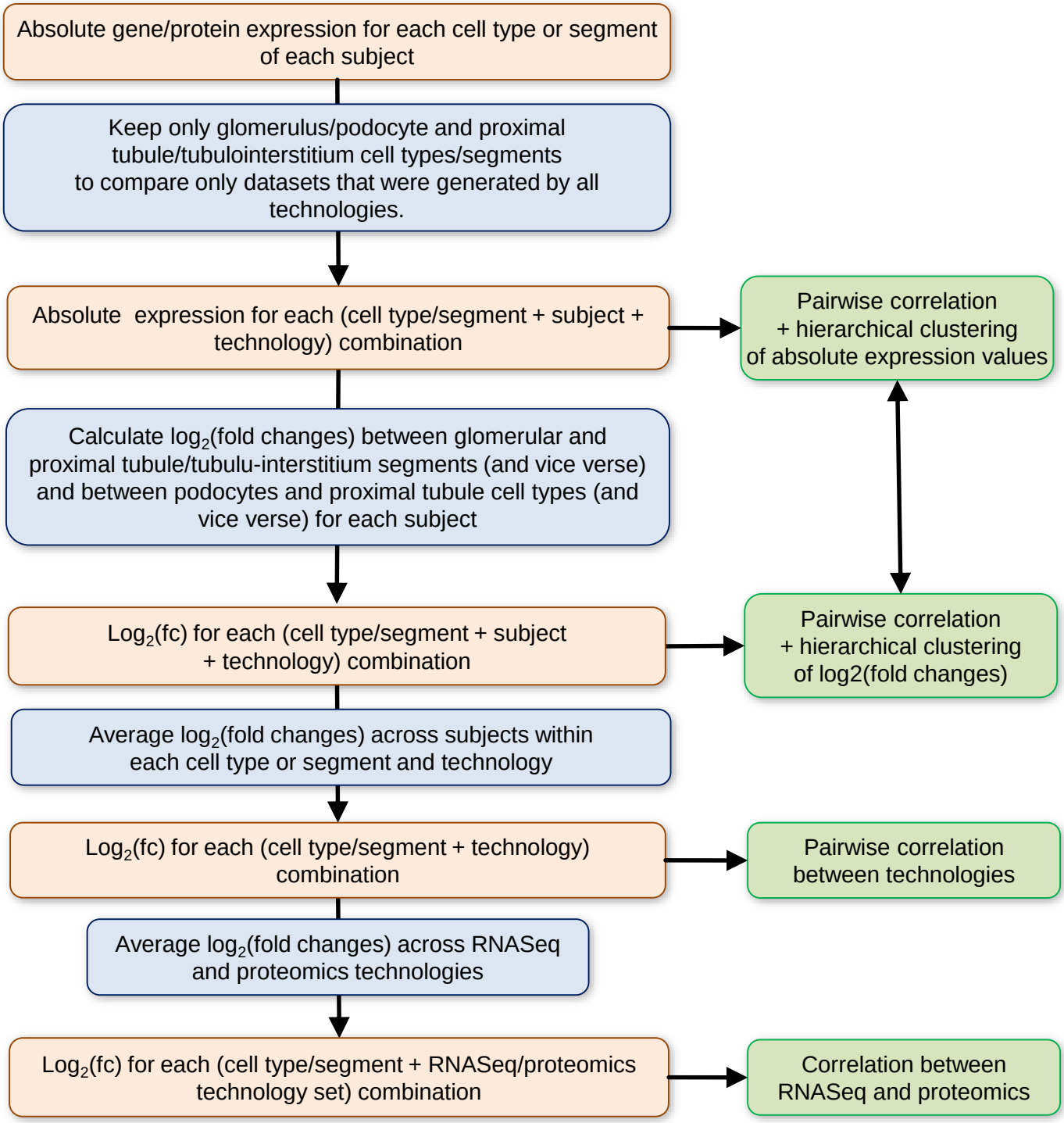

Supplemental Figure S2

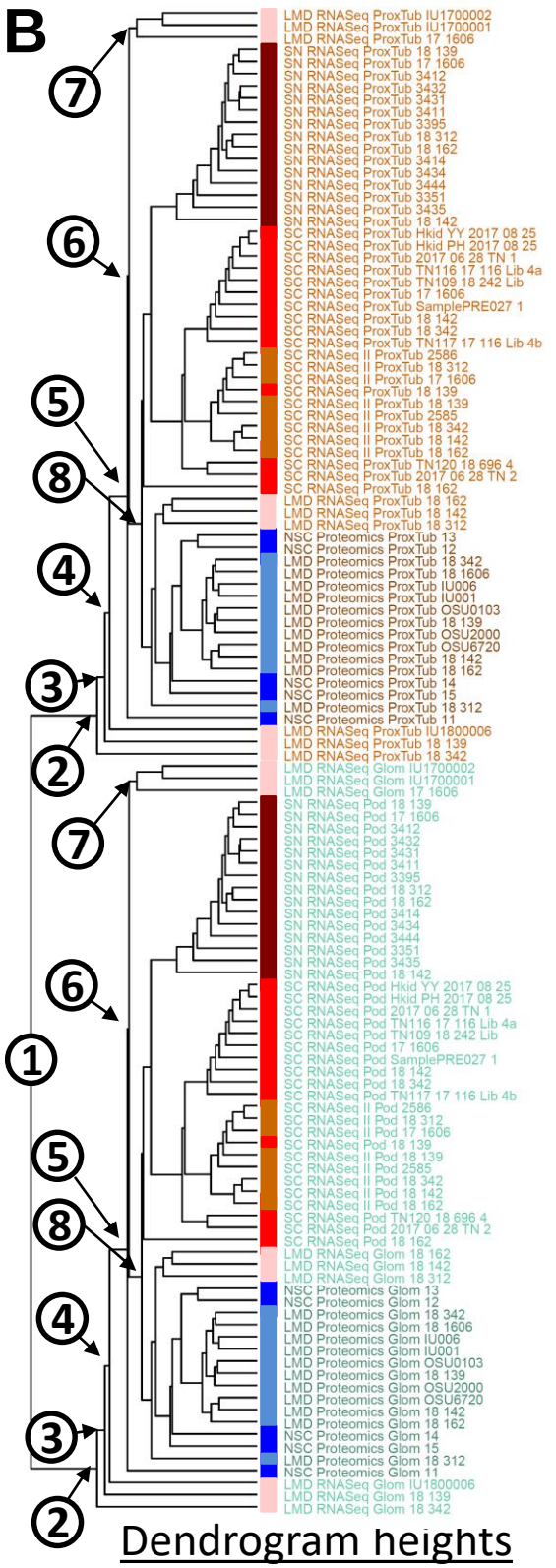

Dendrogram heights

①	0.684	⑤	0.392
②	0.484	⑥	0.387
③	0.461	⑦	0.363
④	0.446	⑧	0.349

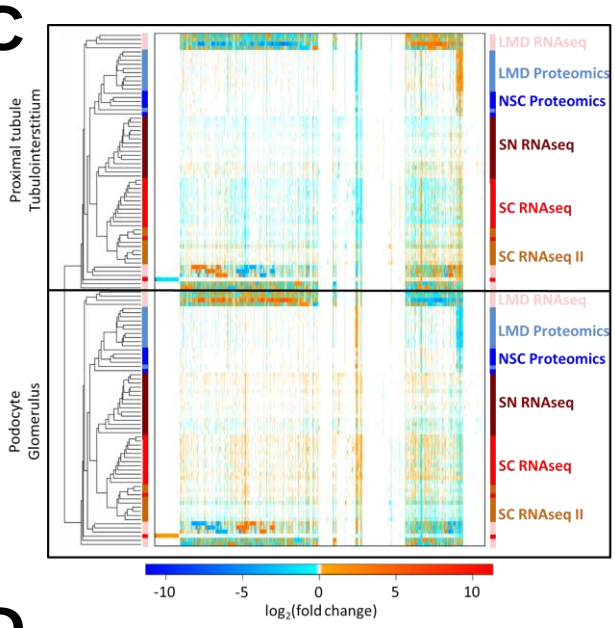

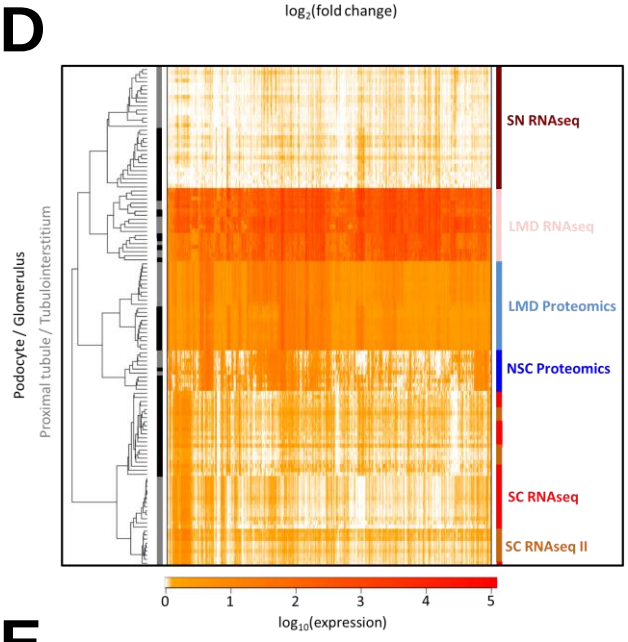

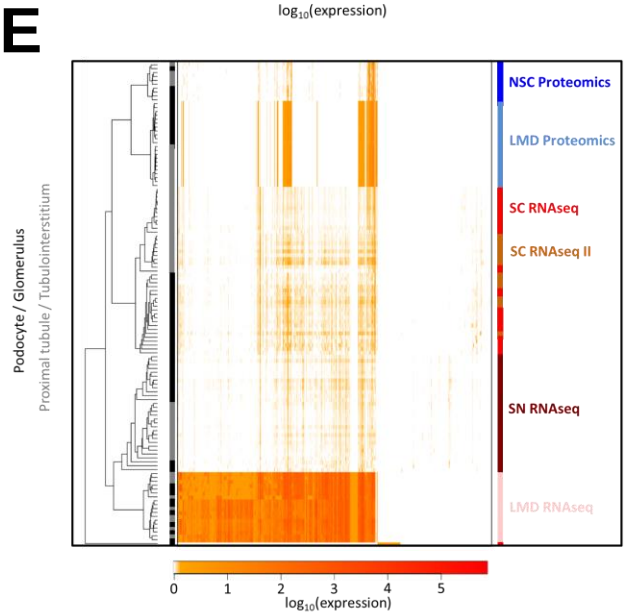

Supplemental Figure S2

Supplemental Figure S2: Cross-platform comparison of gene and protein expression. (A) Pipeline for correlation analysis across different omics technologies. See methods for details. **(B)** Clustering dendrogram that was obtained after hierarchical clustering of pairwise correlations between all samples based on the $\log_2$(fold changes) after removal of those genes and proteins that are not consistently detected. Numbers document heights of branches at indicated positions in the dendrogram. See figure 2C for associated heatmap. **(C)** Hierarchical clustering of pairwise correlation coefficients between all samples based on the $\log_2$(fold changes) without removal of those genes and proteins that are not consistently detected across all assays also groups the samples by anatomical region and not technology. In contrast, pairwise correlation and hierarchical clustering based on logarithmized absolute expression values groups samples by technology, **(D)** with or **(E)** without removal of the not consistently detected genes and proteins.

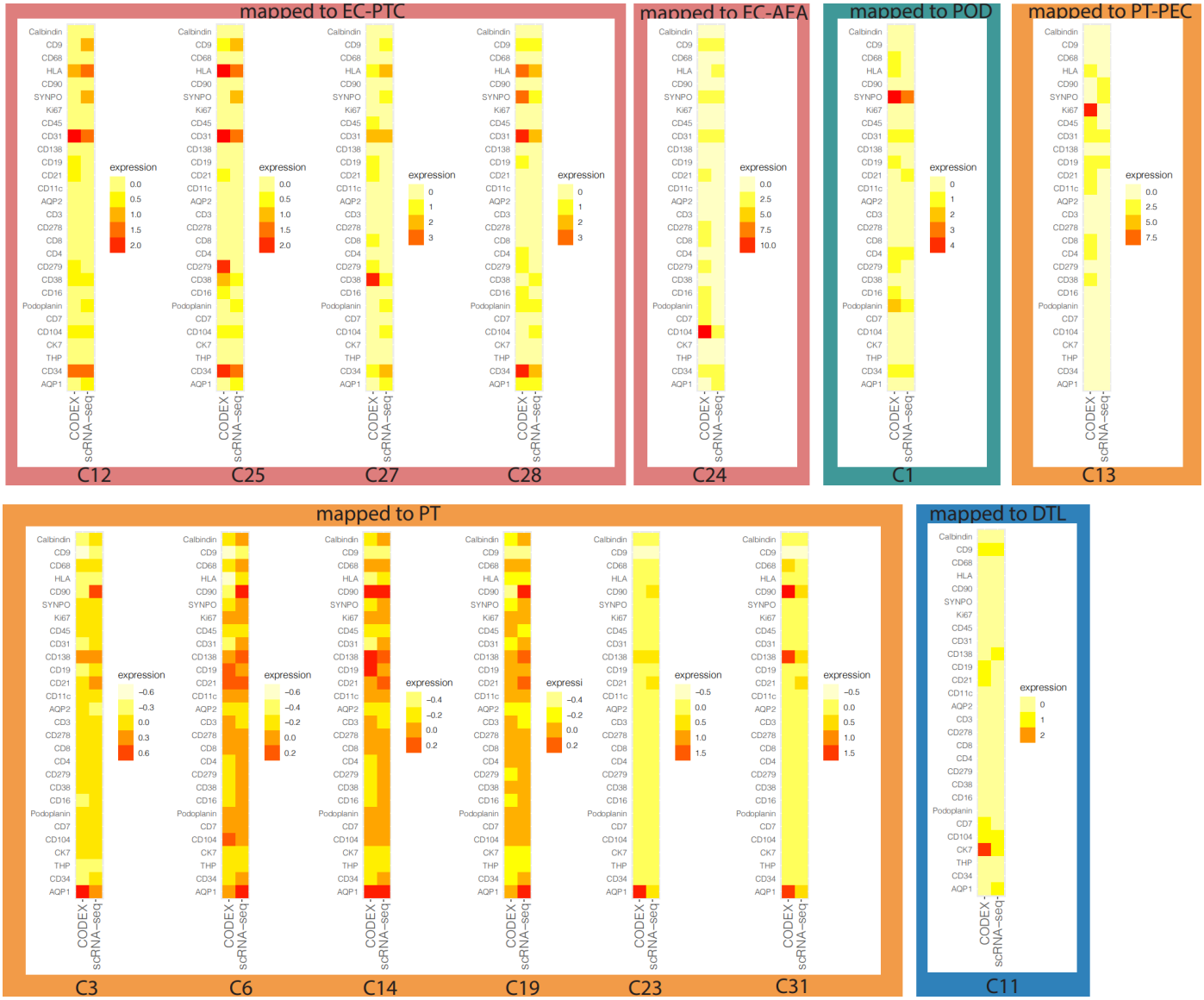

Supplemental Figure S3

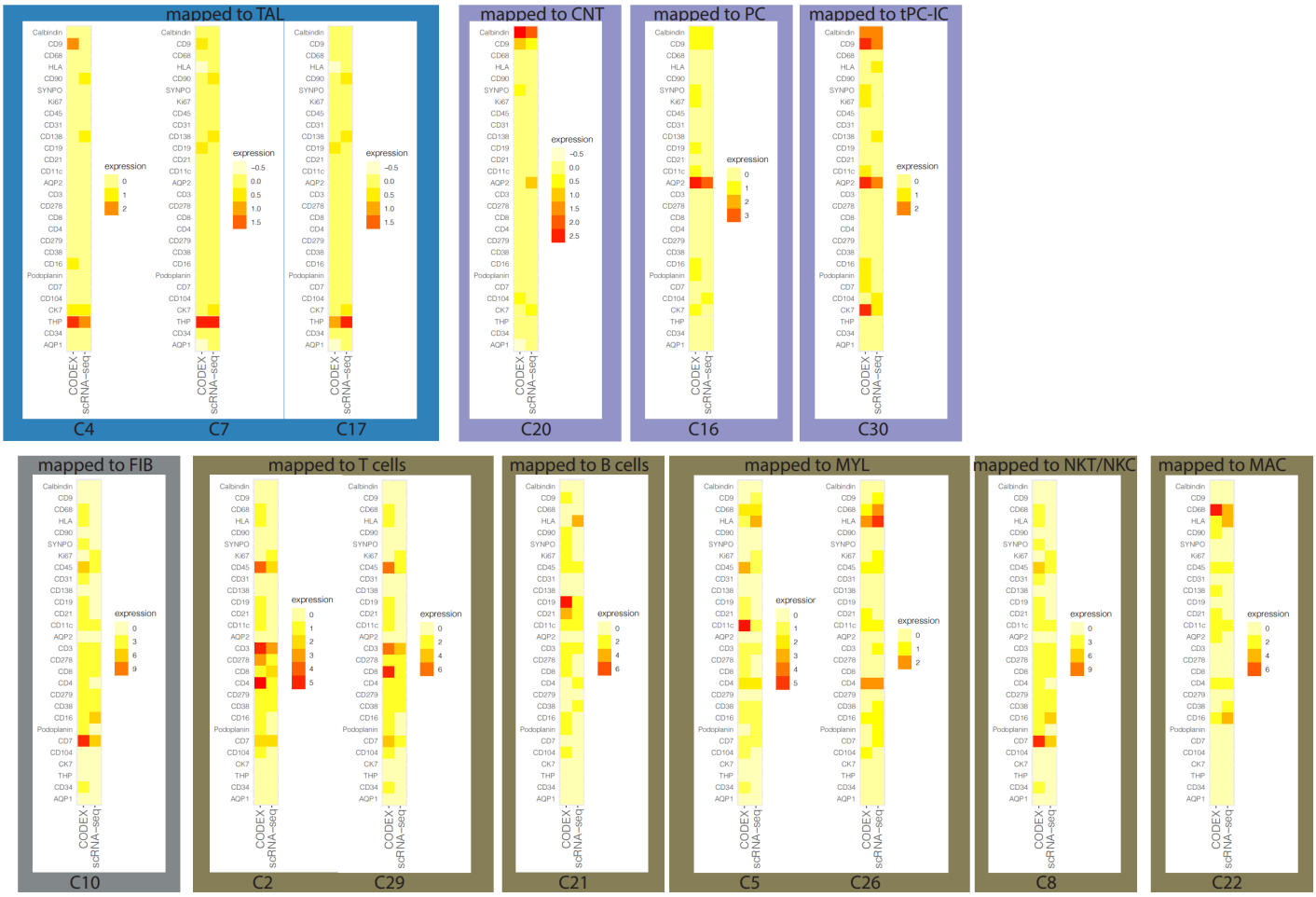

Supplemental Figure S3

Supplemental Figure S3: Comparison of expression across CODEX clusters and mapped cell-type specific transcriptomic profiles. For each CODEX cluster, we show its scaled average expression profile together with the scaled average expression profile of the mapped cell-type specific transcriptomic profile.

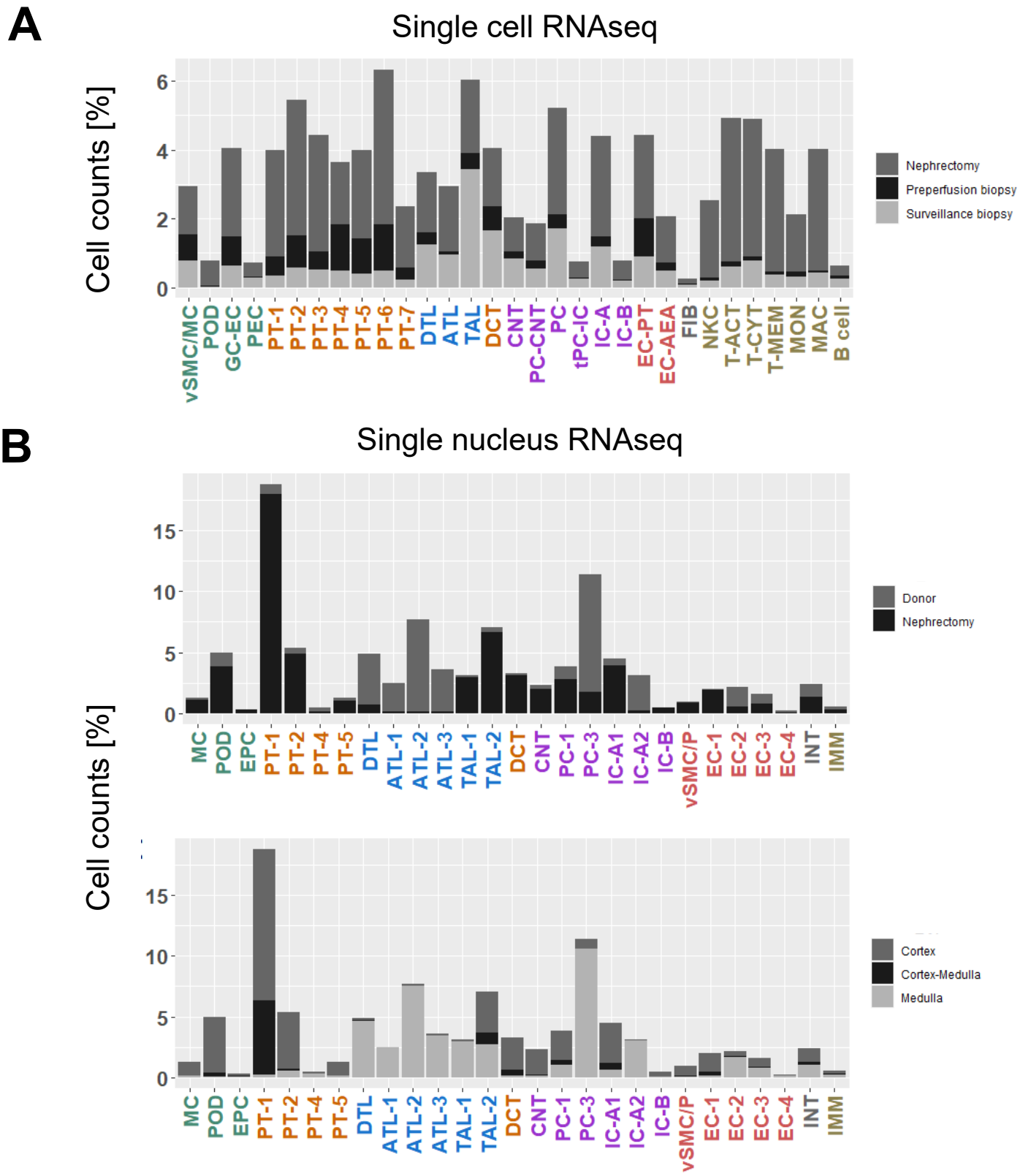

Supplemental Figure S4

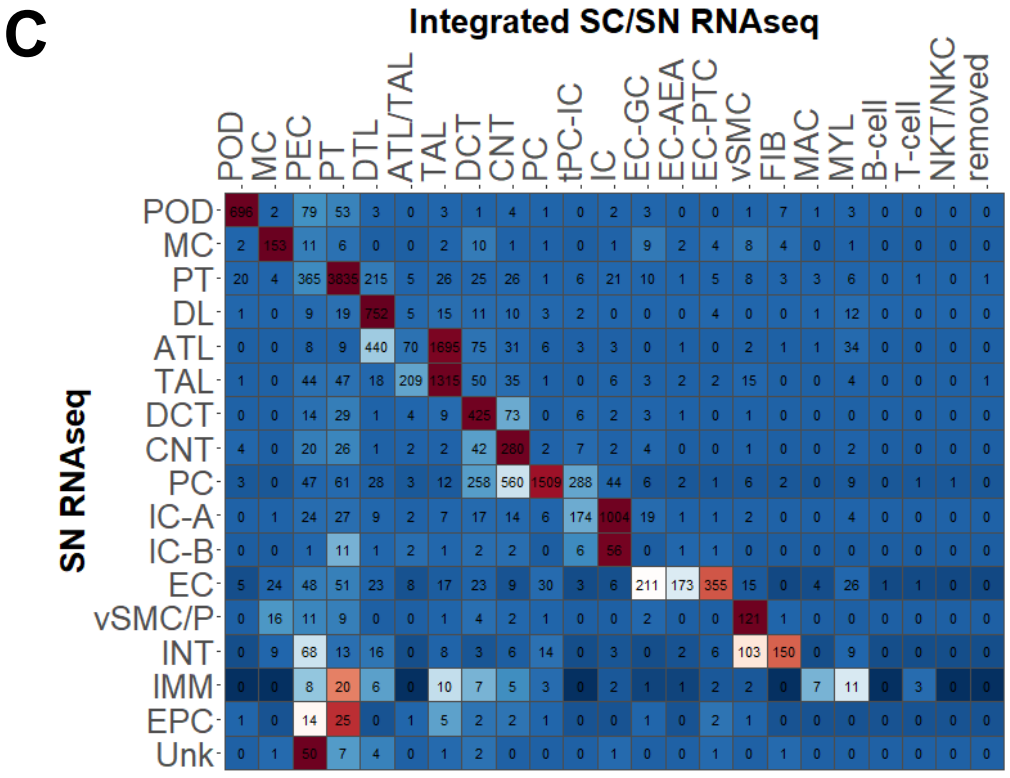

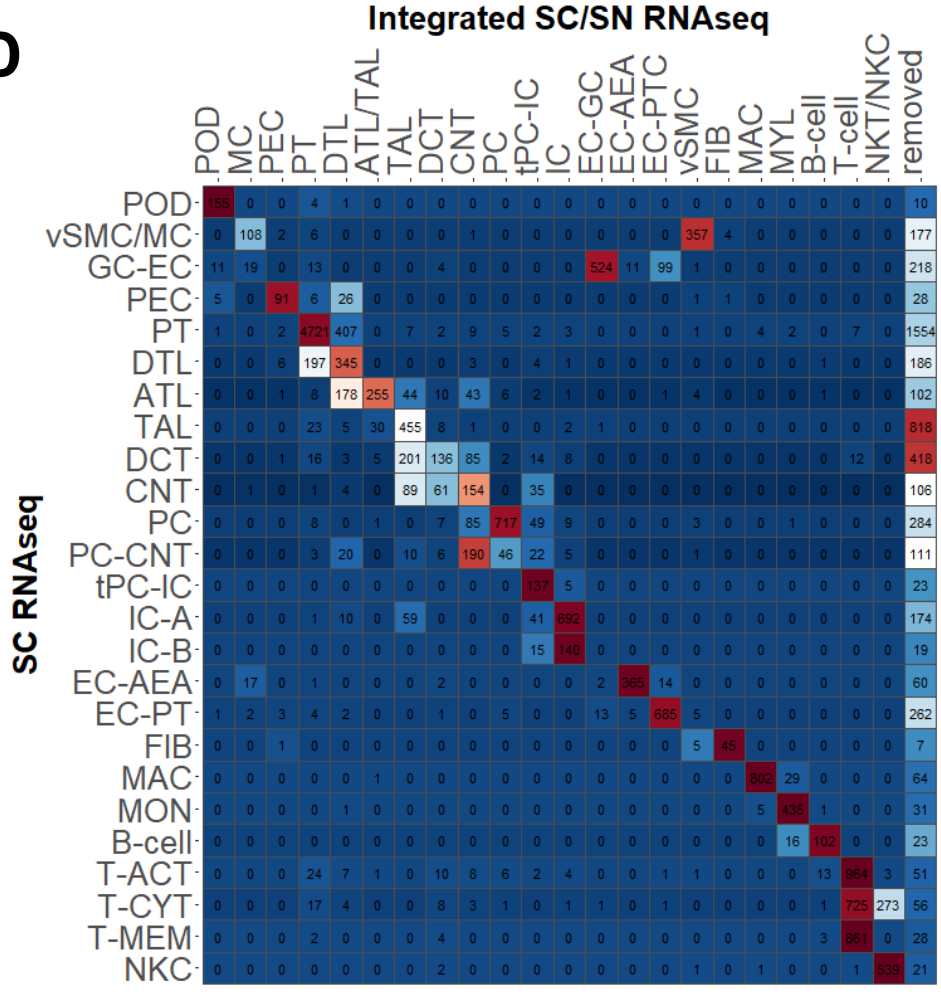

Supplemental Figure S4

E

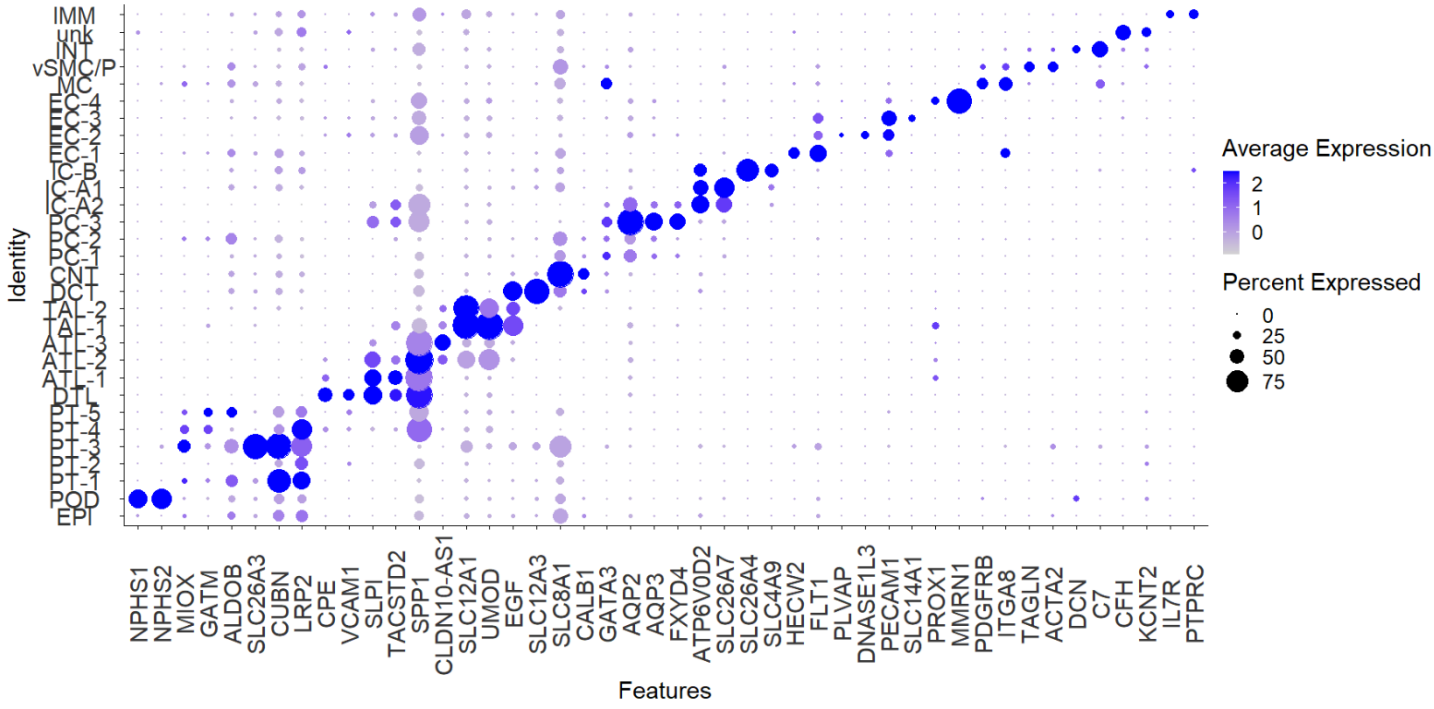

F

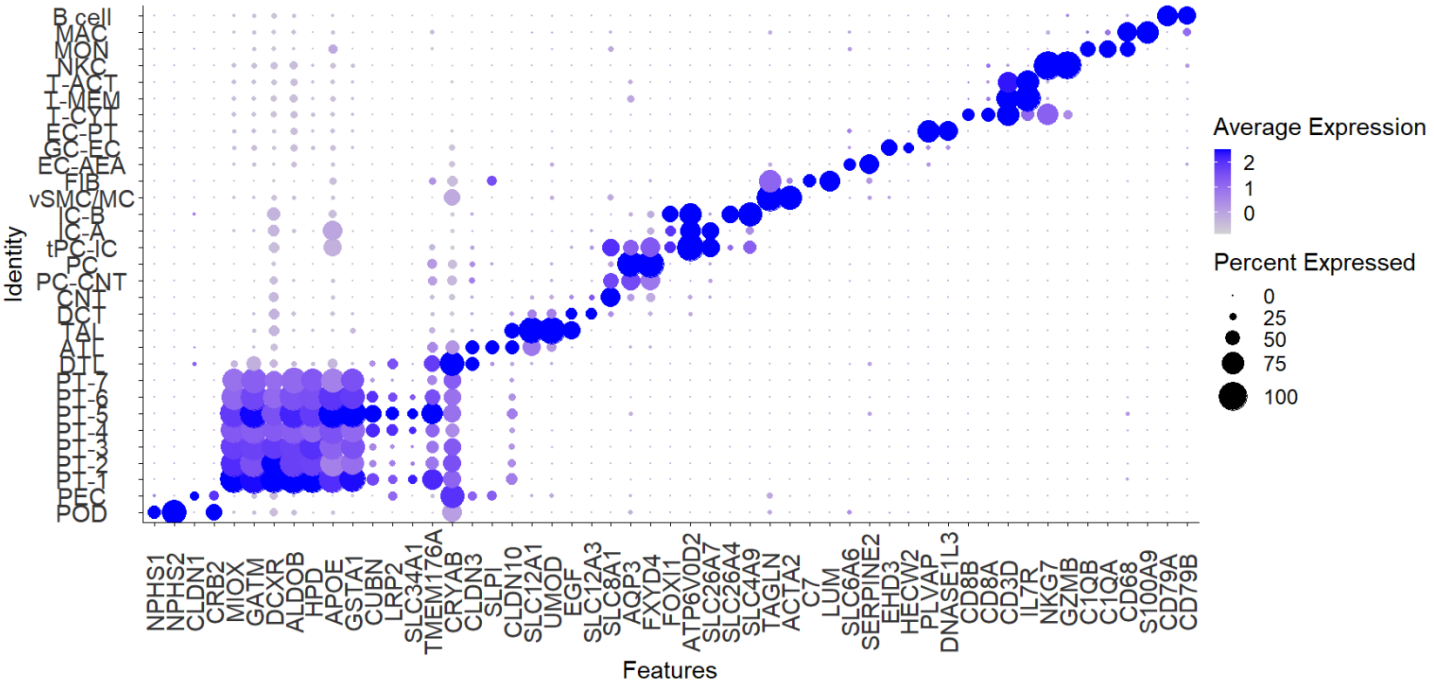

Supplemental Figure S4

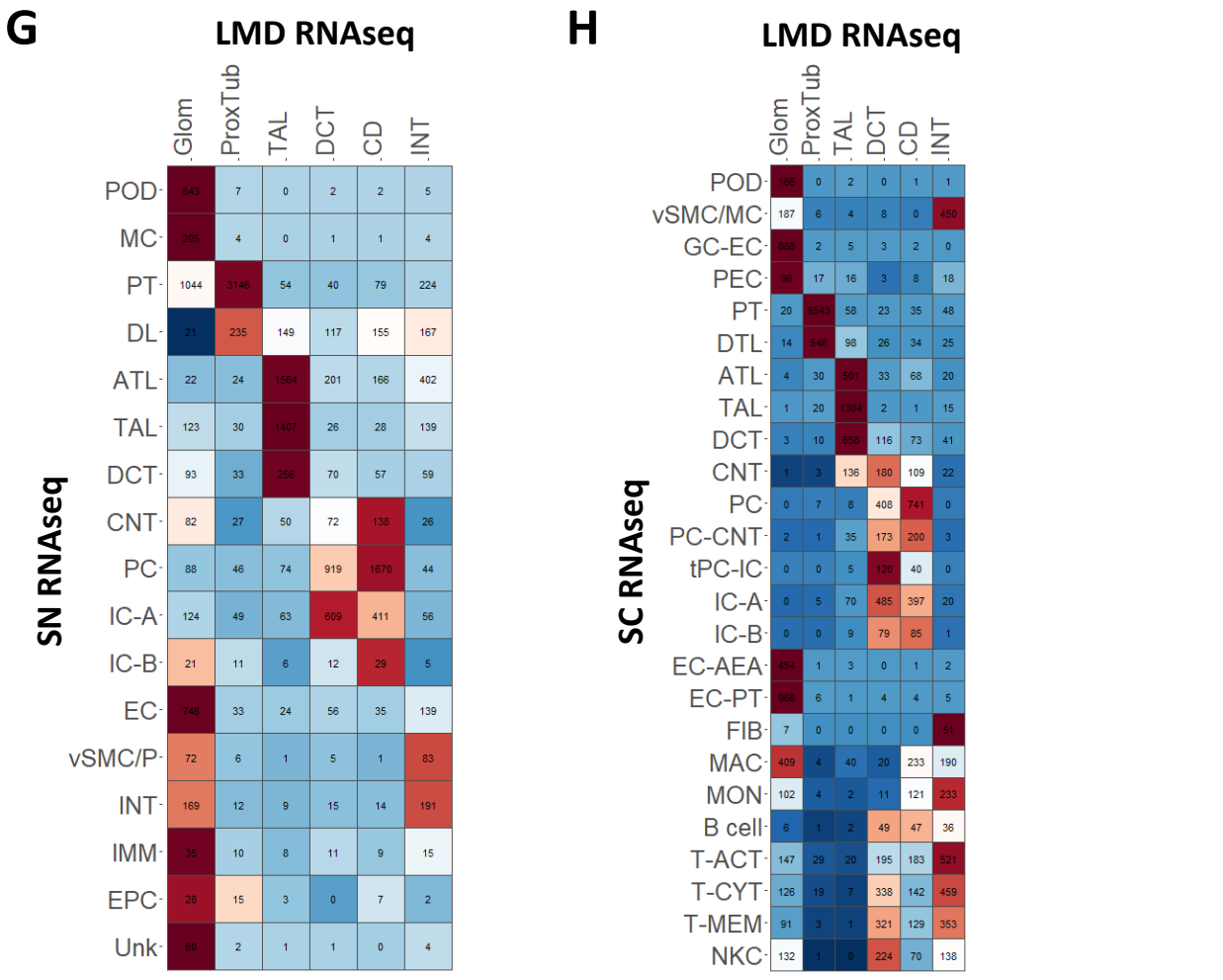

Supplemental Figure 4

Supplemental Figure S4: Separated and integrated analysis of sc and sn RNAseq datasets generate consistent cell type mapping. Cell types and subtypes identified by the separated analyses of the **(A)** sn and **(B)** sc RNAseq datasets. Bars indicate the percentage of all cells that mapped to a particular cell type or subtype, colors indicate the tissue collection method each particular cell was obtained by. Cell type assignments of separate clusters from **(C)** sn and **(D)** sc RNAseq datasets were compared to those obtained by the integrated analysis. Numbers indicate nuclei/cell counts; fields are colored by the percentage of cells within each field compared to the row margins. Note that in separated analyses of the sc RNAseq dataset, the applied cutoff for mitochondrial gene expression was higher (≤50% instead of ≤20%); consequently, some of the cells that were removed in the combined analysis were assigned to cell types in the separated analysis. Expression of cell type selective marker genes in cell subtypes identified **(E)** by single nucleus RNAseq and **(F)** single cell RNAseq. Mapping of the **(G)** nuclei and **(H)** cells to LMD segments documents that the annotations obtained from the separated analyses map to their correct anatomical origin, as observed for the integrated analysis. All heatmaps are colored according to the number of cells assigned to each LMD subsegment, scaled so each row has mean of 0 and standard deviation of 1. See figure 2A for cell type abbreviations.

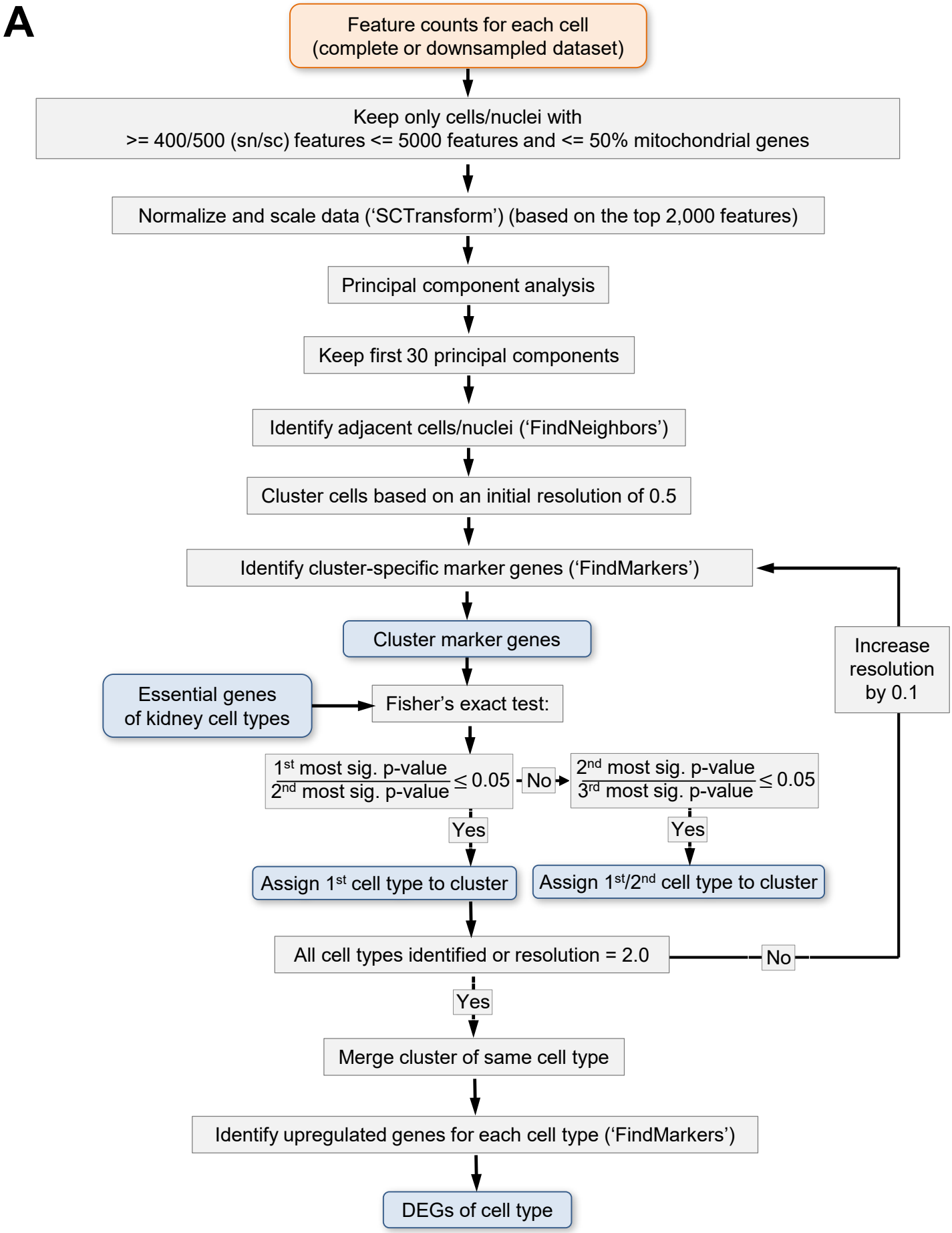

Supplemental Figure S5

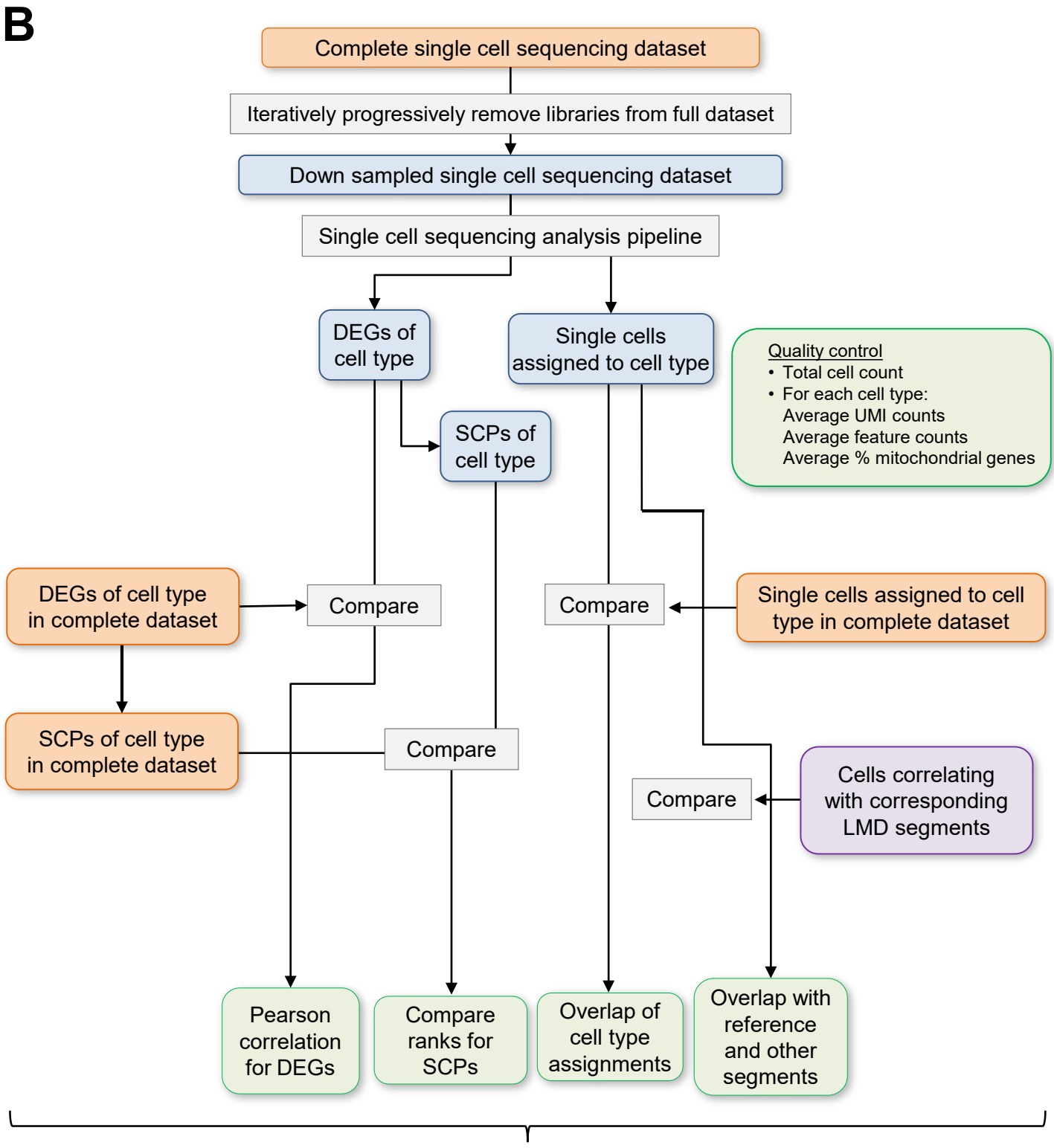

Supplemental Figure S5

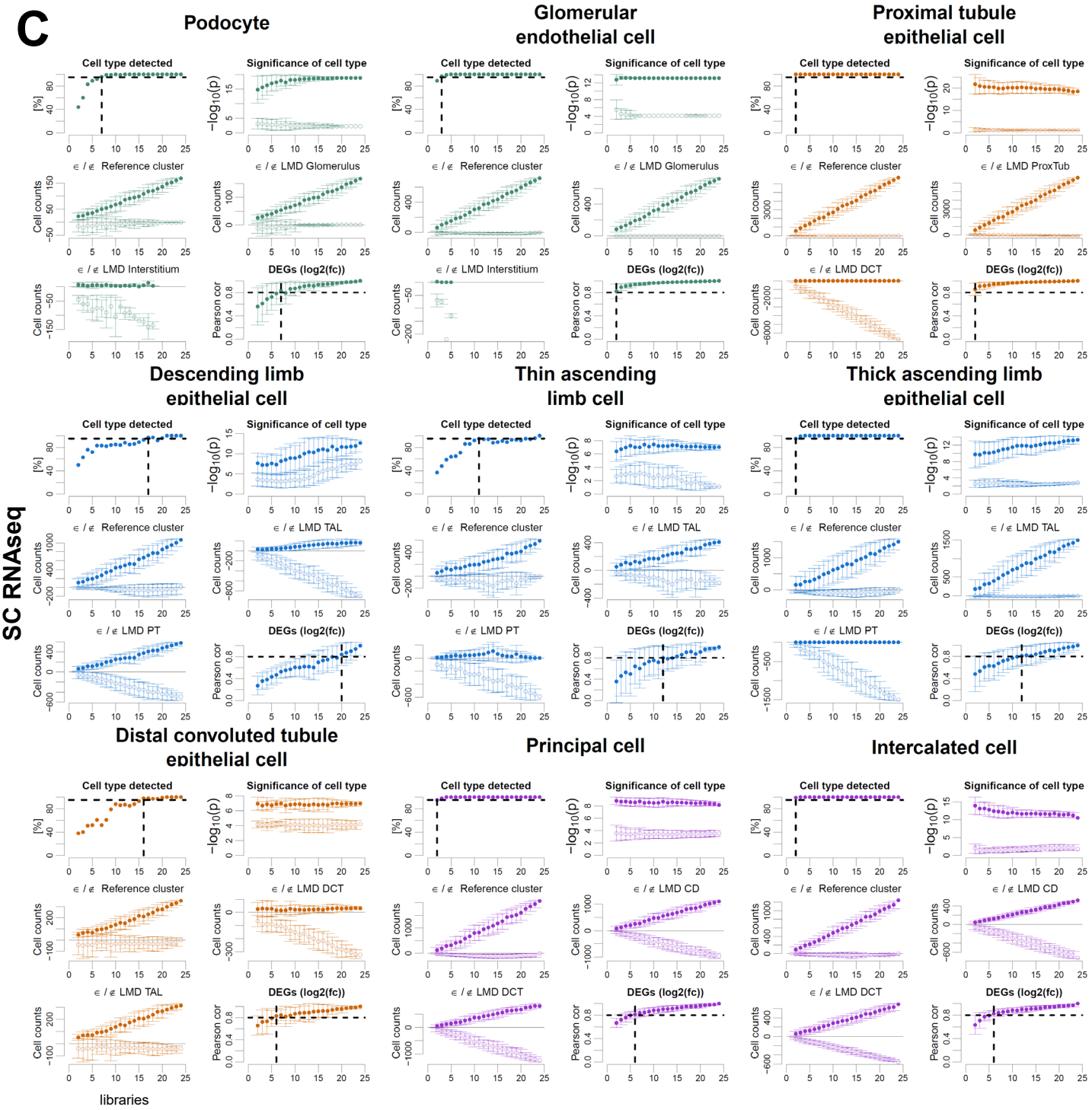

Supplemental Figure S5

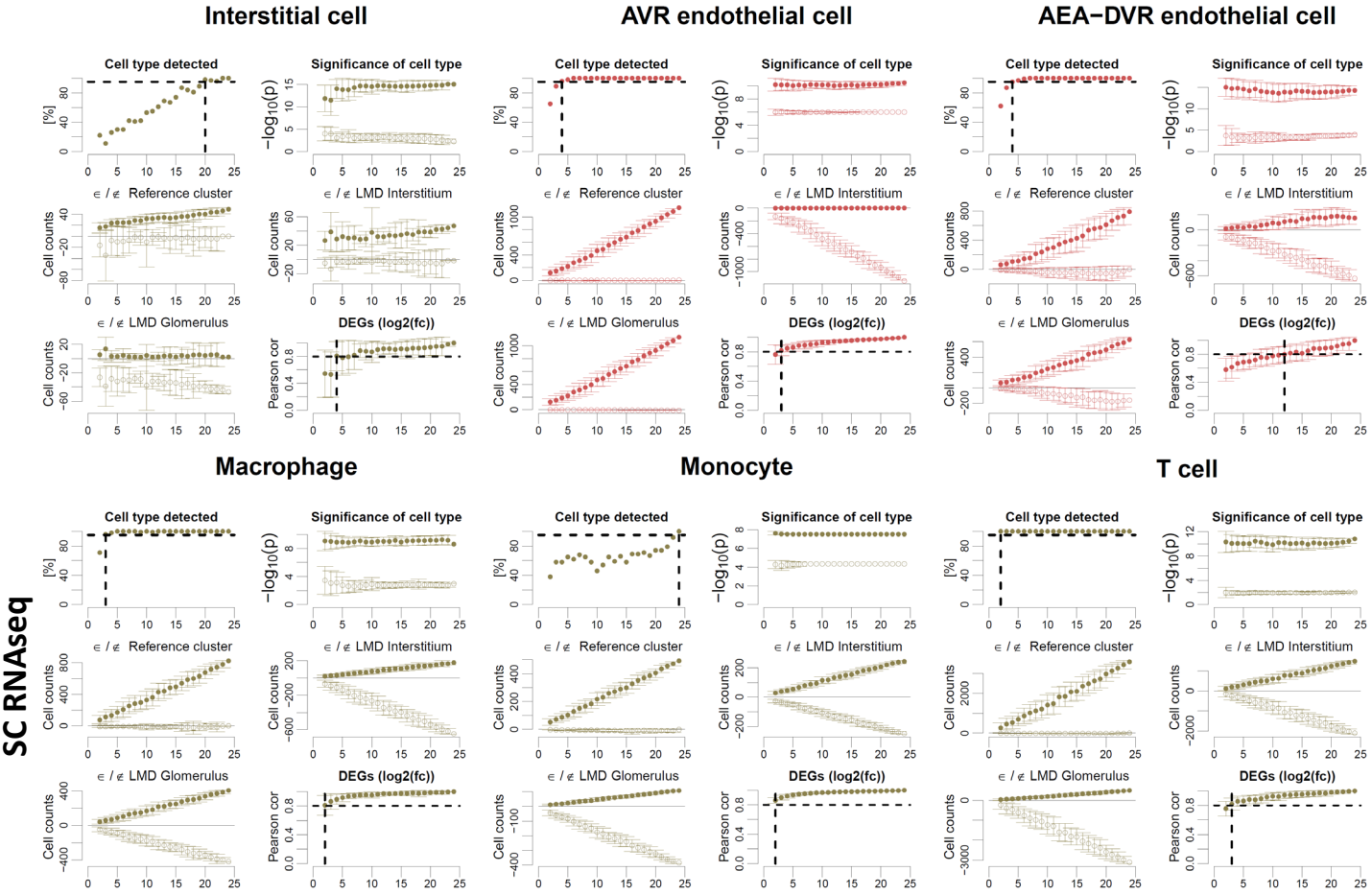

Quality control

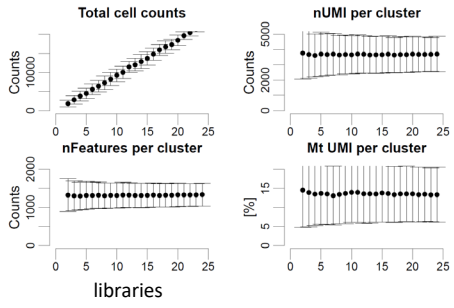

Libraries	Cells	Libraries	Cells
2	1835 +/− 917	14	12855 +/− 1831
3	2843 +/− 1081	15	13680 +/− 1746
4	3817 +/− 1251	16	14793 +/− 1568
5	4498 +/− 1345	17	15906 +/− 1461
6	5592 +/− 1390	18	16712 +/− 1628
7	6403 +/− 1519	19	17307 +/− 1383
8	7290 +/− 1813	20	18442 +/− 1335
9	8250 +/− 1705	21	19638 +/− 1002
10	9270 +/− 1617	22	20426 +/− 899
11	10044 +/− 1594	23	21336 +/− 680
12	11462 +/− 1457	24	22264 +/− 0
13	12016 +/− 1612		

Supplemental Figure S5

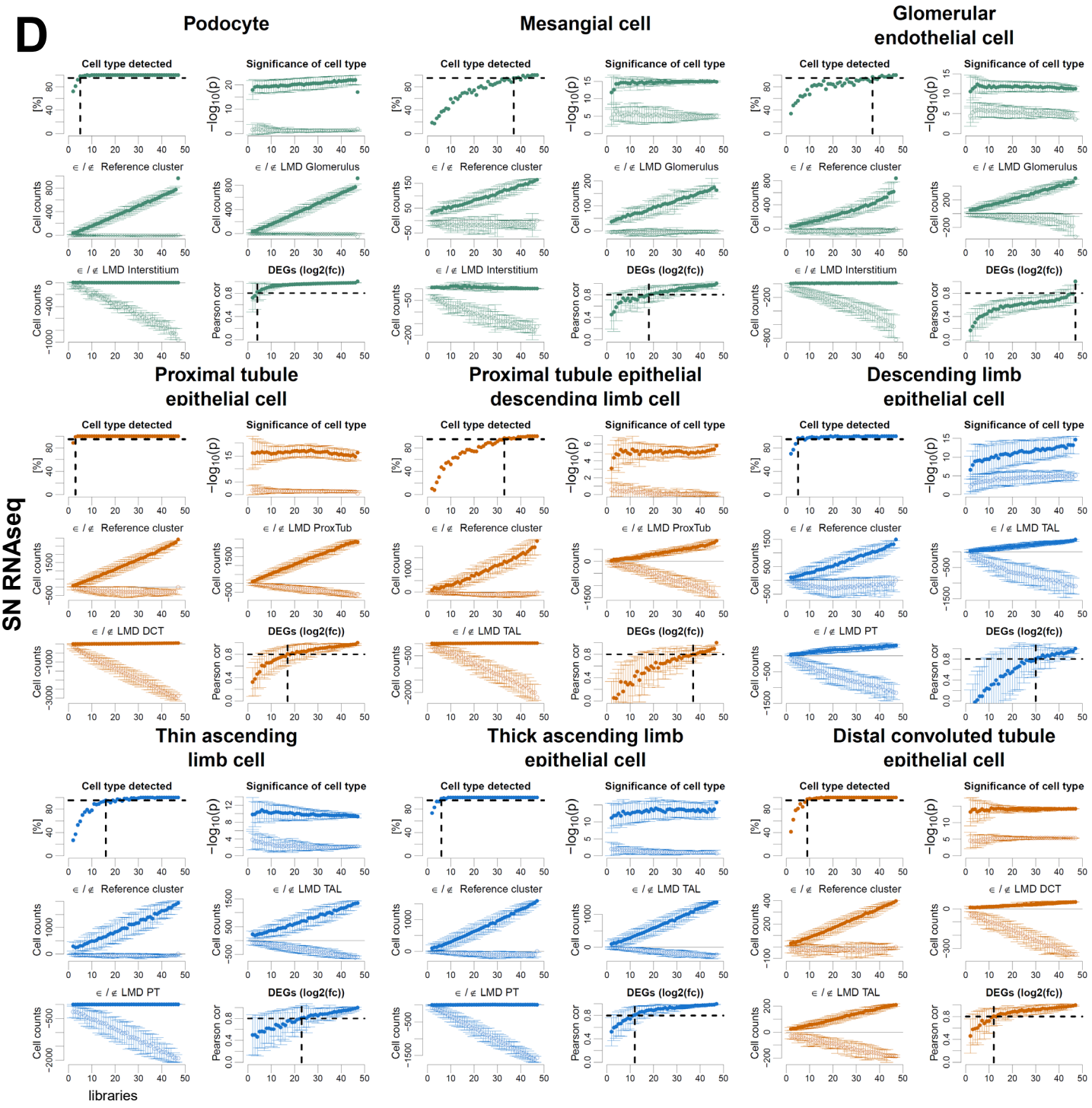

Supplemental Figure S5

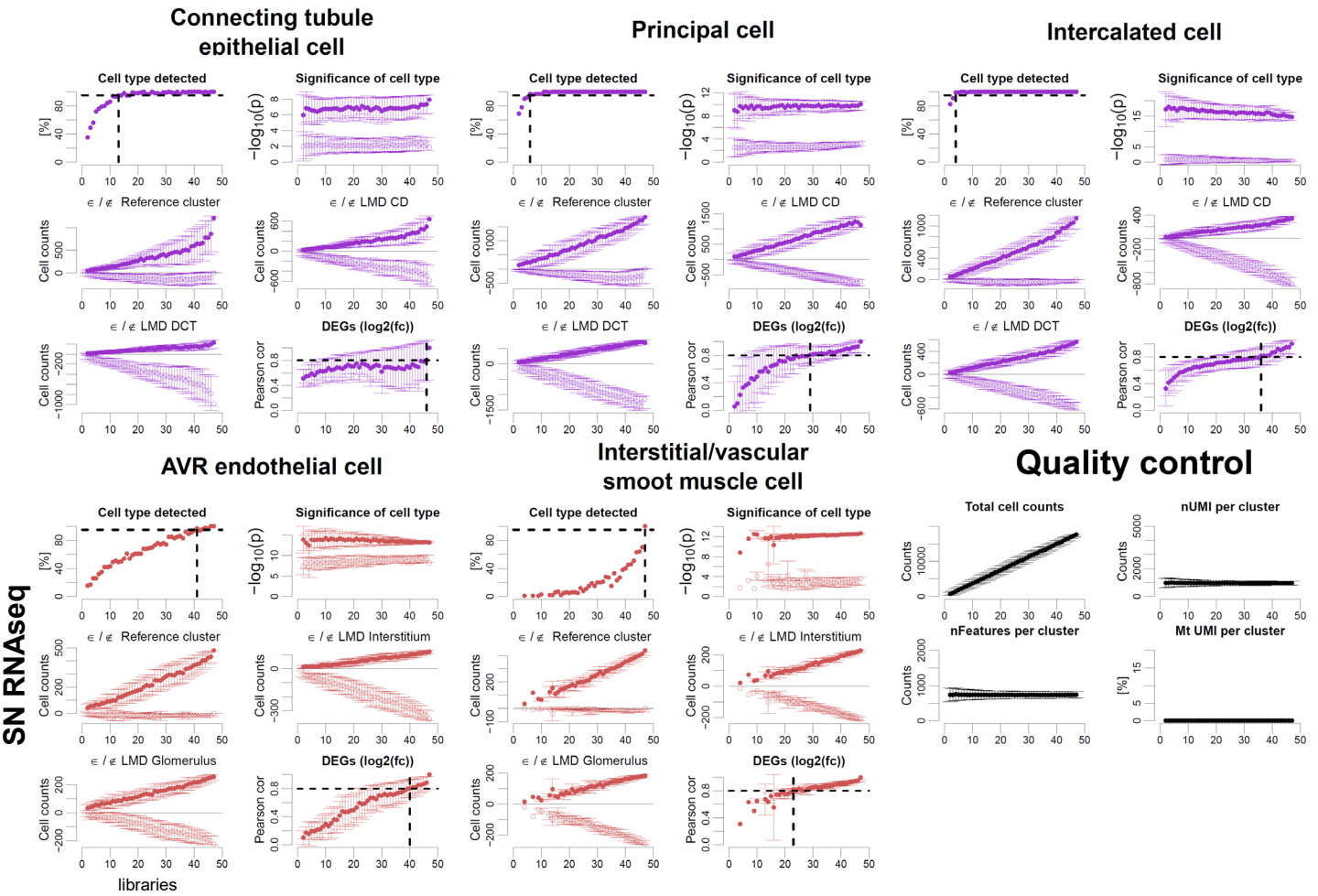

Libraries	Nuclei	Libraries	Nuclei	Libraries	Nuclei
2	755 +/− 473	18	6812 +/− 1110	32	12089 +/− 1001
3	1043 +/− 463	19	7089 +/− 1003	33	12322 +/− 999
4	1464 +/− 639	20	7482 +/− 1151	34	12879 +/− 1103
5	1921 +/− 651	21	7878 +/− 1075	35	13085 +/− 1027
6	2235 +/− 706	22	8192 +/− 1103	36	13300 +/− 893
7	2665 +/− 788	23	8637 +/− 1150	37	13844 +/− 959
8	2989 +/− 796	24	9085 +/− 1031	38	14165 +/− 899
9	3395 +/− 947	25	9359 +/− 1096	39	14577 +/− 811
10	3718 +/− 911	26	9836 +/− 1227	40	15054 +/− 844
11	4128 +/− 892	27	10268 +/− 1131	41	15272 +/− 778
12	4438 +/− 936	28	10421 +/− 1079	42	15661 +/− 721
13	4930 +/− 1161	29	10831 +/− 1187	43	16197 +/− 683
14	5221 +/− 1152	30	11329 +/− 1063	44	16451 +/− 560
15	5634 +/− 1033	31	11798 +/− 1145	45	16934 +/− 448
16	5881 +/− 1078			46	17279 +/− 323
17	6403 +/− 1076			47	17655 +/− 0

Supplemental Figure S5

Supplemental Figure S5. Complete results of single-cell/nucleus transcriptomic *post hoc* power analysis. Subject libraries or samples were randomly and progressively removed from the sc (24 libraries) and sn (47 libraries) RNAseq to generate at max 100 non-overlapping random groups for each number of remaining libraries. **(A)** Sc and sn datasets were subjected to an automated sc/sn data analysis pipeline. **(B)** Results were averaged for each number of subject libraries and compared between the downsampled and complete datasets as indicated. *Post hoc* power results of the **(C)** sc and **(D)** sn RNAseq datasets. **'Cell type detected':** This plot documents how often (in percent) a particular cell type was detected in dependence of the number of analyzed libraries. **'Significance of cell type'**: To assign cell types to each cluster we subjected cluster specific marker genes to enrichment analysis using Fisher's Exact test and a list of literature curated cell-type specific essential genes. For each cluster predicted cell types were ranked by significance and the top ranked cell type was assigned to that cluster. The plot shows the $-\log_{10}$(p-values) of the first (i.e. the selected) and the second ranked cell type. Comparison of both p-values allows an estimation of the reliability of a particular cell type assignment. The larger the difference between both $-\log_{10}$(p-values), the more certain is that particular cell type assignment. **'element/not element of Reference cluster':** Cells/nuclei that were assigned to the same (above abscise, positive values, full circles) or to a different cell type (below abscise, negative values, open circles) as in the full dataset were counted in each downsampled dataset. **'element/not element of indicated LMD subsegment':** Using cell and nuclei mappings presented in Suppl. Figure 4E/F we counted how many cells/nuclei of a particular cell type mapped to the indicated LMD subsegment (above abscise, positive values, full circles) or to a different LMD subsegment (below abscise, negative values, open circles). **'DEGs log(fc)'**: Correlation between the log fold changes of cell type specific markers obtained for the downsampled and complete dataset. Notify that all comparisons were only done, if a particular cell type was detected (as indicated in the first diagram). See figure 2A for cell type abbreviations.

A

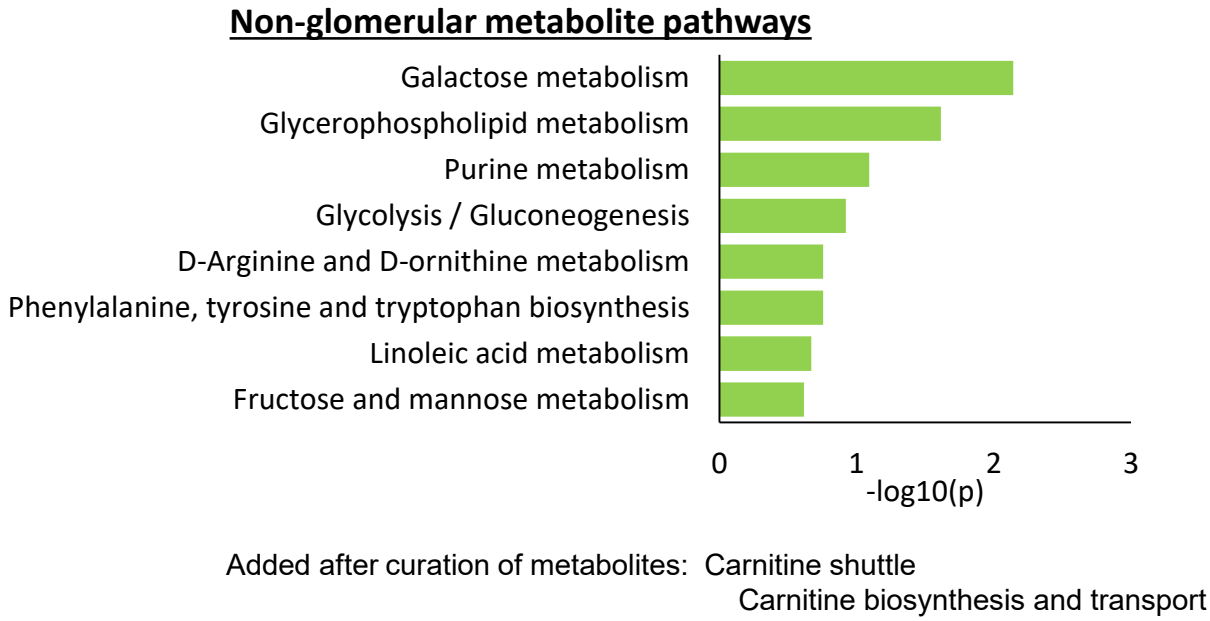

B

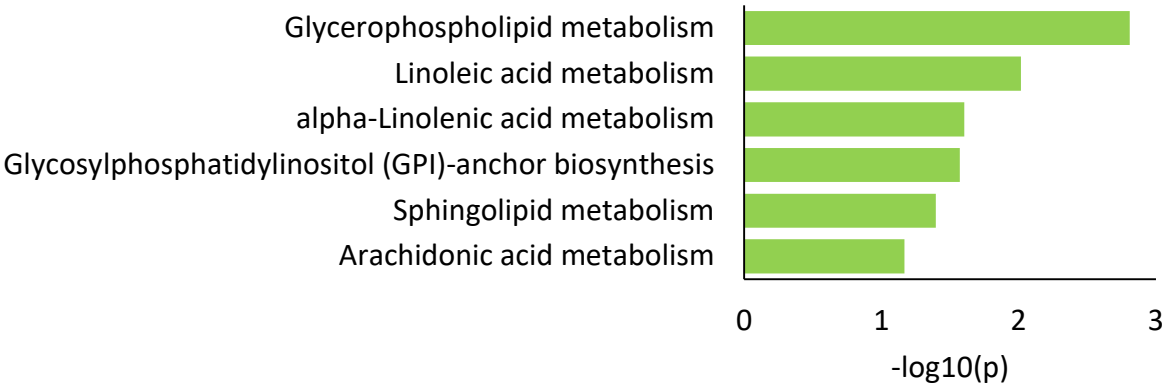

Supplemental Figure S6

Supplemental Figure S6: Pathway enrichment analysis of spatial metabolomics data. All **(A)** Non-glomerular and **(B)** glomerular metabolites obtained from the three nephrectomy samples were subjected to pathway enrichment analysis using MetaboAnalyst. Some pathways were predicted from metabolites that are general precursors for the synthesis of multiple products and participate in multiple pathways. To exclude such unspecific and consequently uncertain pathway predictions, we focused only on those pathways that were predicted from a pathway specific metabolite (see methods for details). To merge the metabolic pathways with the MBCO SCP-networks, we mapped the MetaboAnalyst pathways 'Glycolysis/Gluconeogenesis' and 'Glycerophospholipid metabolism' to the MBCP SCPs 'Glycolysis and Gluconeogenesis' and to 'Phosphoglyceride biosynthesis', respectively. Based on identified metabolites, we added the MBCO SCPs "Carnitine shuttle" and "Carnitine biosynthesis and transport" to the predicted MetaboAnalyst pathways (see methods for details).

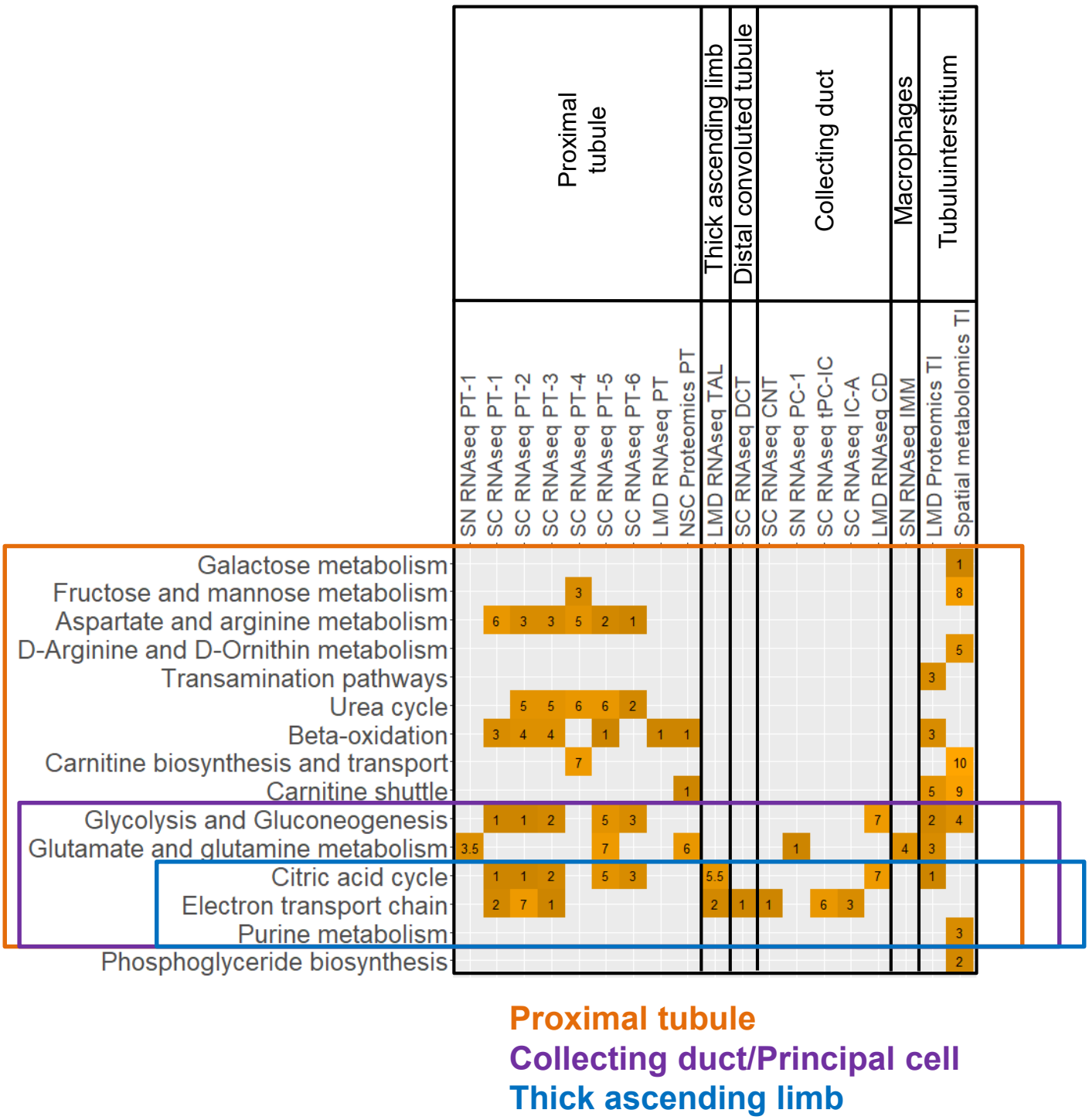

Supplemental figure S7

Supplemental Figure S7: Mapping of tubulointerstitial SCPs to cell types. SCPs predicted by dynamic enrichment analysis for the tubulointerstitial segment by the LMD Proteomics and spatial metabolomics assays were mapped to one of three detected glomerular cell types, because they were either detected in that cell type as well or related to SCPs detected for that cell type. Numbers indicate at which rank a particular SCP was detected. Notify that dynamic enrichment analysis can predict single SCPs or combinations of up to three SCPs, and consequently the same rank can be given to multiple SCPs. When an SCP was predicted by multiple cell subtypes, the highest rank is visualized in this figure.

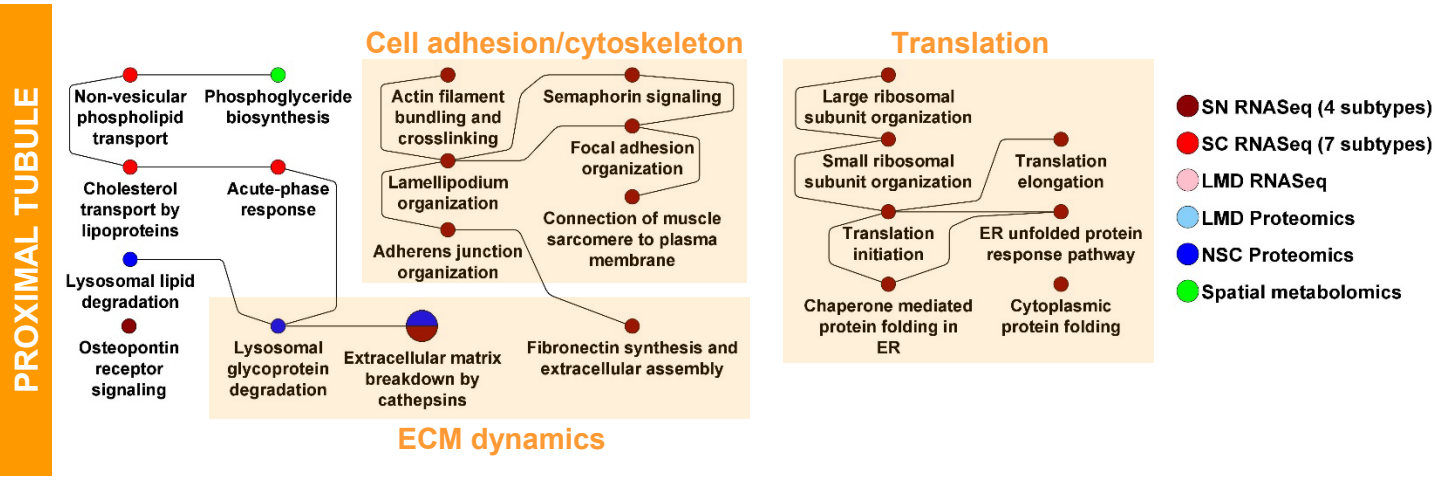

Supplemental Figure S8

Supplemental Figure S8: Enrichment analysis of differentially expressed genes and proteins in proximal tubule cells and subsegments. See Figure 5 for details. SCPs that were among the top seven predictions based on dynamic enrichment analysis of PT DEGs and DEPs and were removed from the main figure for space reasons.

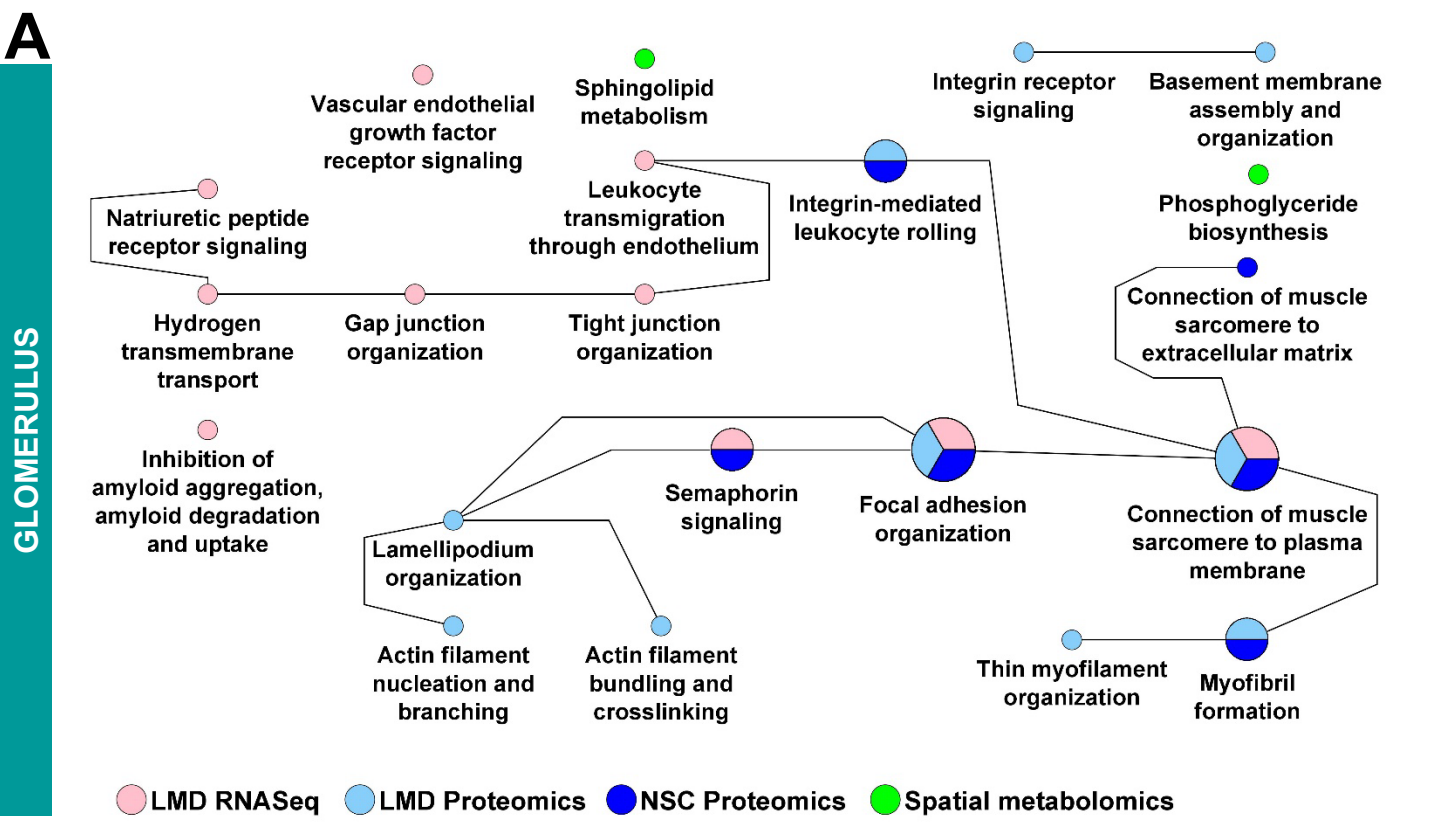

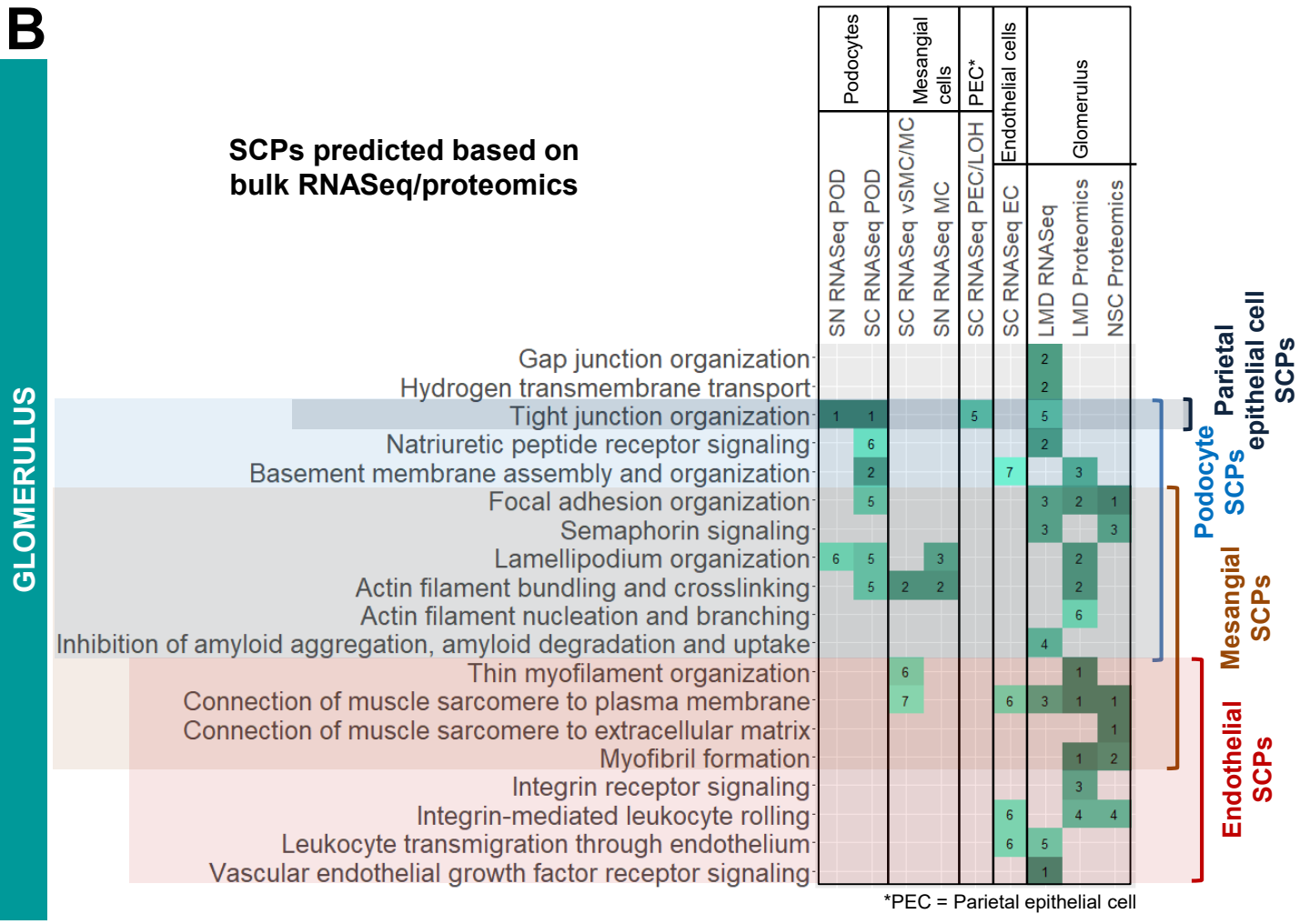

Supplemental Figure S9

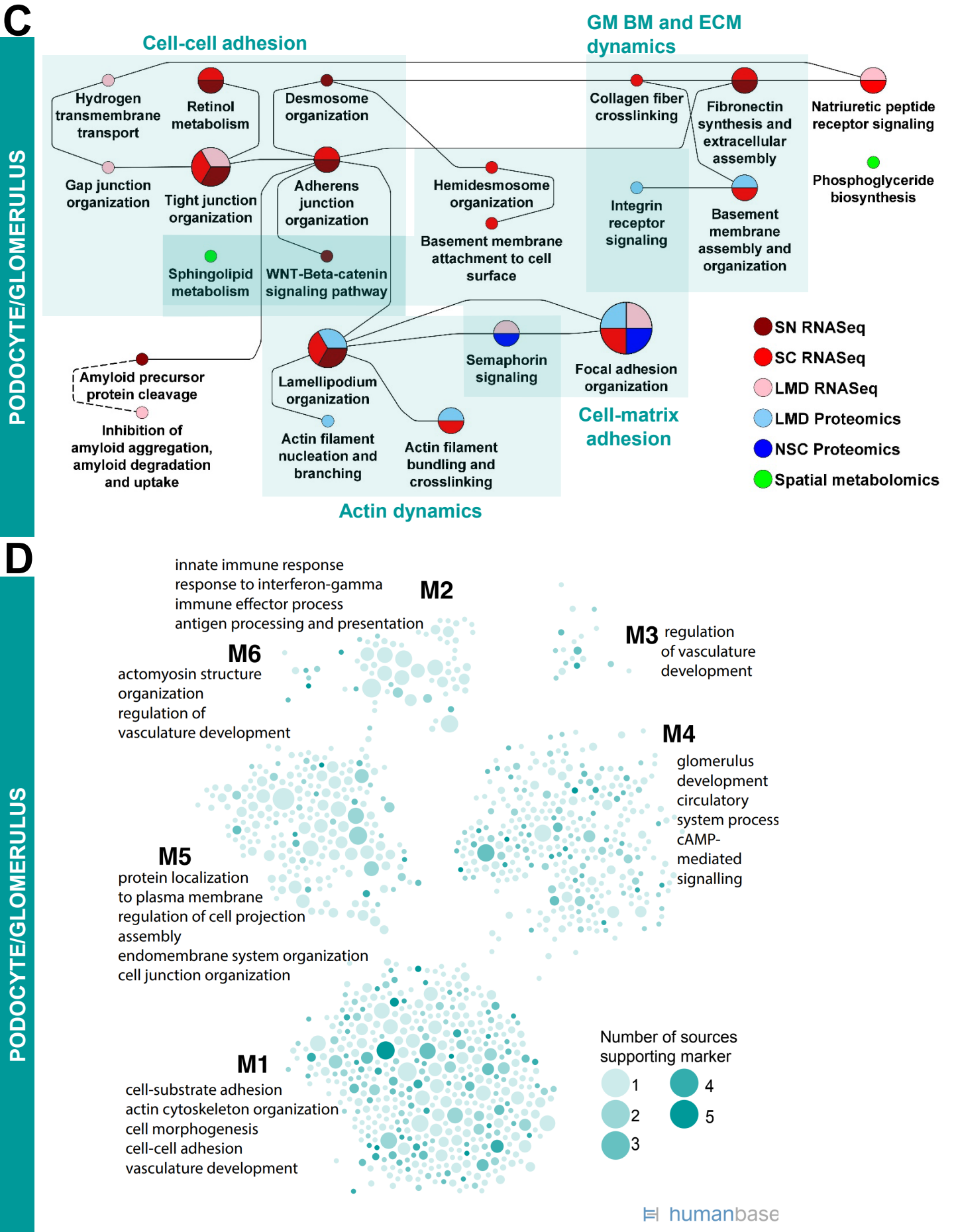

Supplemental Figure S9

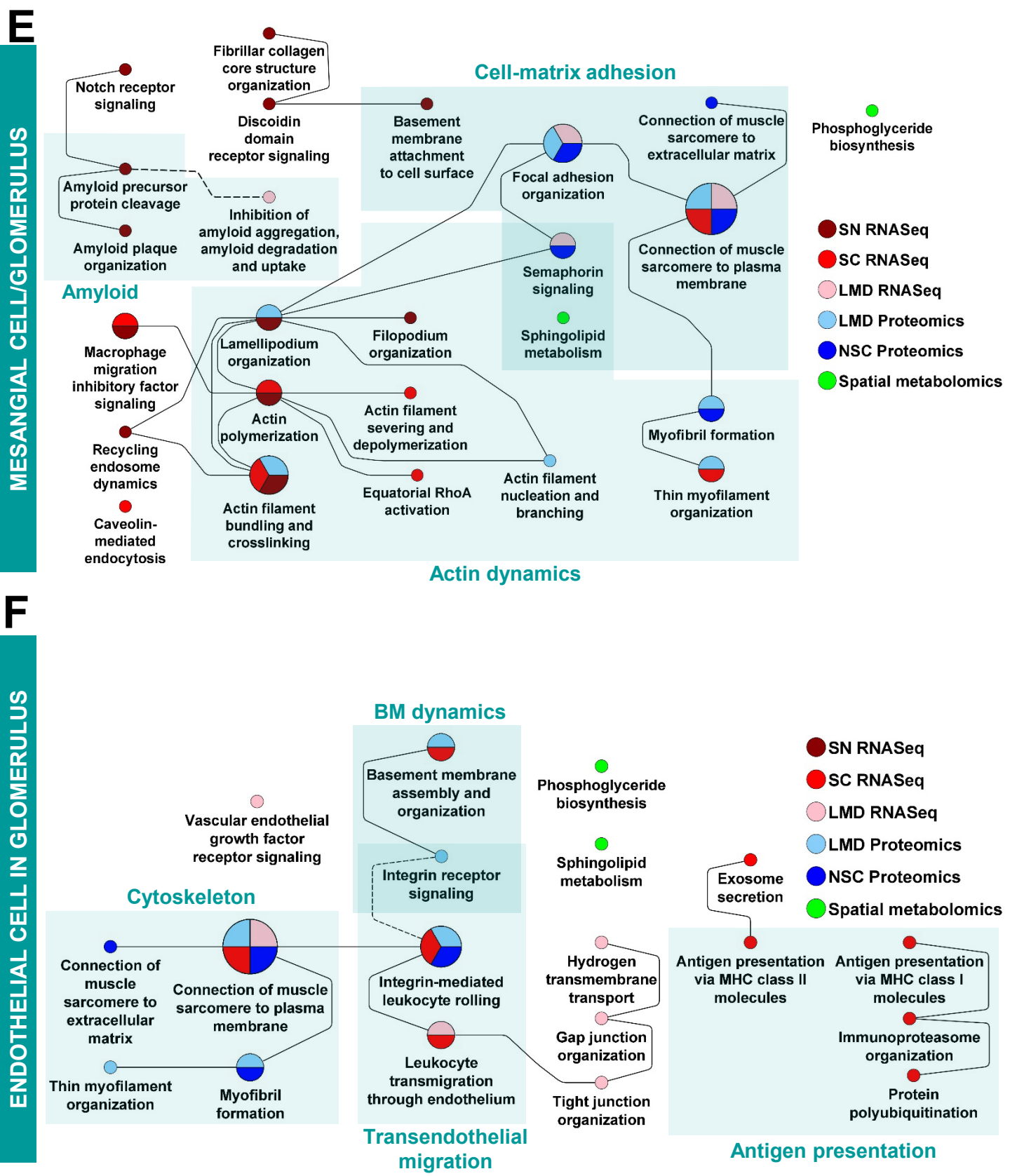

Supplemental Figure S9

G

PARIETAL EPITHELIAL CELL/ GLOMERULUS

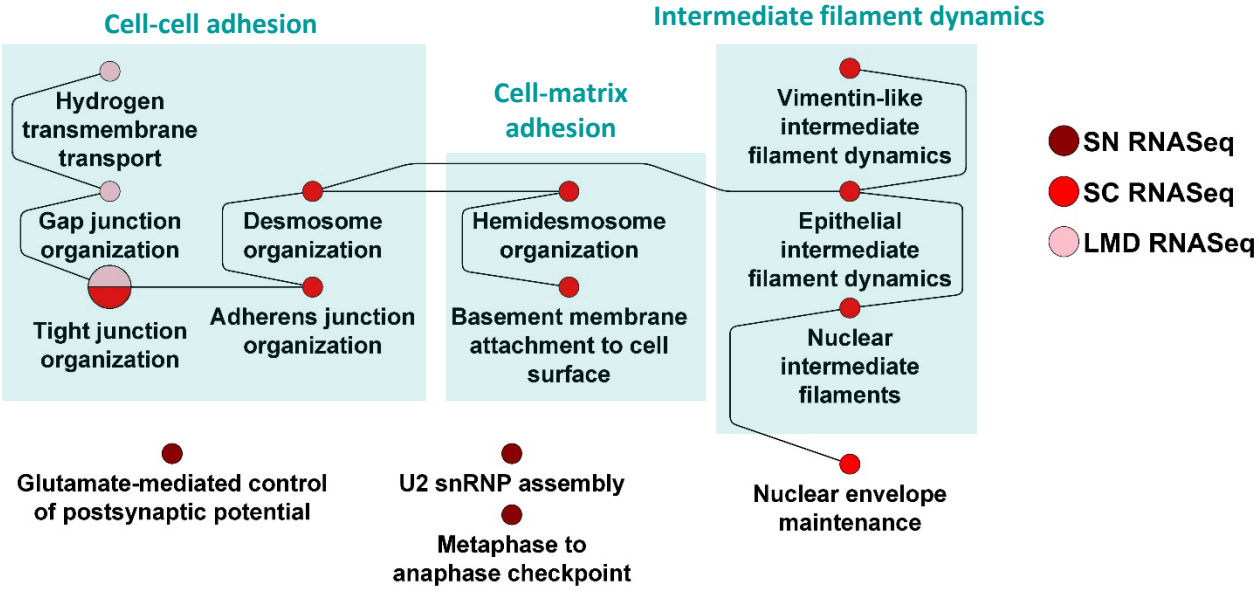

Supplemental Figure S9

Supplemental Figure S9: Enrichment analysis for glomerular datasets. (A) Marker genes and proteins identified by LMD RNAseq and Proteomics and NSC Proteomics were subjected to dynamic enrichment analysis. **(B)** Predicted glomerular SCPs were mapped to one of four detected glomerular cell types, because they were either detected in that cell type as well or related to SCPs detected for that cell type. Numbers indicate at which rank a particular SCP was detected. Notify that dynamic enrichment analysis can predict single SCPs or combinations of up to three SCPs, and consequently the same rank can be given to multiple SCPs. **(C)** SCP networks predicted for podocytes based on the sn and sc RNAseq datasets were merged with the podocyte mapped SCPs identified in B. **(D)** Podocyte specific modules were generated by combined analysis of the podocyte sc and sn marker genes and all glomerular marker genes and proteins. SCP networks predicted for **(E)** mesangial cells, **(F)** glomerular endothelial cells and **(G)** parietal epithelial cells based on sn and sc RNAseq datasets were merged with the SCPs that were mapped to these cell types in (B).

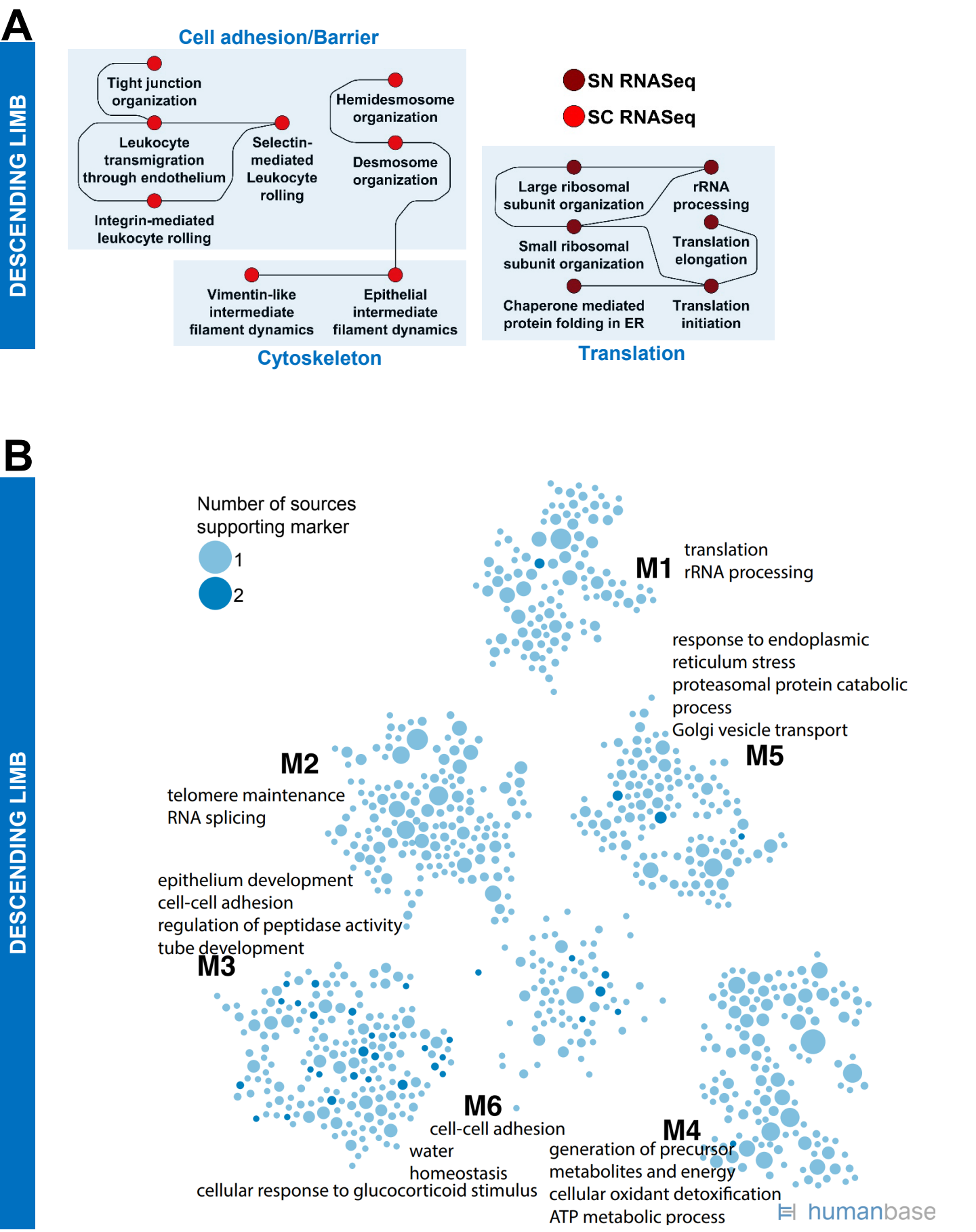

Supplemental Figure S10

C

THIN ASCENDING LIMB

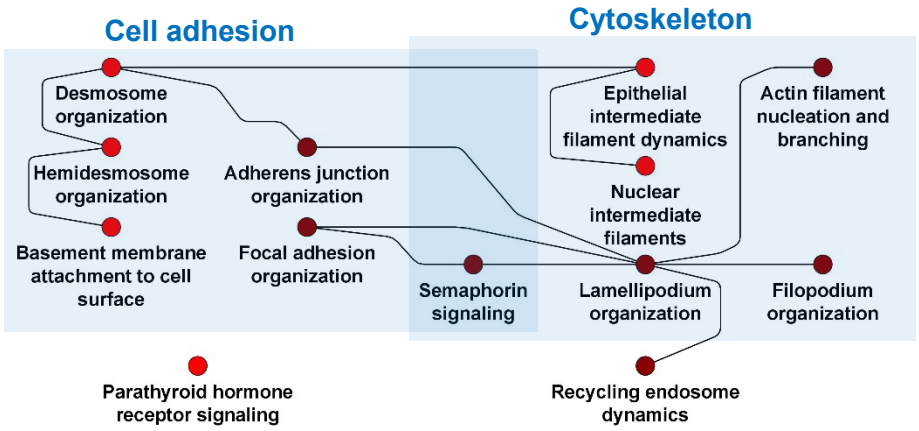

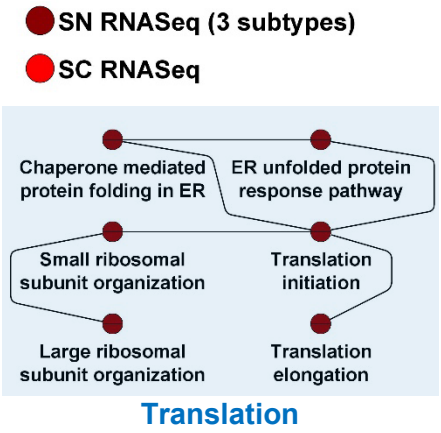

D

THIN ASCENDING LIMB

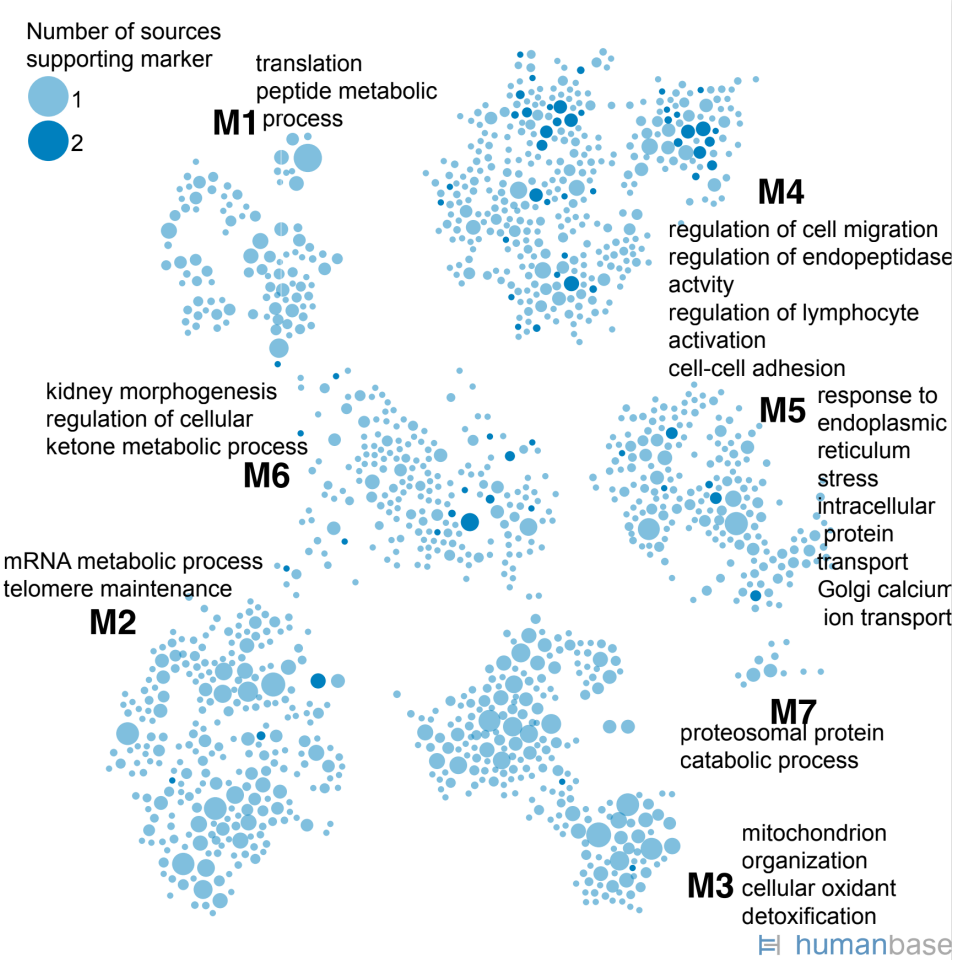

Supplemental Figure S10

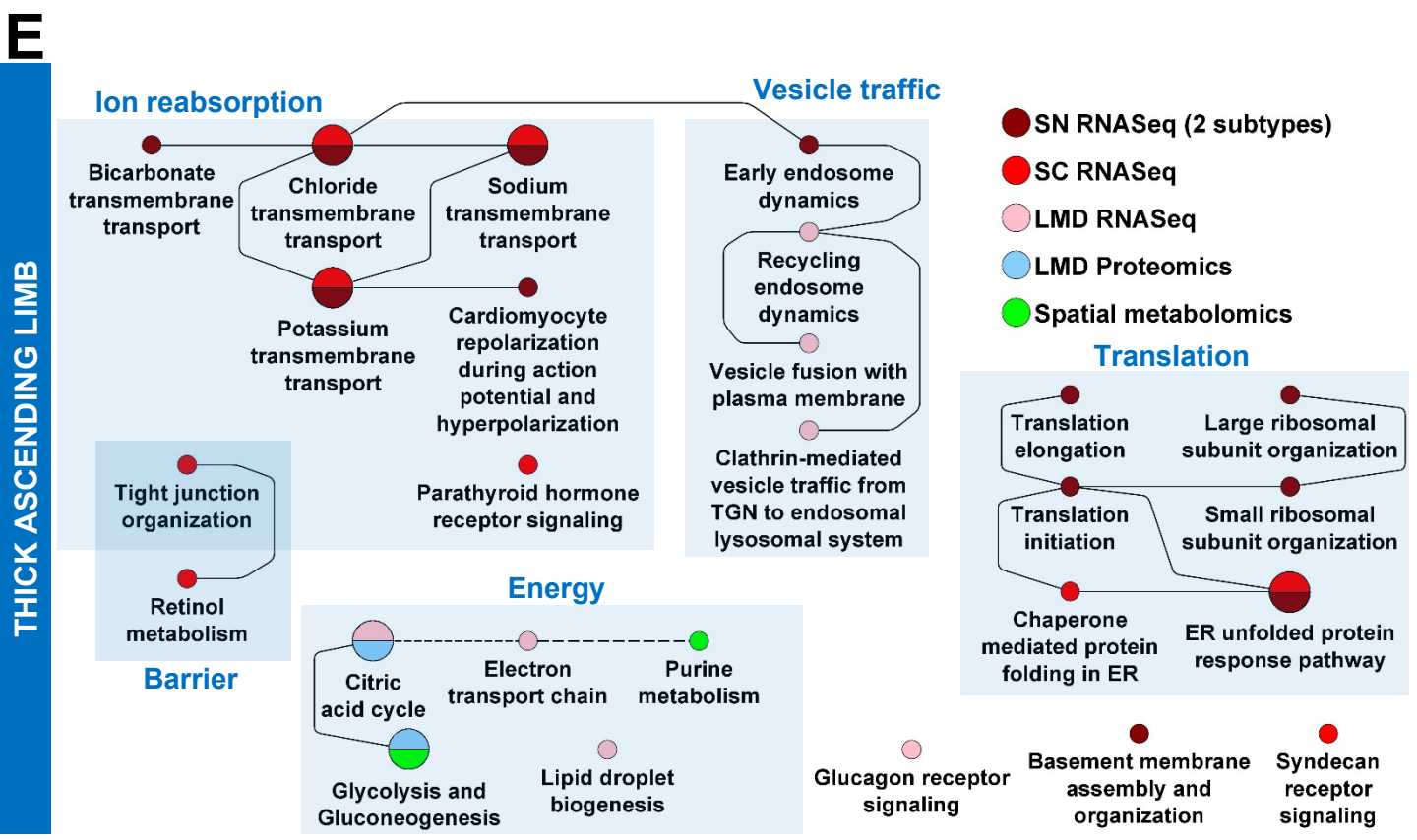

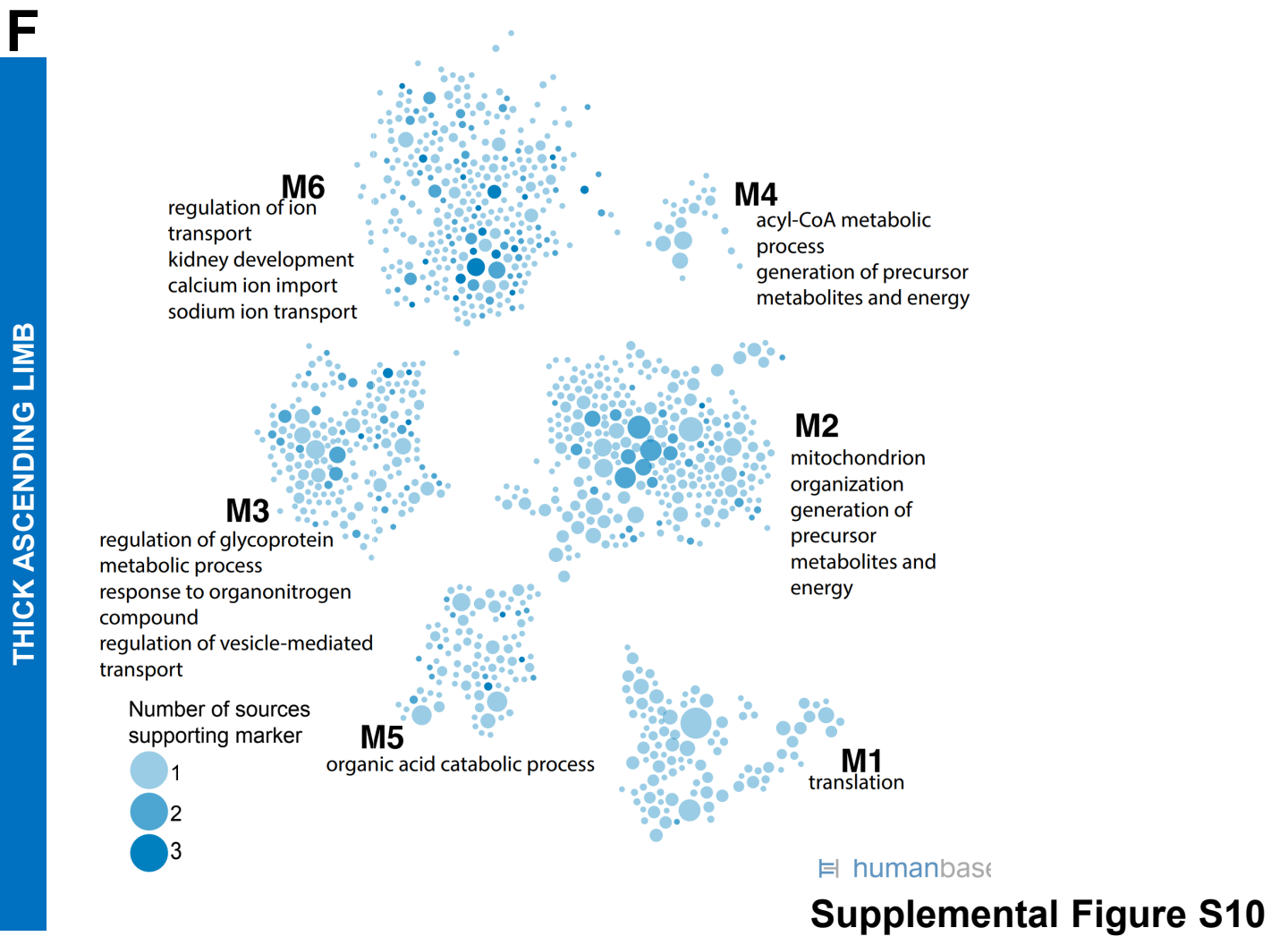

Supplemental Figure S10

Supplemental Figure S10: Enrichment analysis for the Loop of Henle. Descending limb cell specific marker genes were subjected to **(A)** dynamic enrichment and **(B)** humanbase module analysis. **(C)** Dynamic enrichment and **(D)** module analysis results of thin ascending limb cell marker genes. **(E)** Dynamic enrichment and **(F)** module analysis results of thick ascending limb cell marker genes.

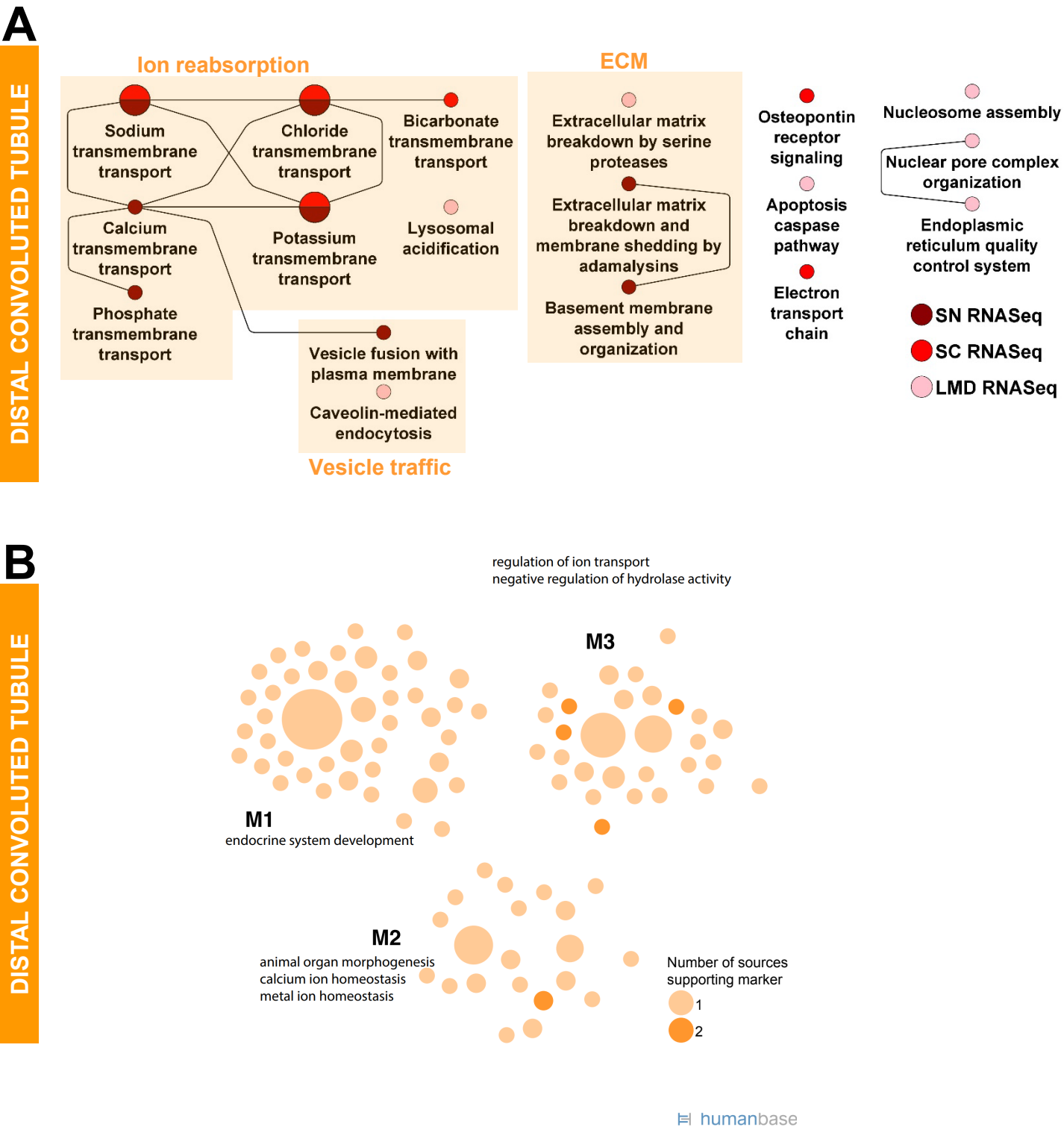

Supplemental Figure S11

Supplemental Figure S11: Enrichment analysis for the distal convoluted tubule. Distal convoluted tubule cell and segment specific DEGs were subjected to **(A)** dynamic enrichment and **(B)** module analysis.

A

CONNECTING TUBULE

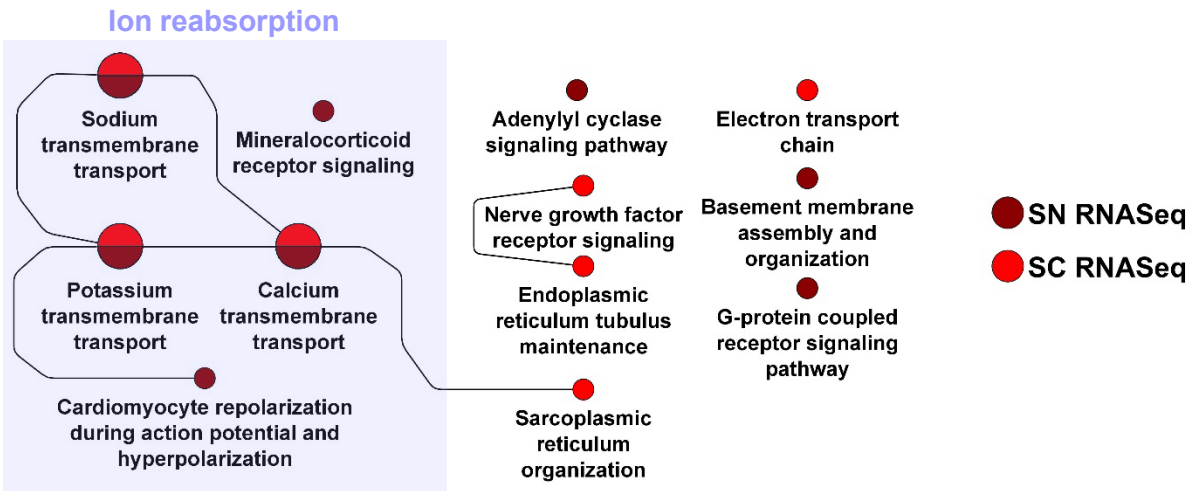

B

CONNECTING TUBULE

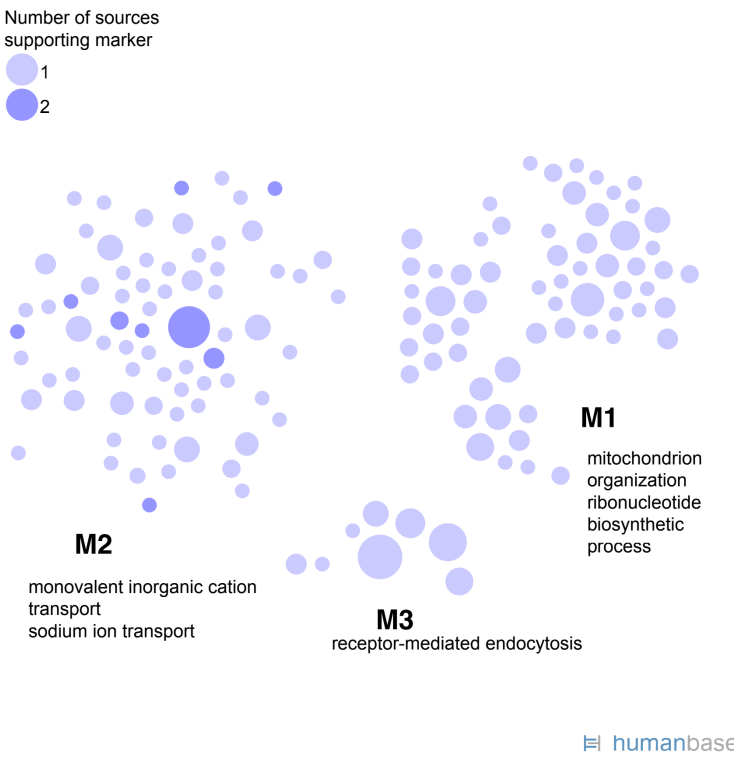

Supplemental Figure S12

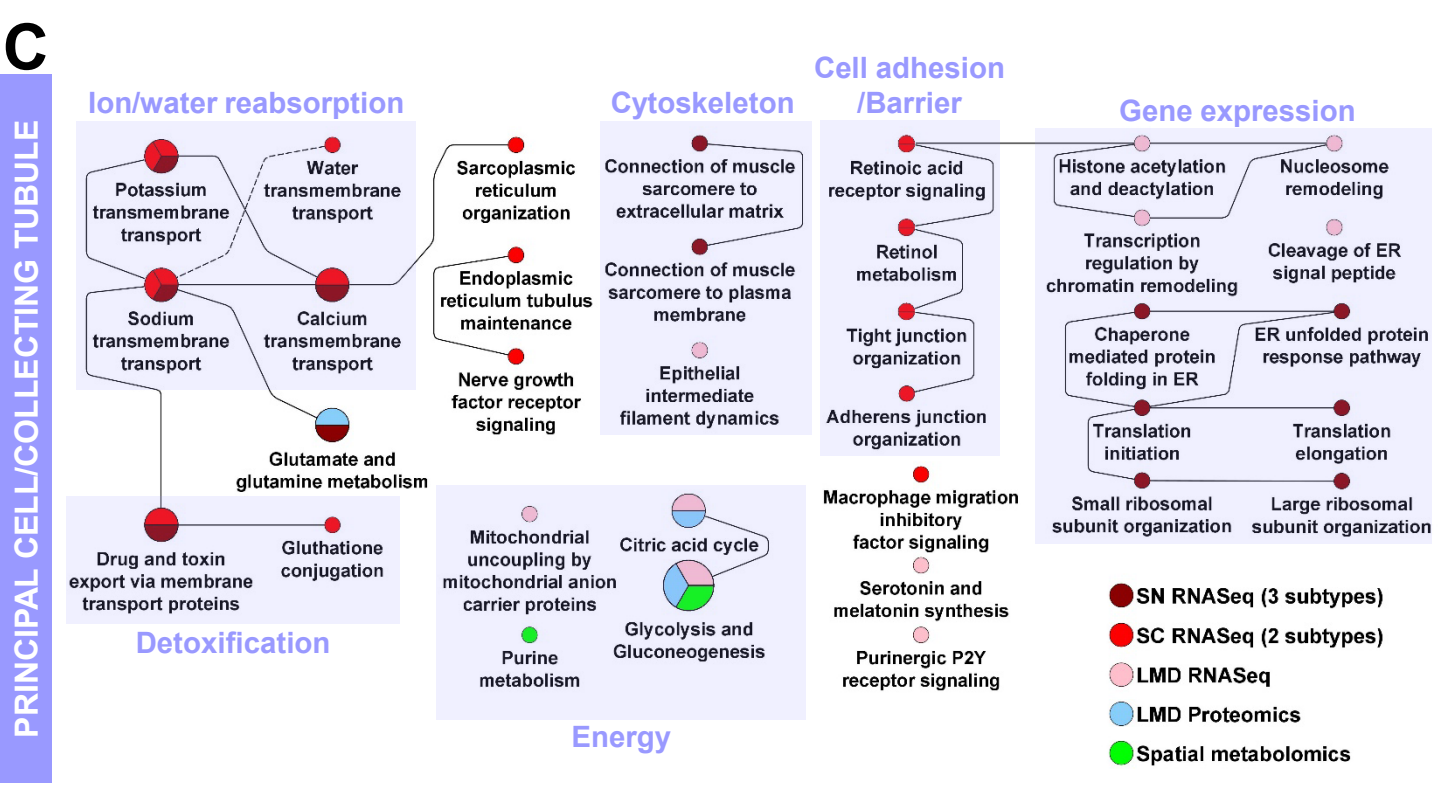

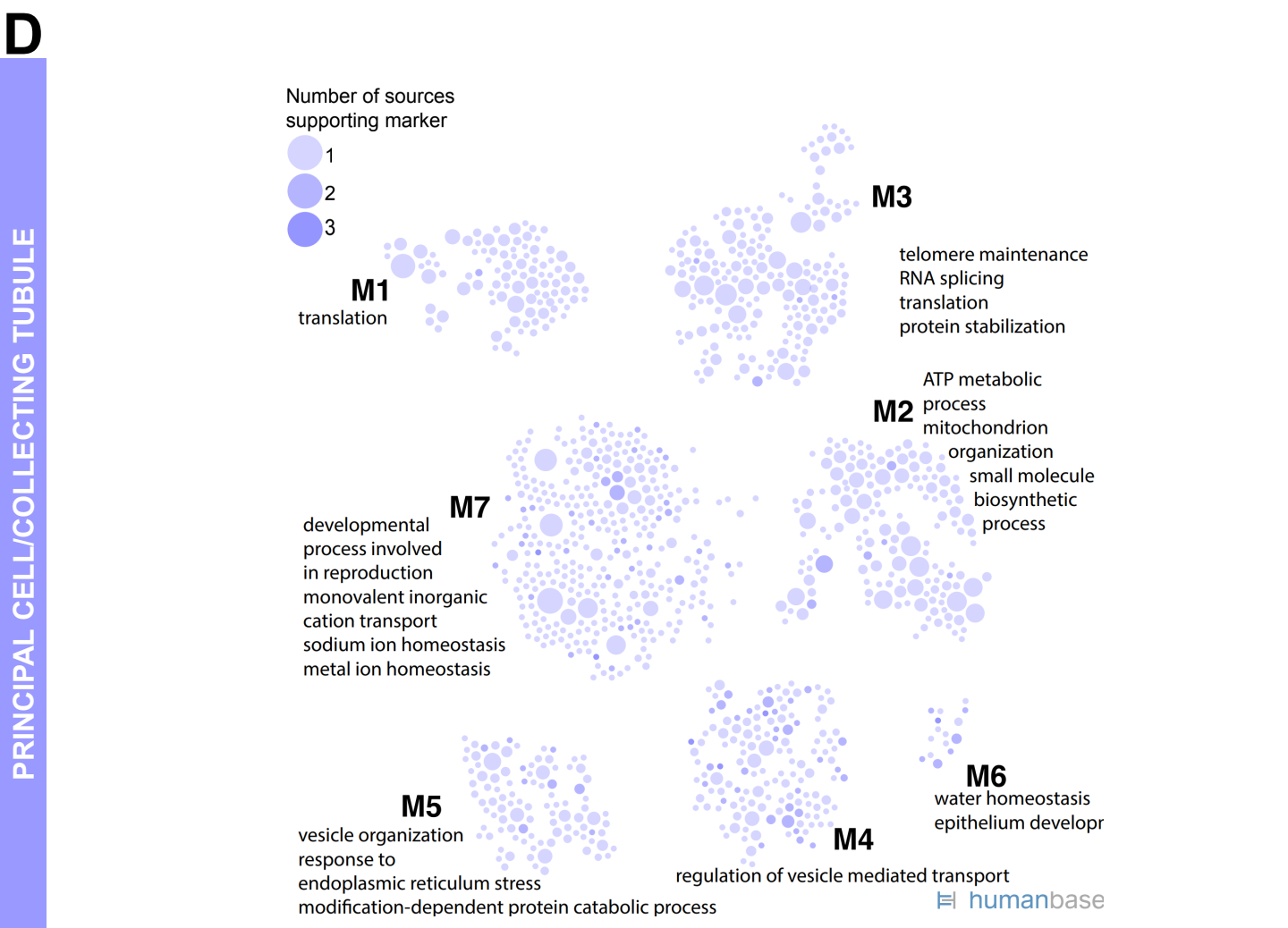

Supplemental Figure S12

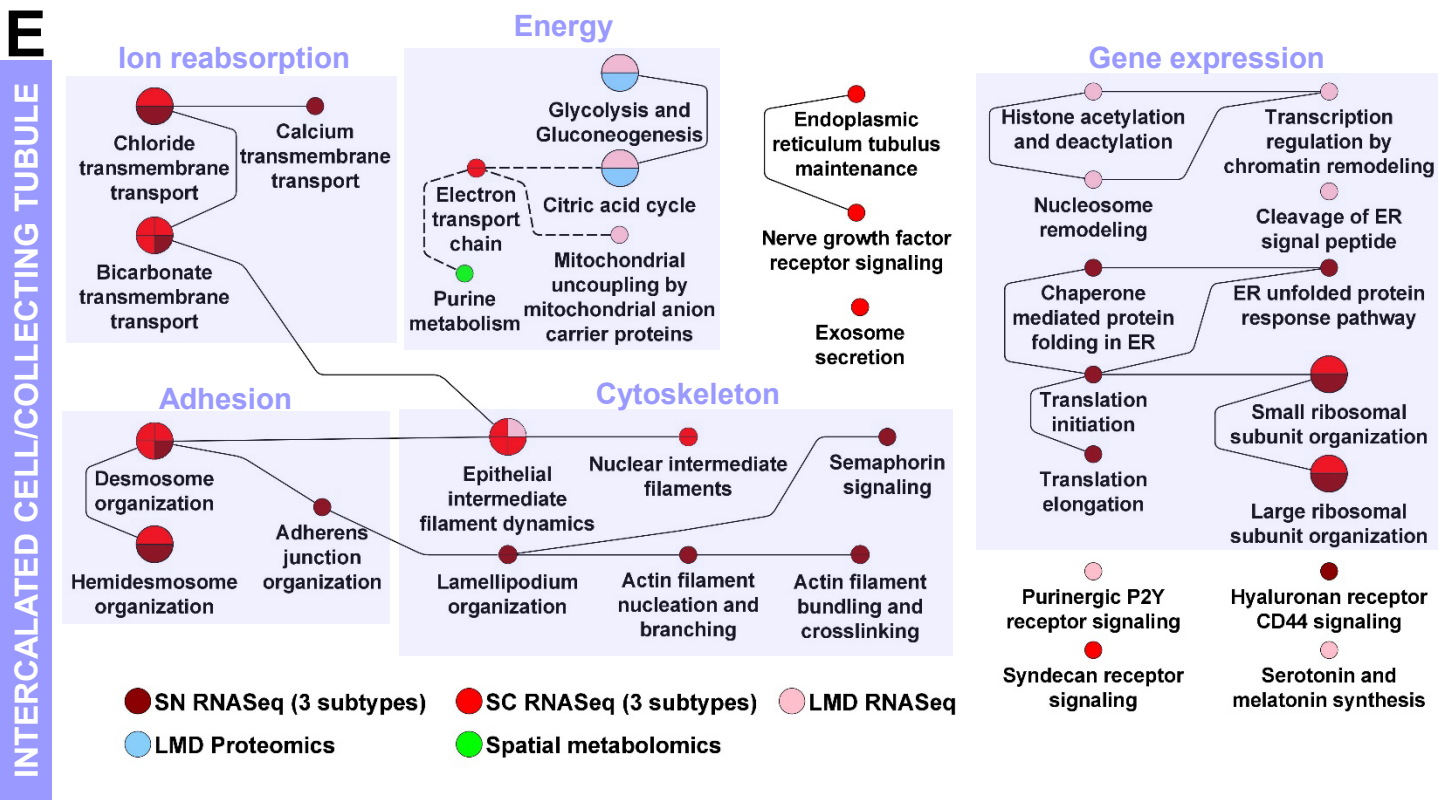

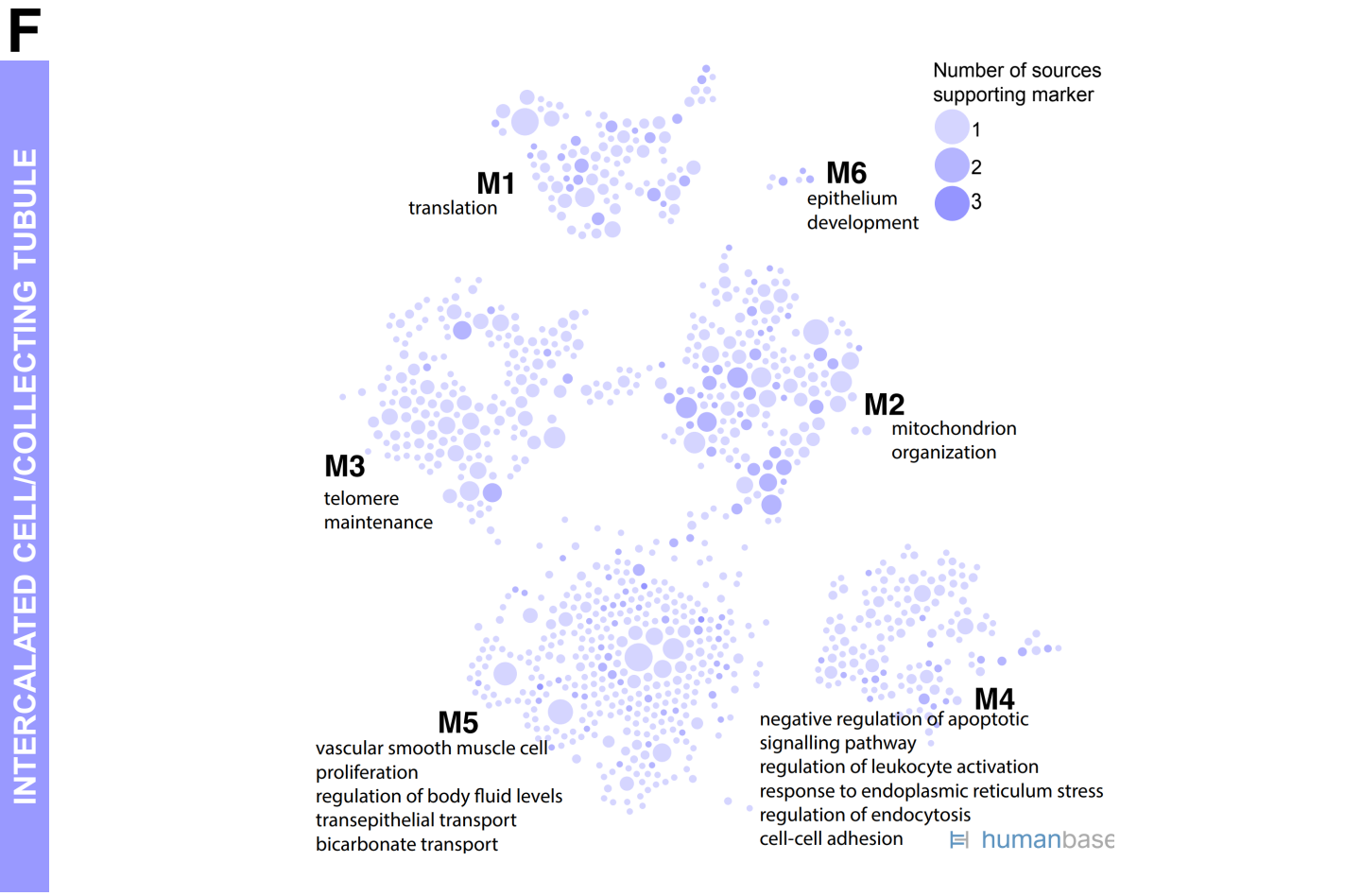

Supplemental Figure S12

G

INTERCALATED CELLs

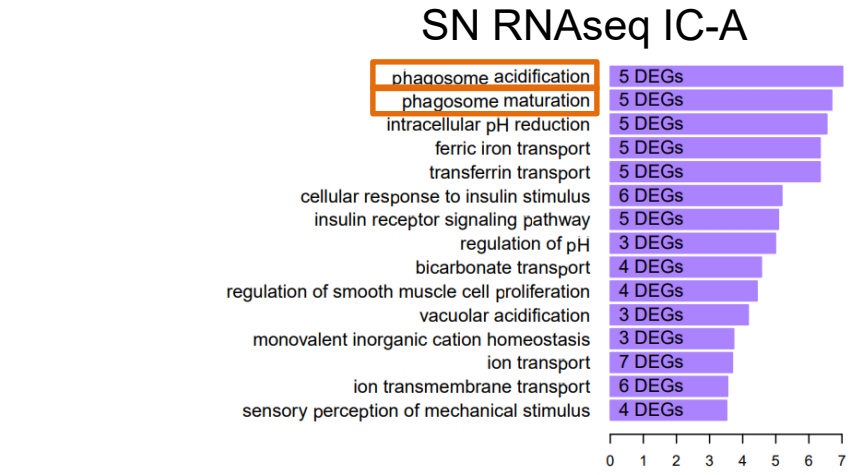

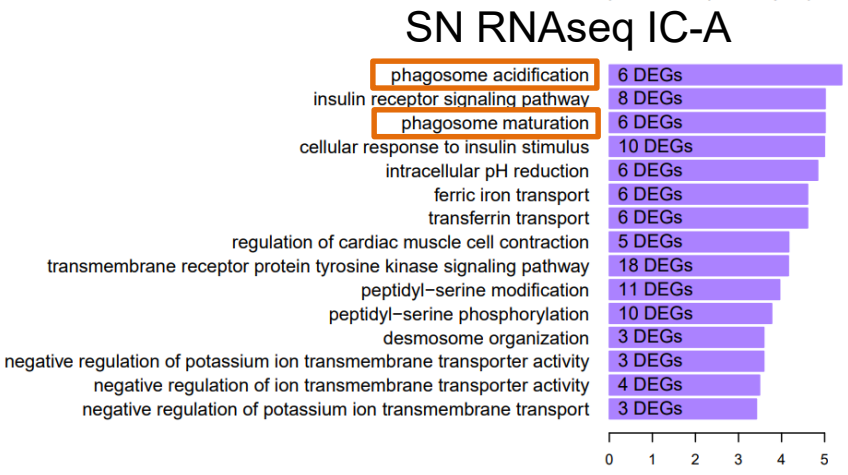

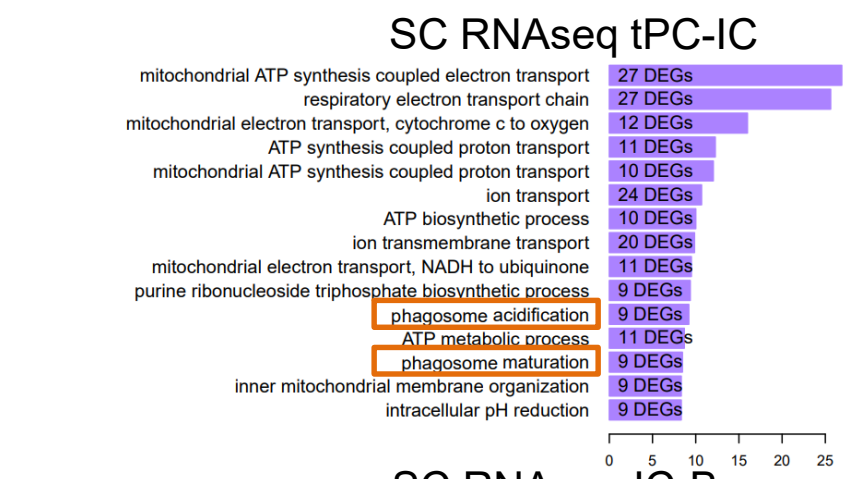

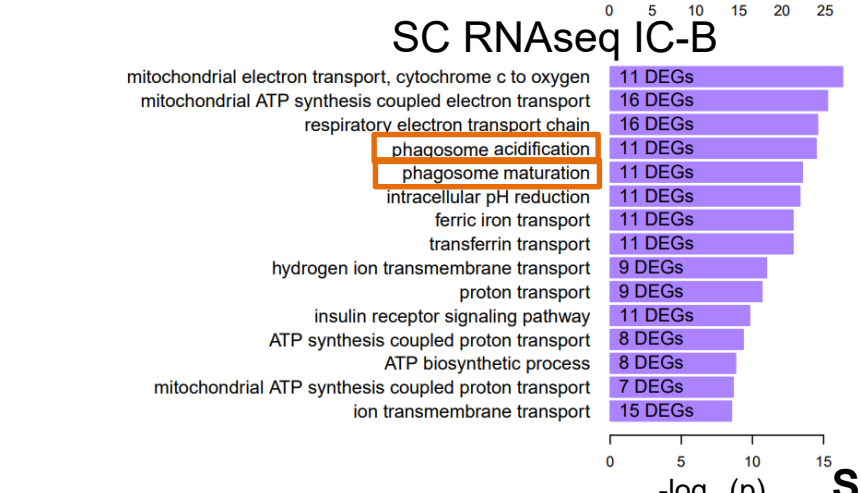

Supplemental Figure S12

Supplemental Figure S12: Enrichment analysis for the collecting duct. Connecting tubule cell specific DEGs were subjected to **(A)** dynamic enrichment and **(B)** module analysis. Principal cell and collecting duct specific DEGs were subjected to **(C)** dynamic enrichment and **(D)** module analysis. Intercalated cell and collecting duct specific DEGs were subjected to **(E)** dynamic enrichment and **(F)** module analysis. **(G)** Enrichment analysis of the marker genes for 4 different intercalated cell subtypes from sn and sc RNAseq using Gene Ontology Biological Processes identifies the pathways 'Phagosome acidification' and 'Phagosome maturation'.

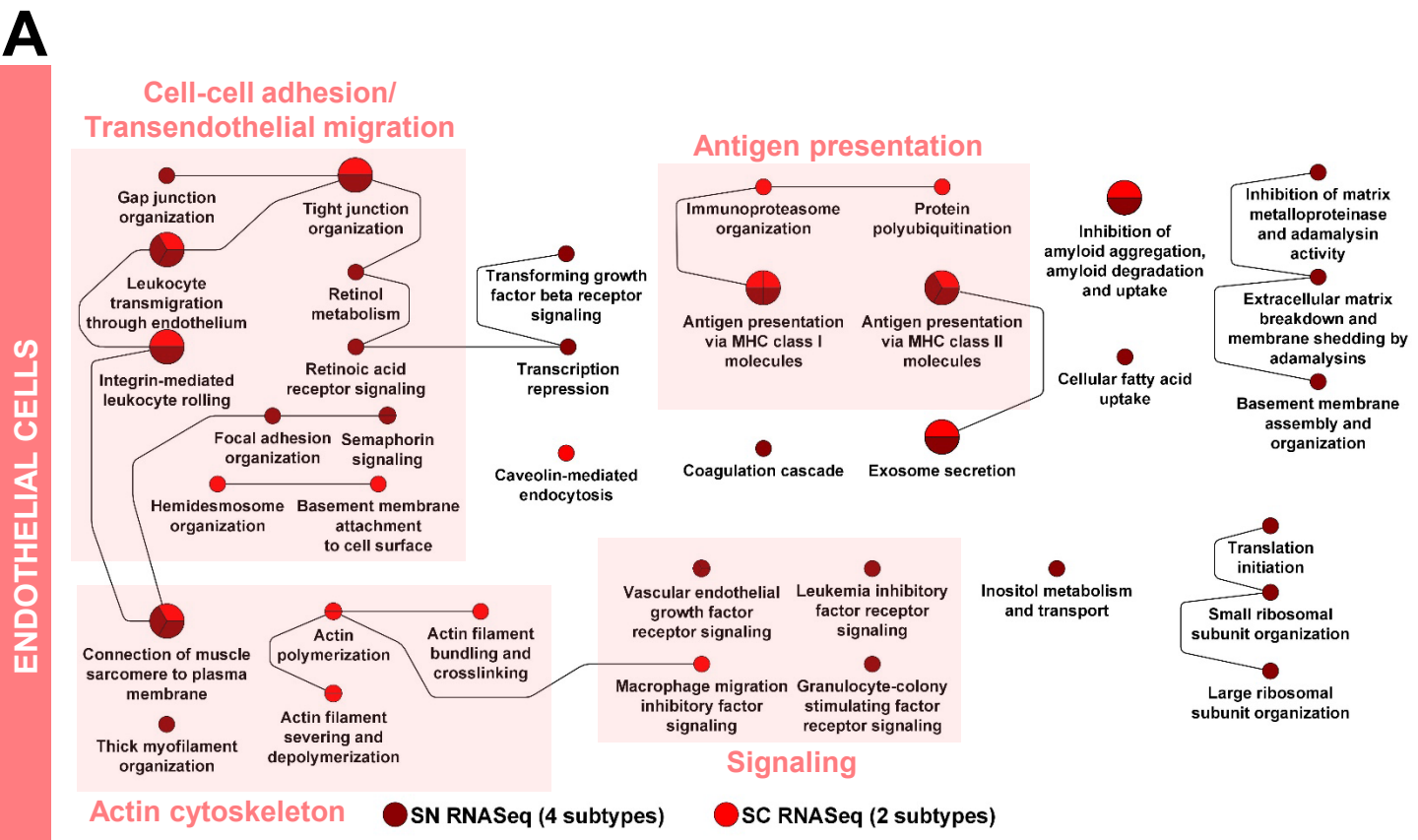

Supplemental Figure S13

Supplemental Figure S13: Enrichment analysis for vascular cells. (A) Endothelial cell specific DEGs were subjected to dynamic enrichment. **(B)** Similarly, vascular smooth muscle cell specific DEGs were subjected to dynamic enrichment analysis.

NON-IMMUNE INTERSTITIAL CELLS

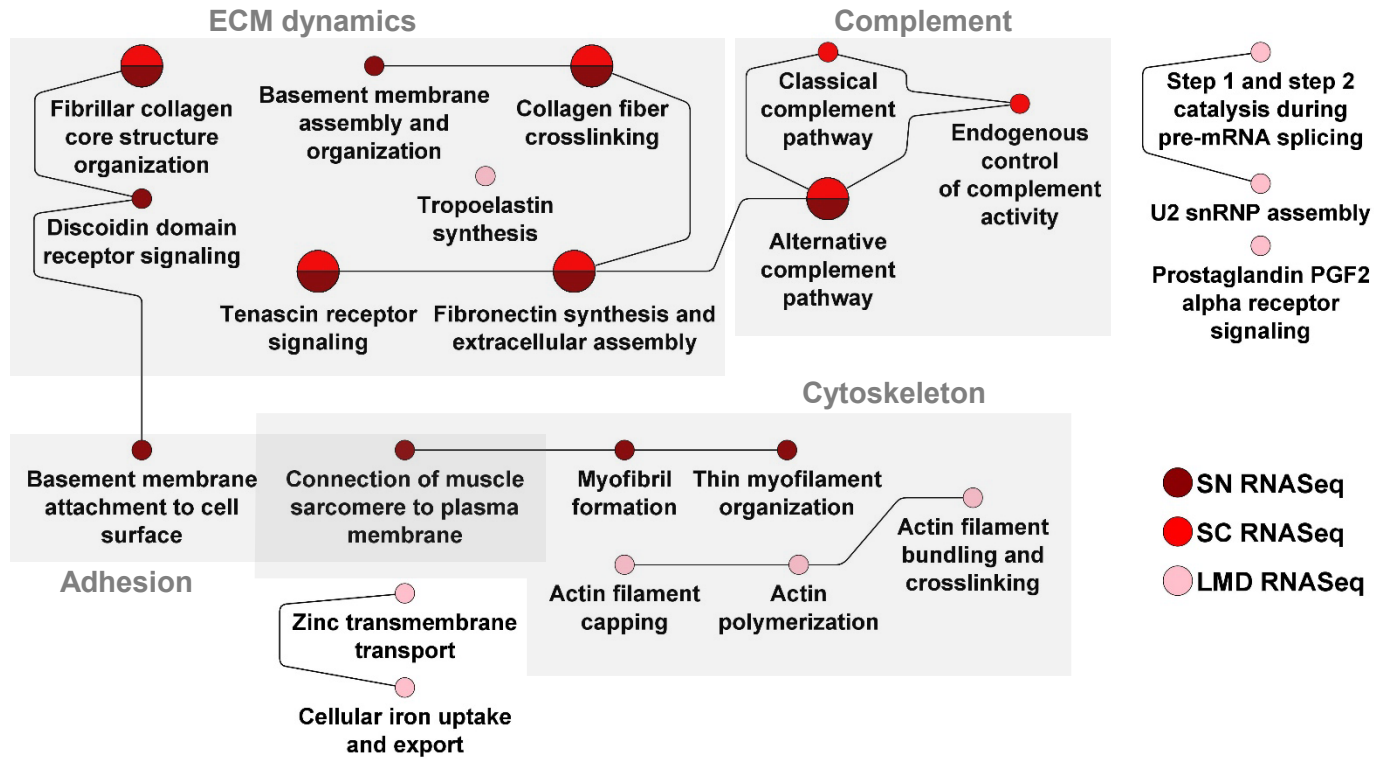

Supplemental Figure S14

Supplemental Figure S14: Enrichment analysis for interstitial cells. Interstitial fibroblast cell and segment specific DEGs were subjected to dynamic enrichment analysis.

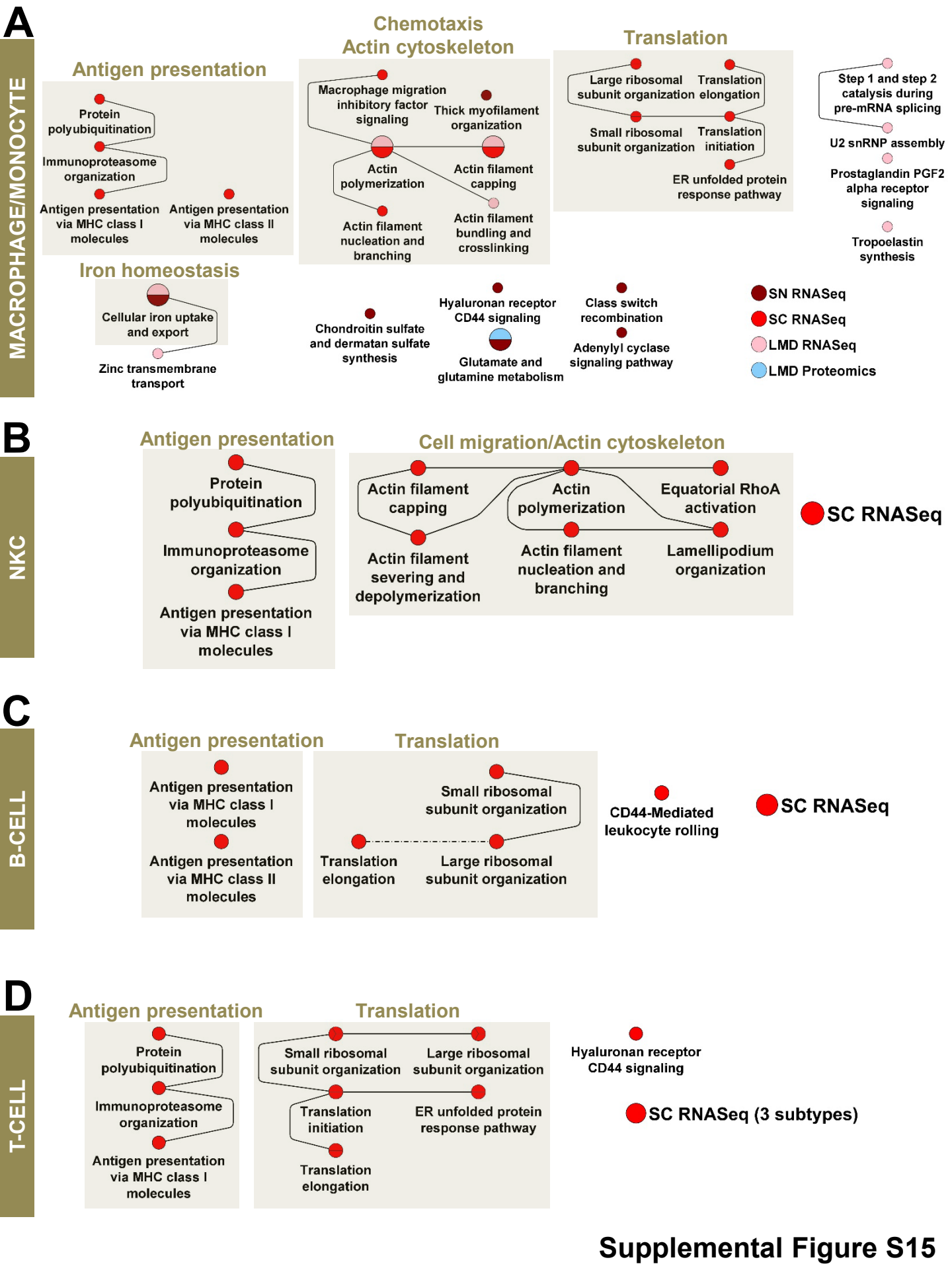

Supplemental Figure S15

Supplemental Figure S15: Enrichment analysis for immune cells. (A) Macrophage/Monocyte, **(B)** Natural Killer cell, **(C)** B-cell, and **(D)** T-cell specific DEGs were subjected to dynamic enrichment analysis.

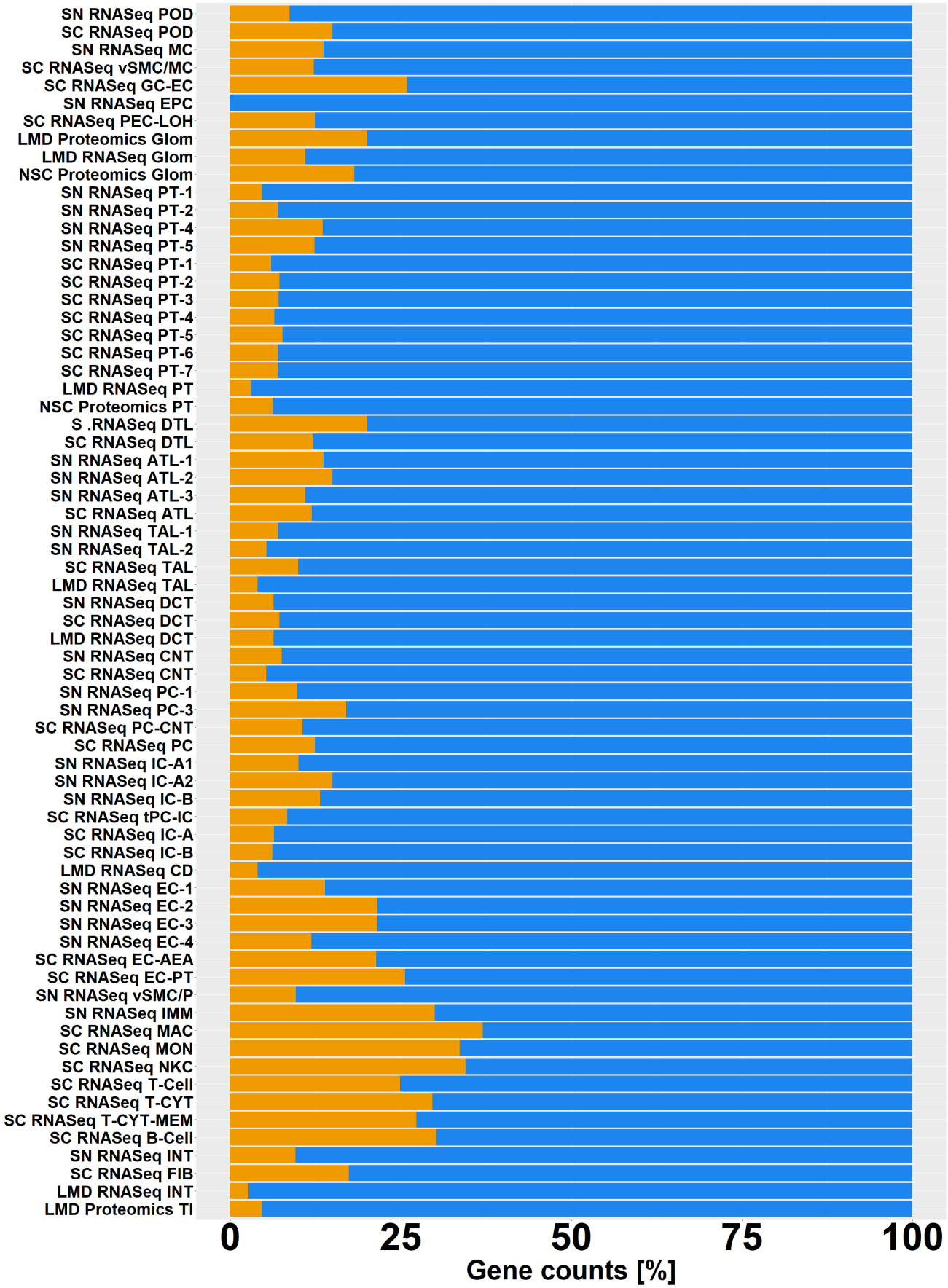

Supplemental Figure S16

Supplemental Figure S16: Expression of immune related genes in the kidney cell types. Using all genes that are assigned to the Gene Ontology Biological Process “immune system process” or any of its children processes based on the “is_a” or “part_of” relationships, we documented the percentage of immune system related genes (orange) in all cell type, subtype and segment-specific marker genes and proteins. See figure 2A for cell type abbreviations.

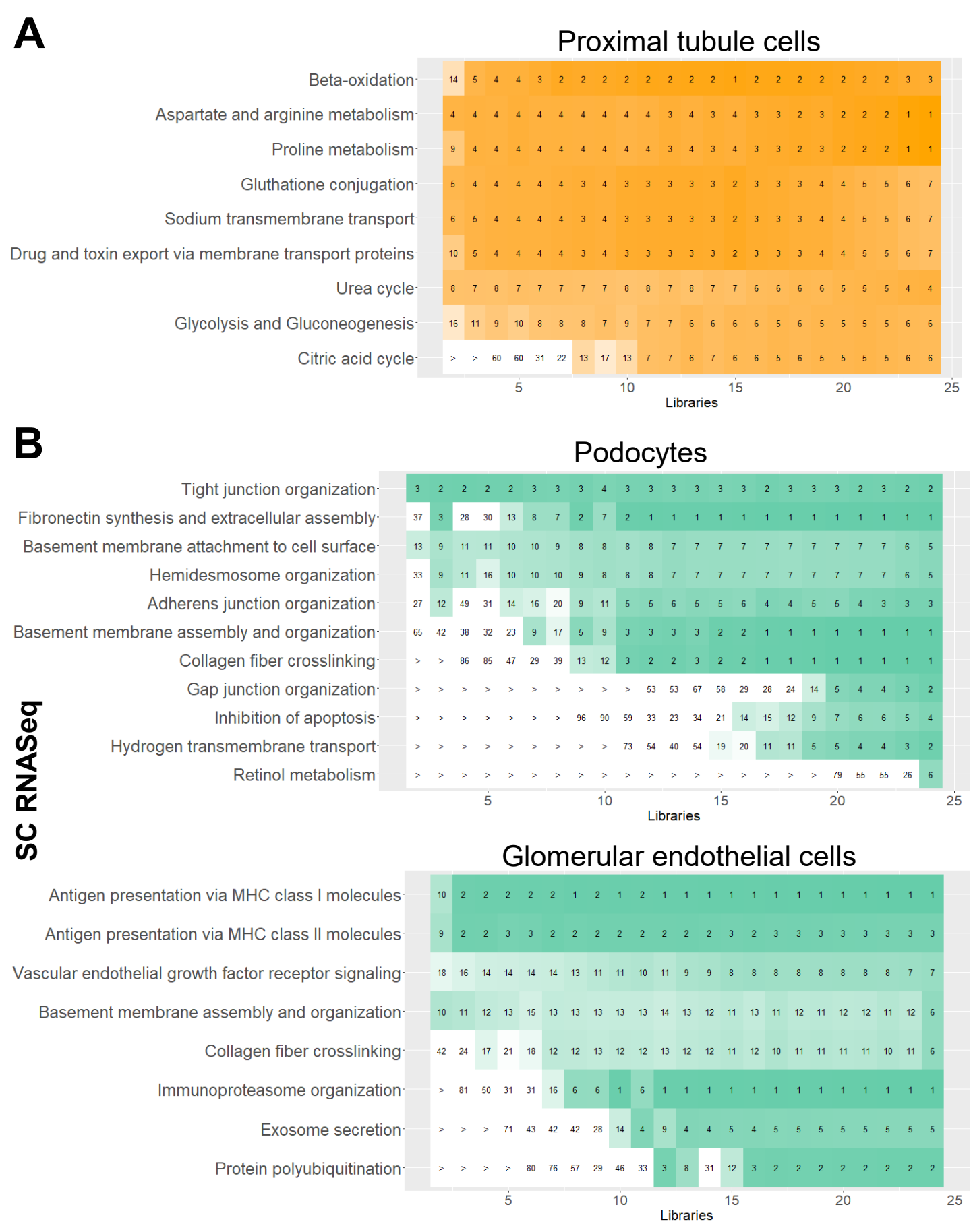

Supplemental Figure S17

C

SC RNASeq

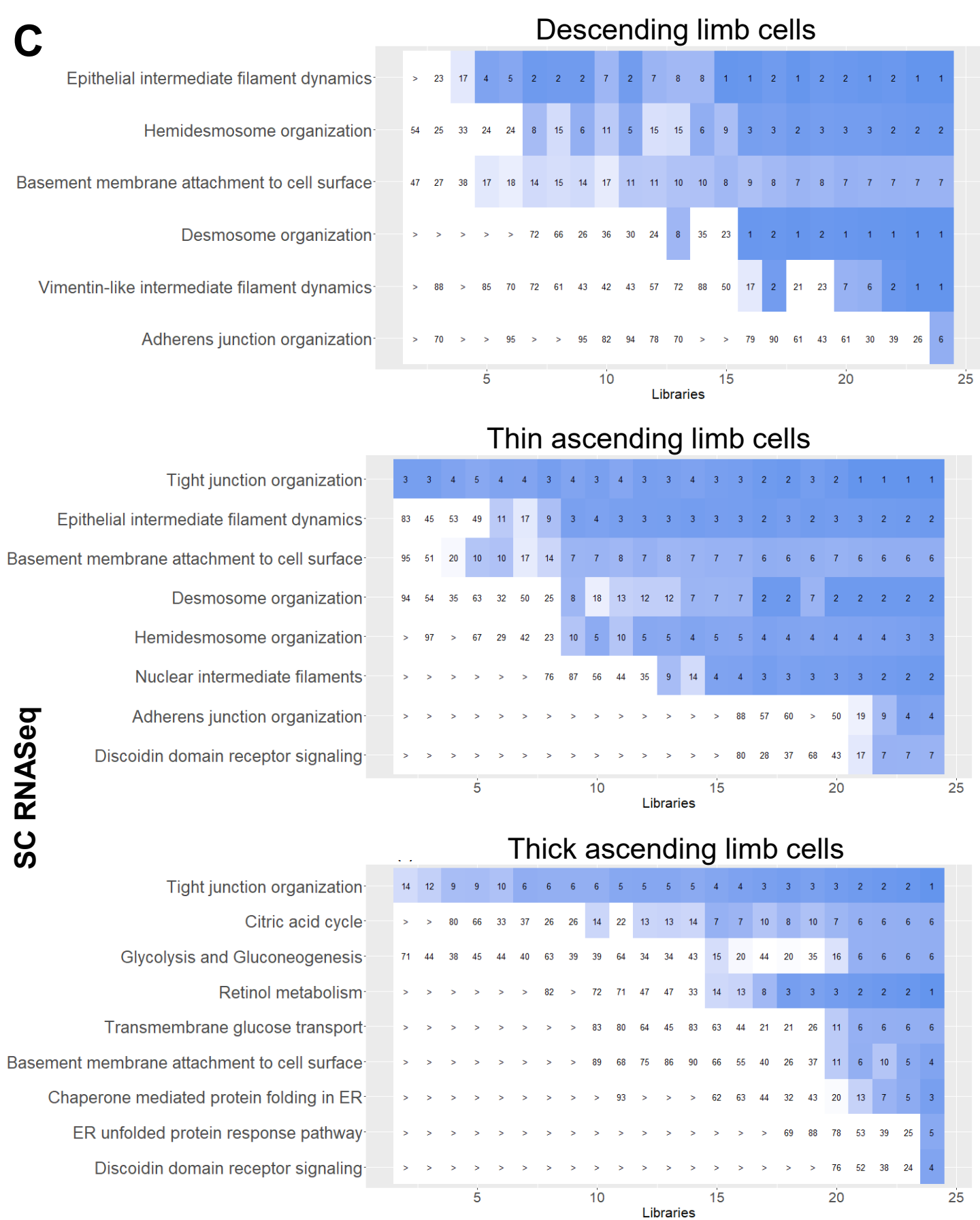

Supplemental Figure S17

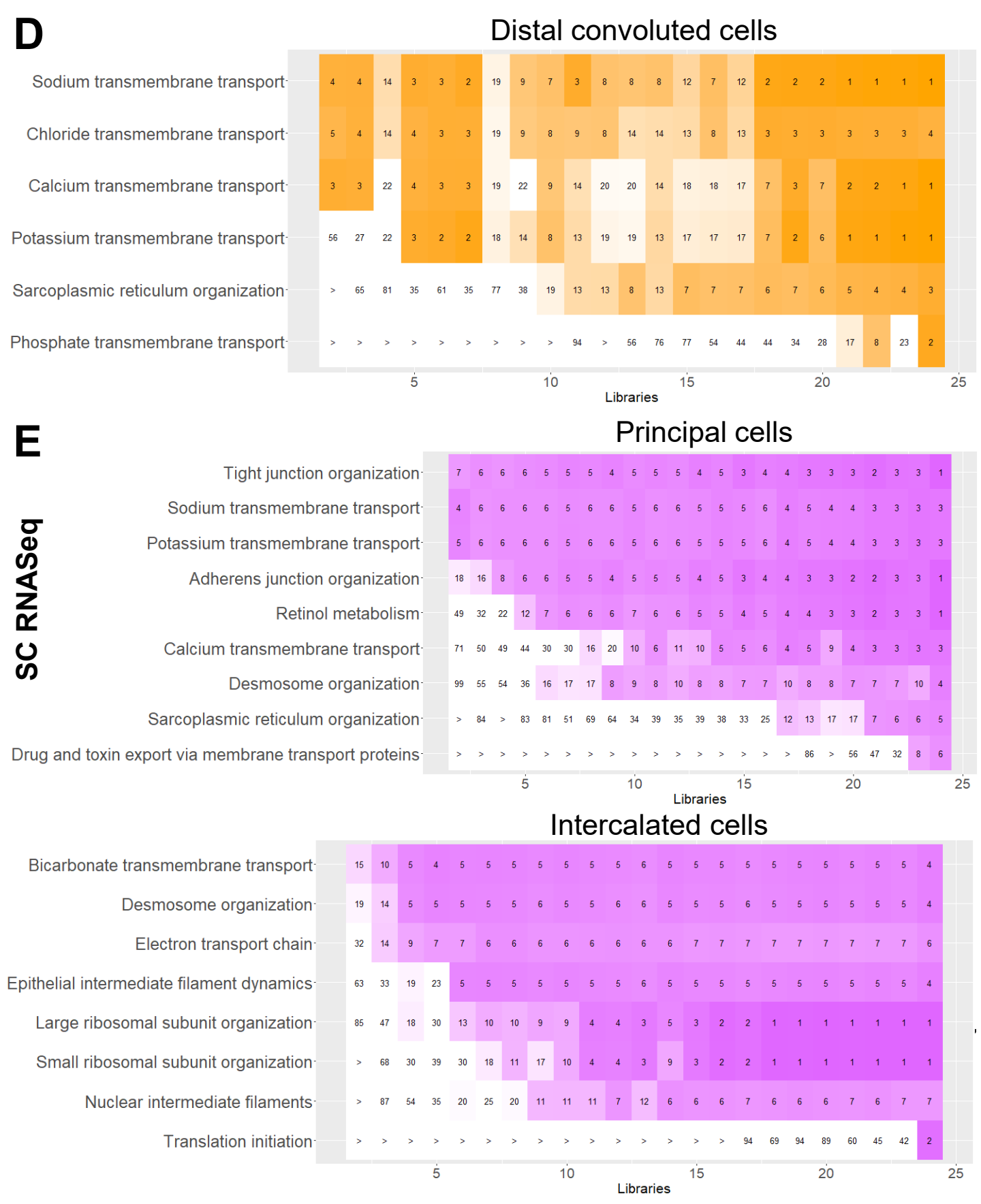

Supplemental Figure S17

F

SC RNASeq

Endothelial cells – Afferent/Efferent Arteriole

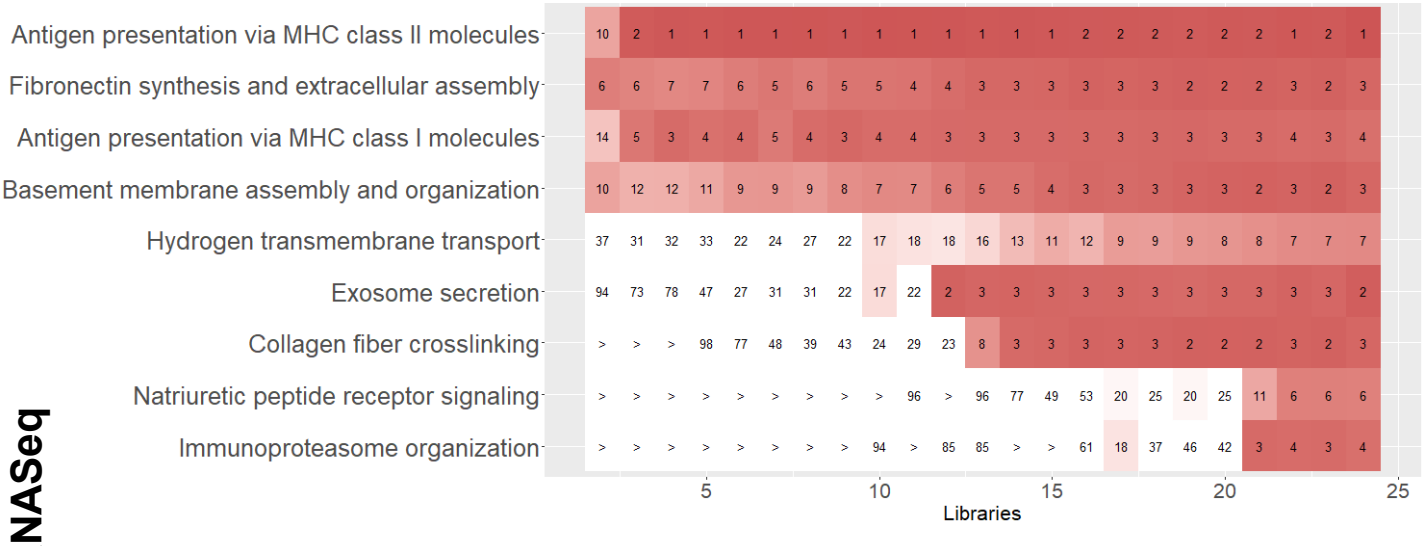

Endothelial cells – descending vasa recta/afferent/efferent arteriole

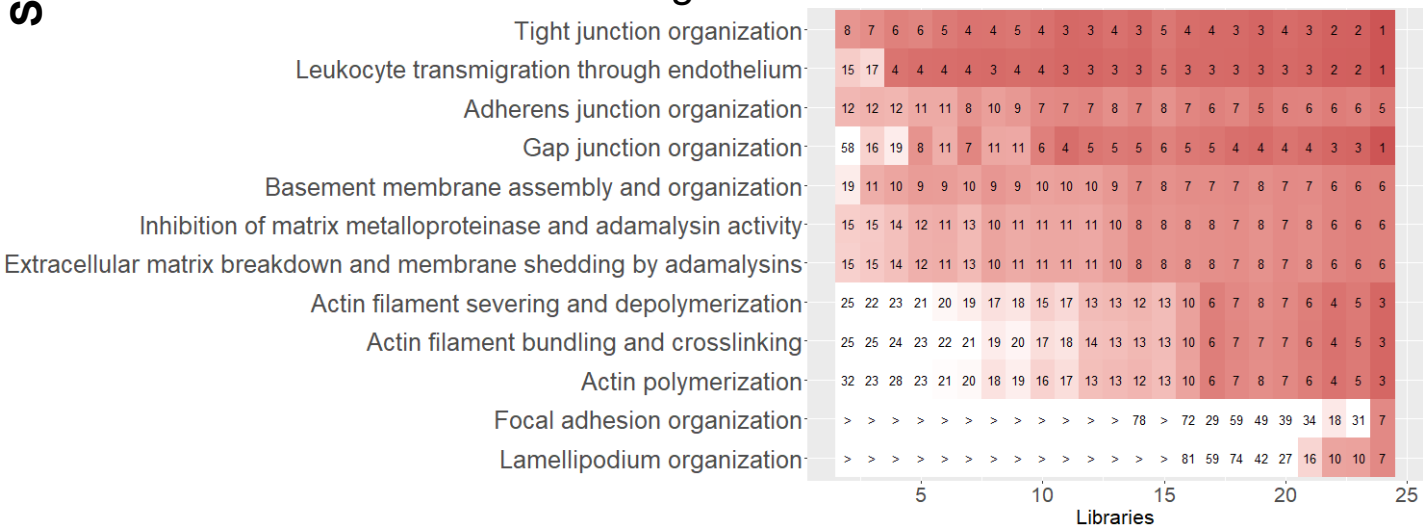

G

Interstitial cells

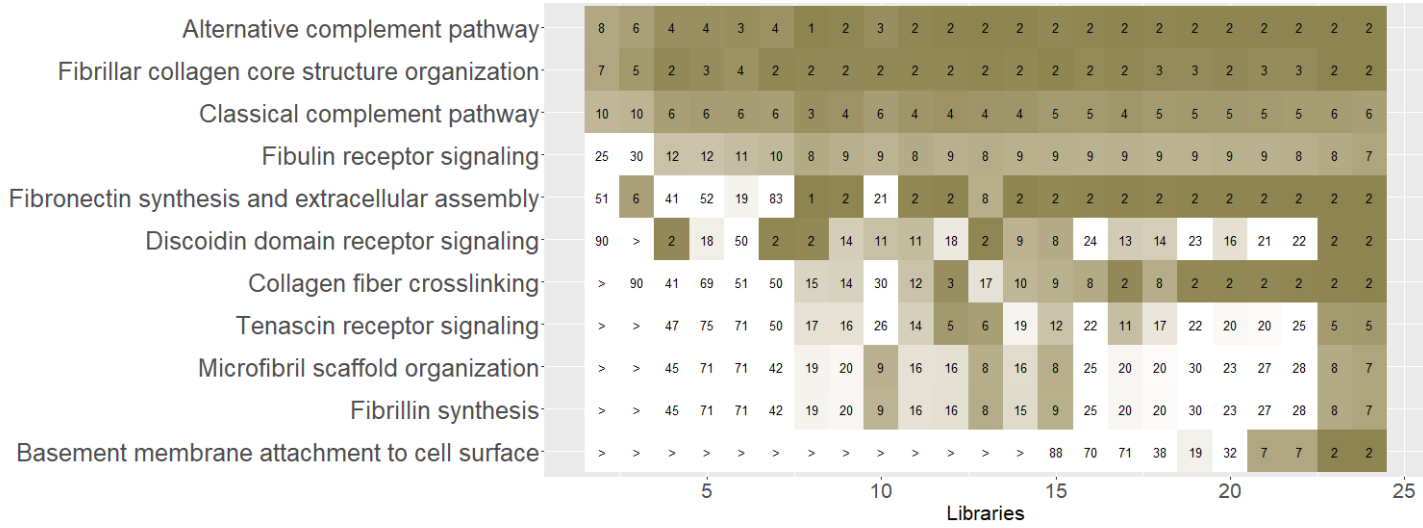

Supplemental Figure S17

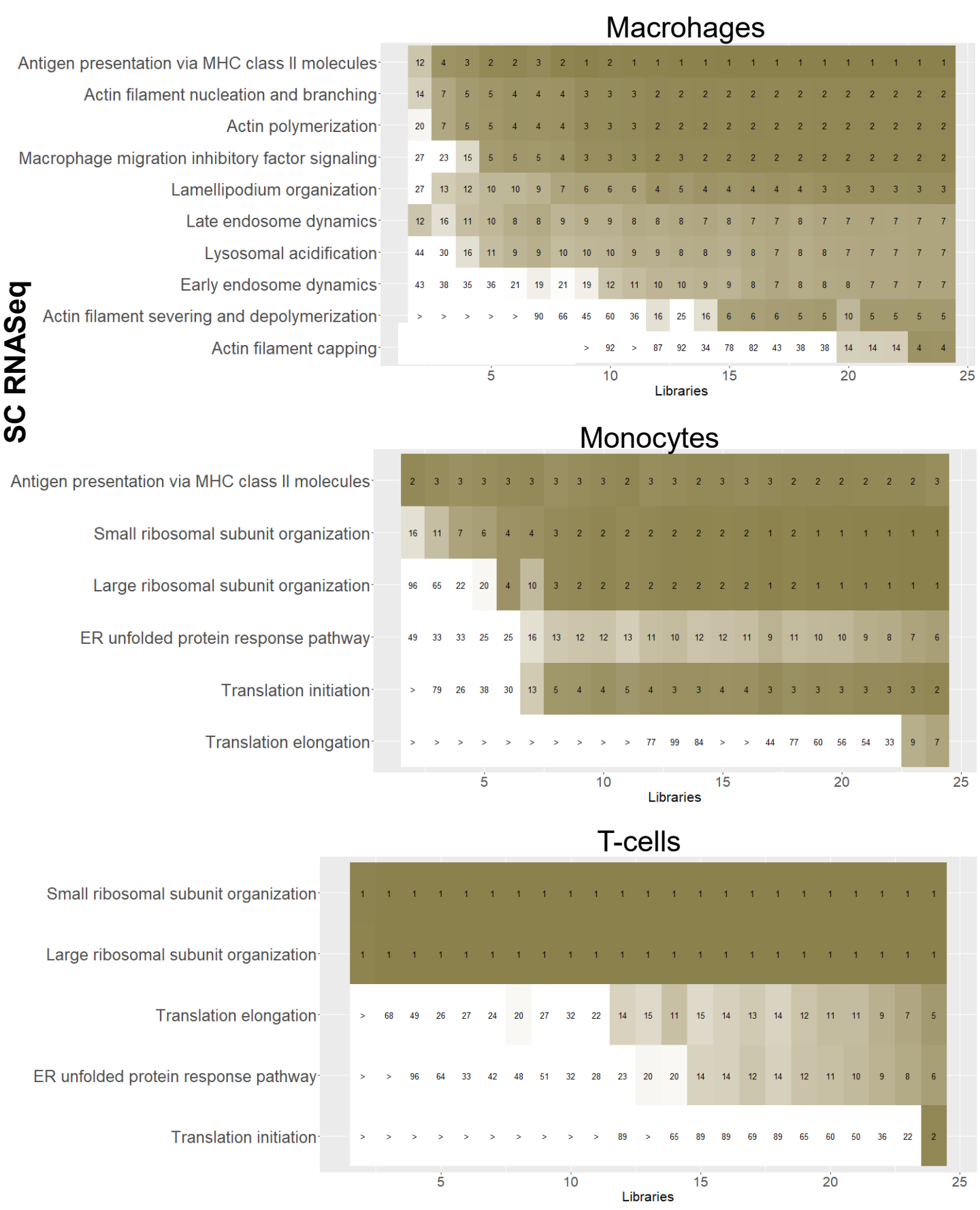

Supplemental Figure S17

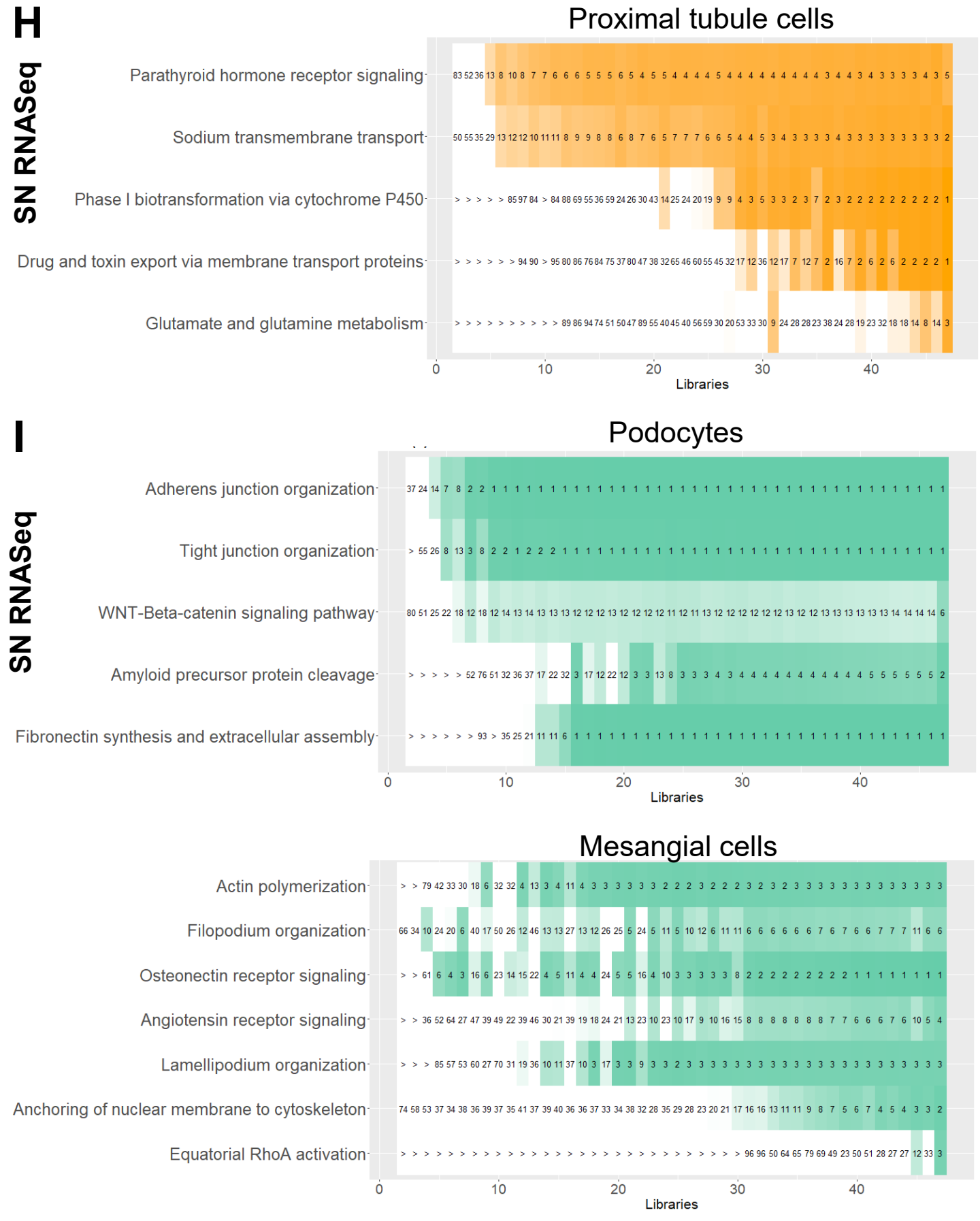

Supplemental Figure S17

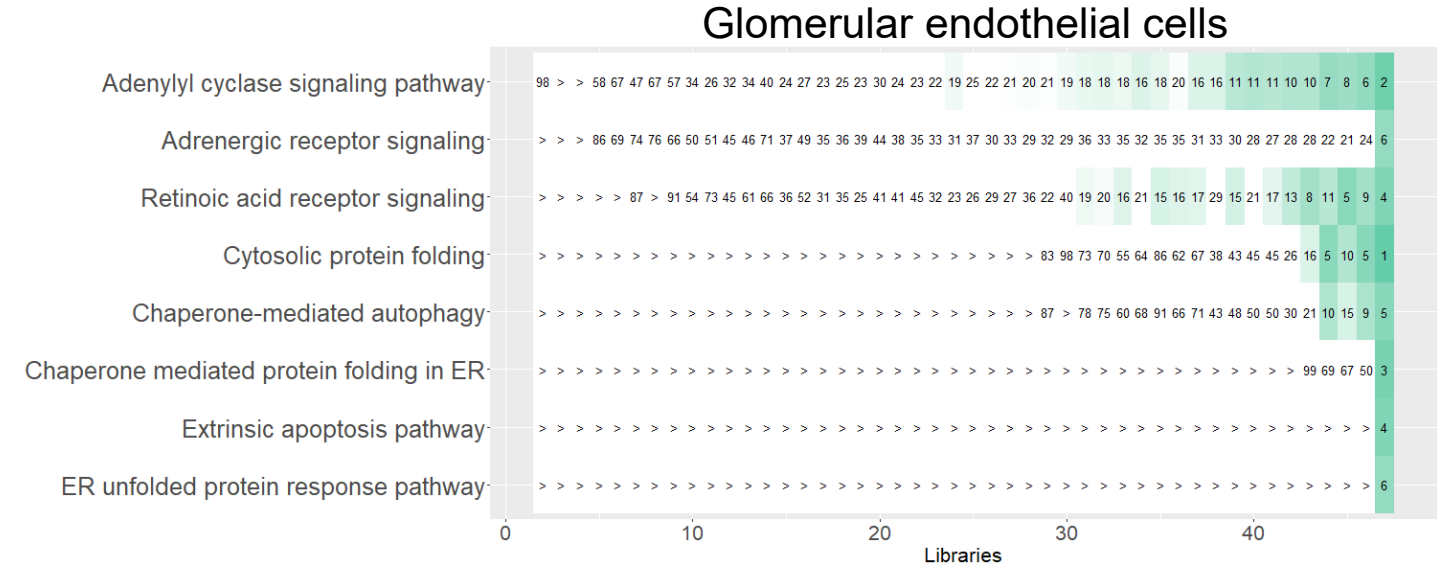

J

SN RNASeq

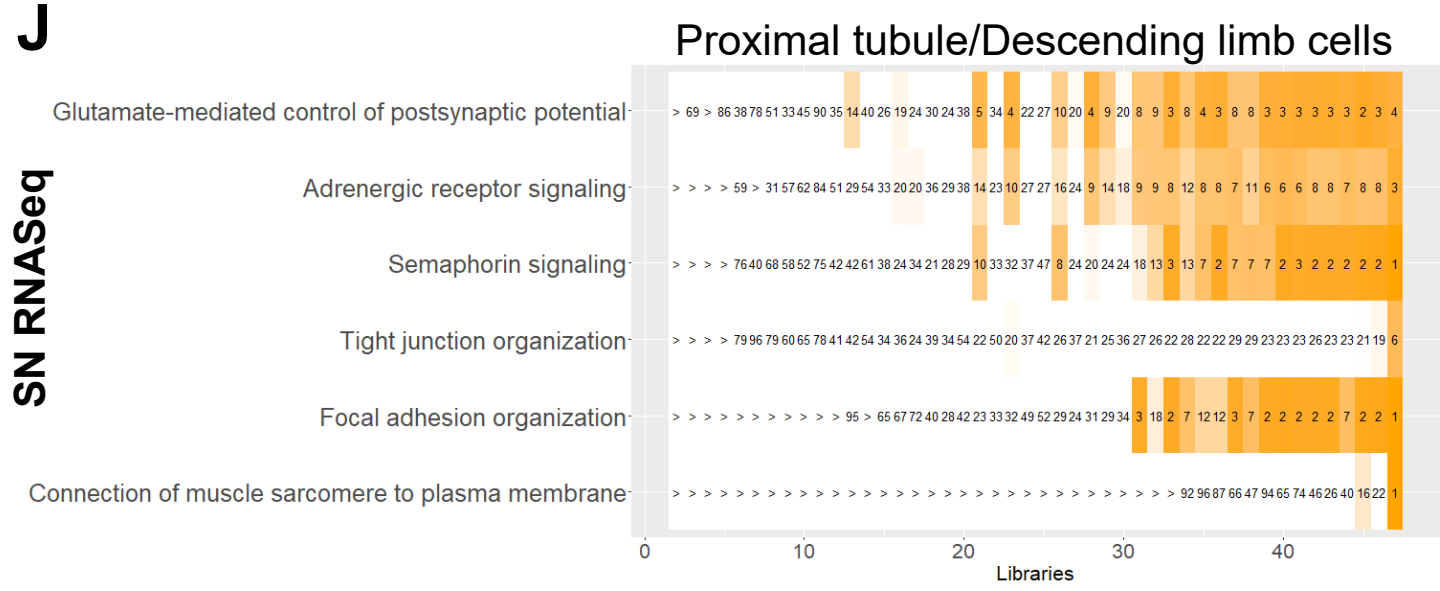

K

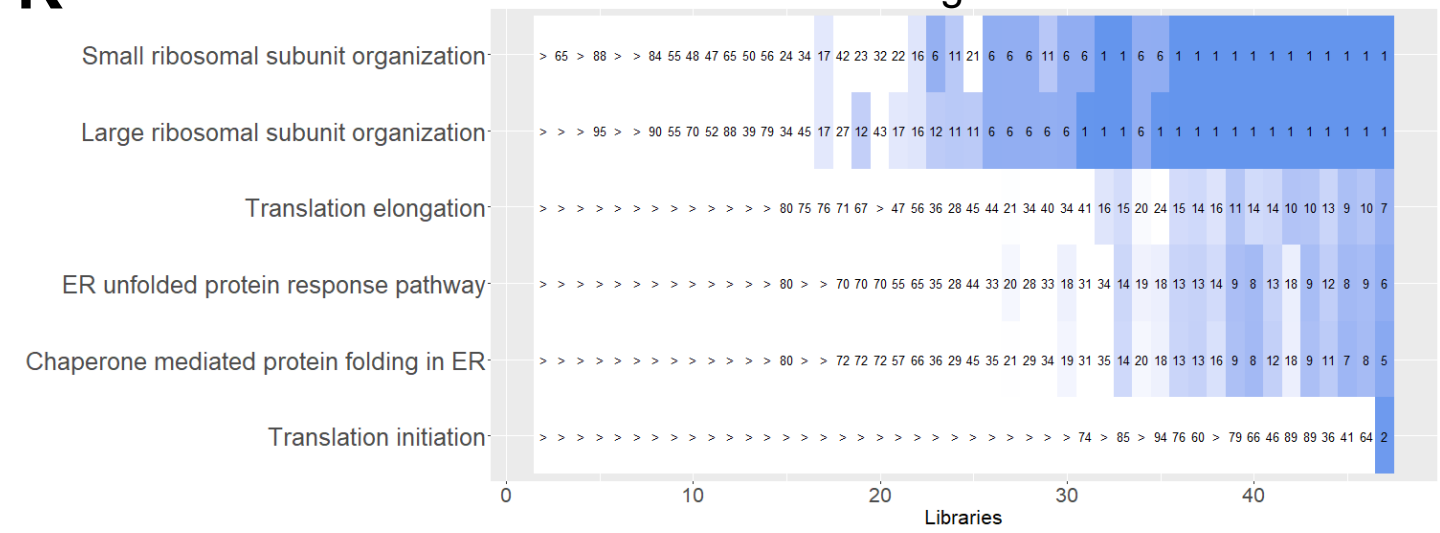

Supplemental Figure S17

SN RNASeq

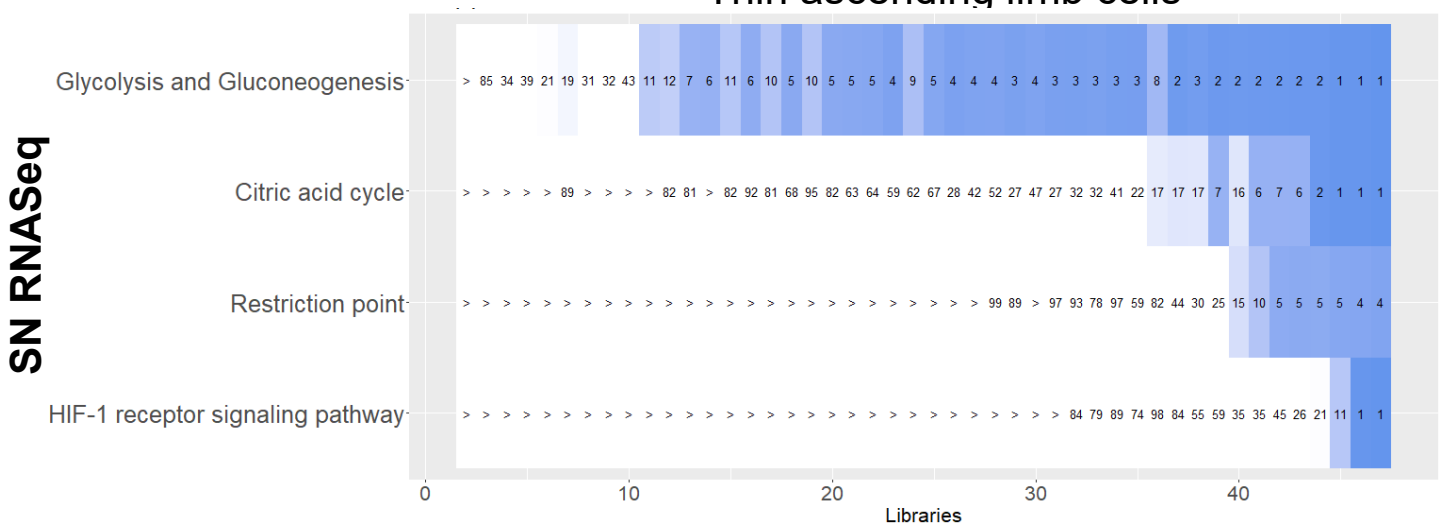

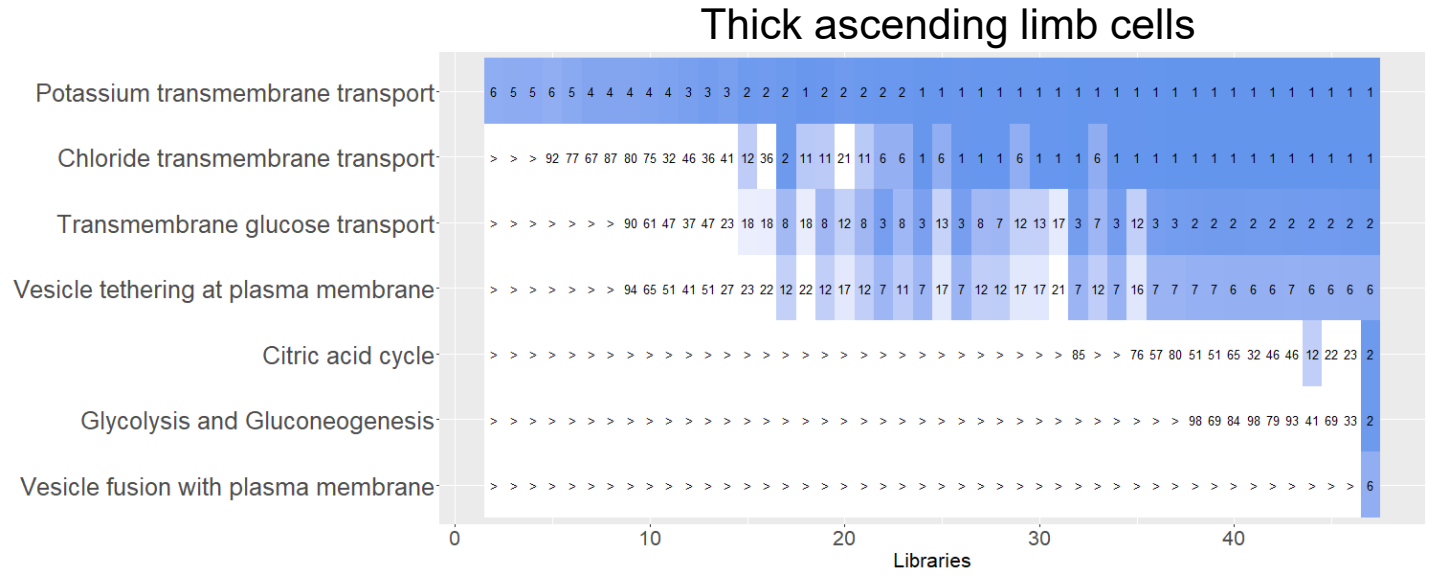

L

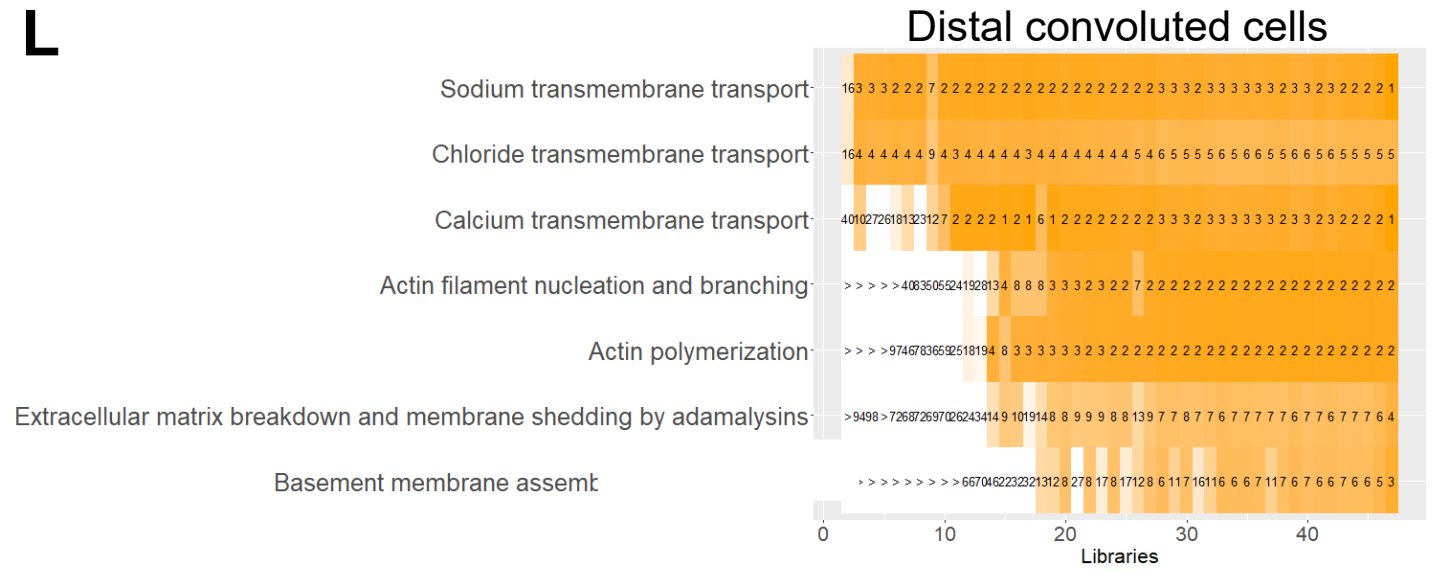

Supplemental Figure S17

M

SN RNASeq

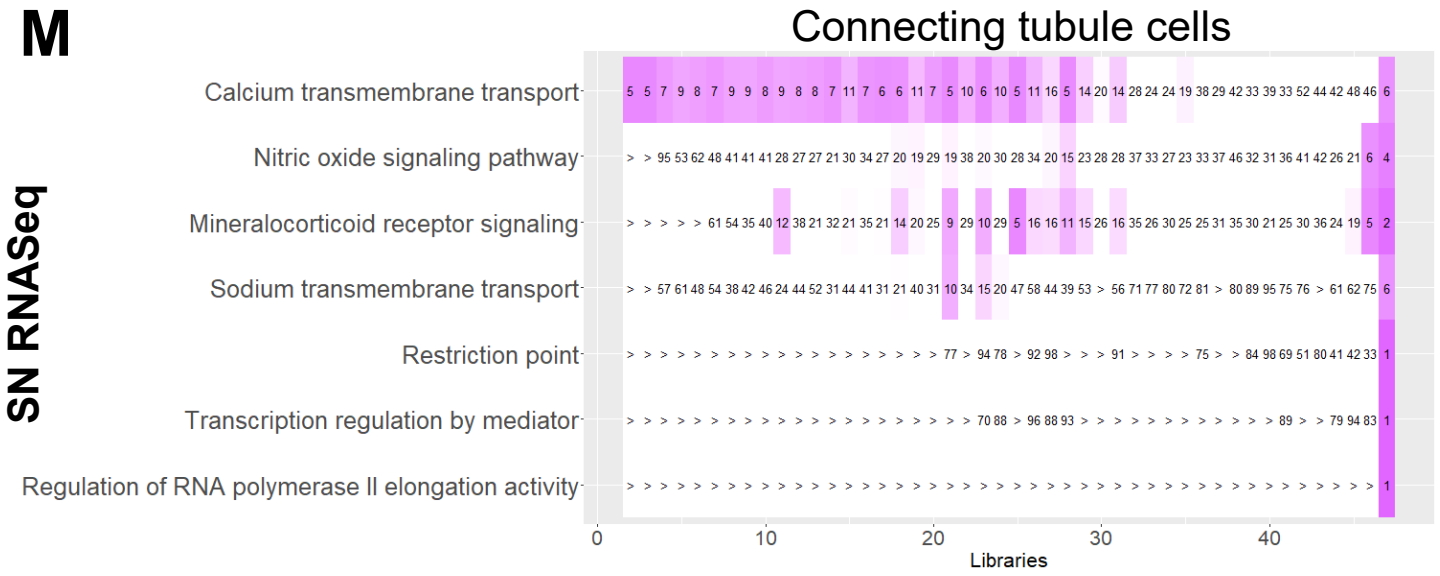

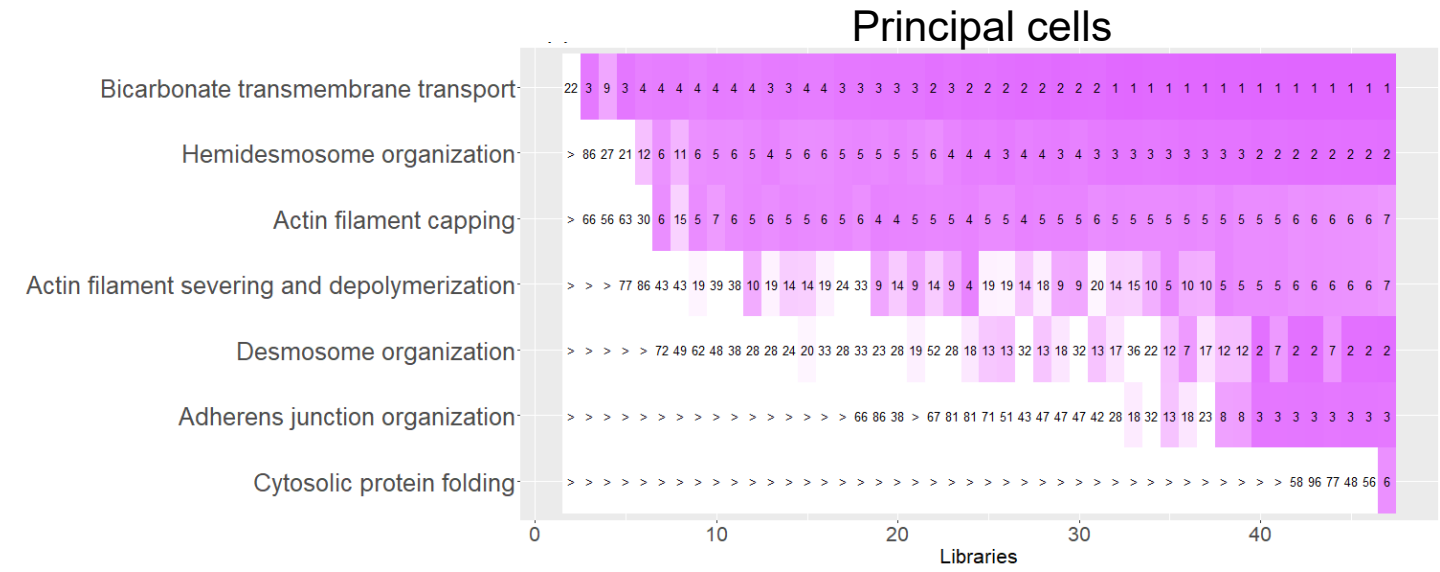

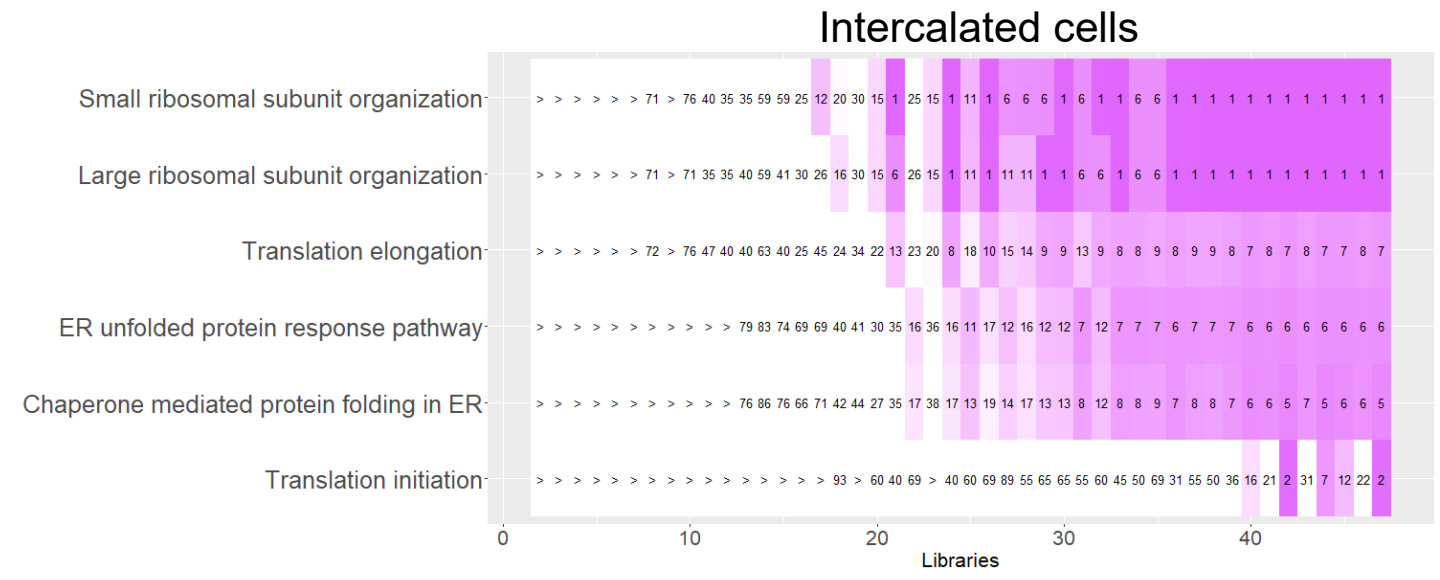

Supplemental Figure S17

N

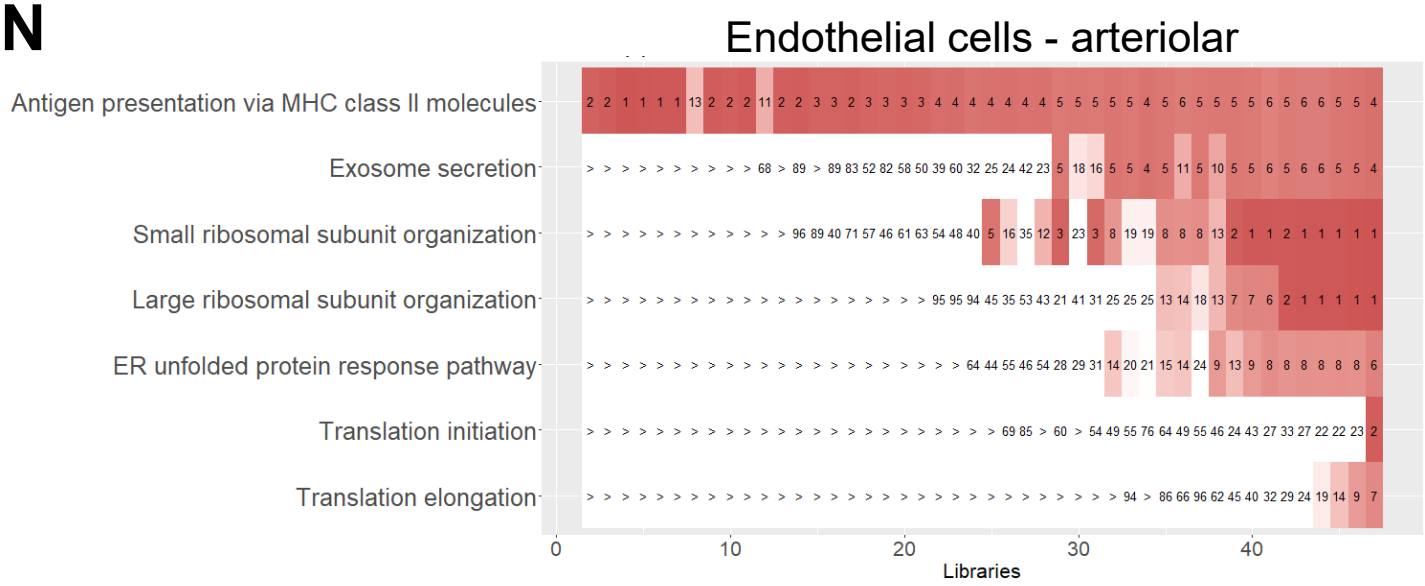

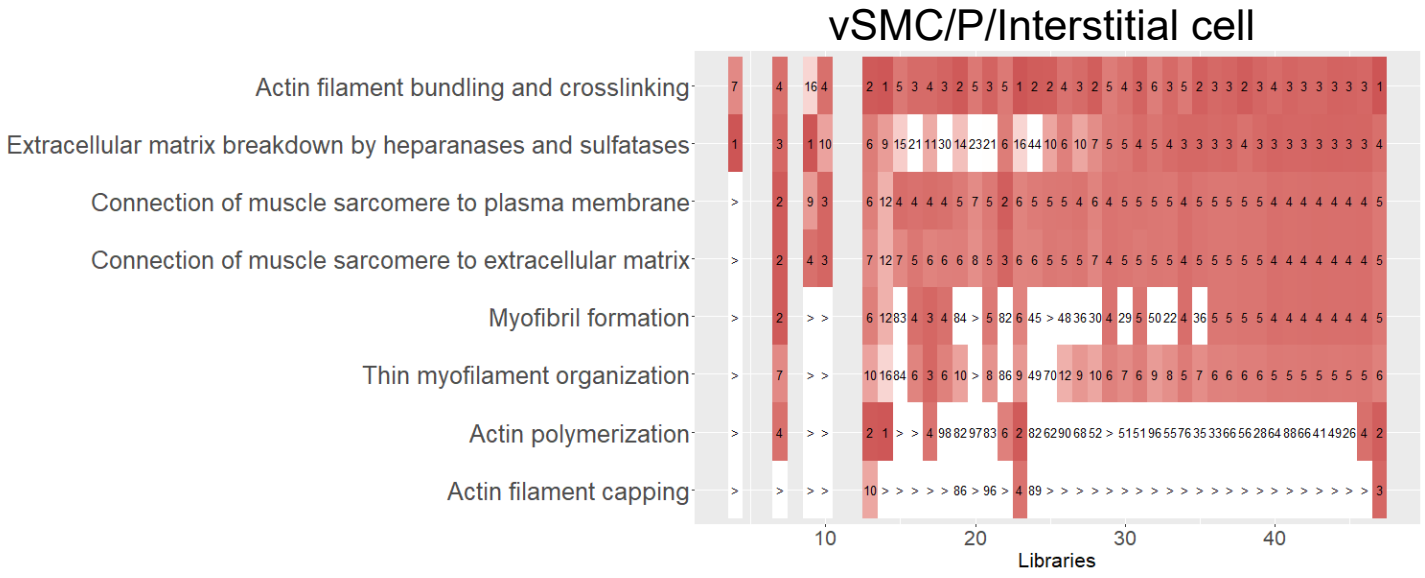

Supplemental Figure S17

Supplemental Figure S17: Cellular key functions are most consistently predicted by downsampled sc and sn RNAseq datasets. To analyze the reliability of predicted cell type-specific biology we subjected the top 300 cell-type specific marker genes that were obtained from the full or down-sampled sc and sn RNAseq datasets (Suppl. Figure 5C and 5D, respectively) to dynamic enrichment analysis. SCPs that were among the top seven predictions for the complete sc and sn RNAseq were identified. We identified the dynamic enrichment ranks of these SCPs in the down-sampled datasets and averaged them across all datasets with the same number of libraries. Color scale ranges from 1 (dark green/orange/purple) to 21 or higher (white). Notify that SCPs predicted for the complete datasets are not necessarily the same as the one documented in figure 6. The 2124, 4447 and 721 individual complete and downsampled datasets were analyzed using our automated pipeline that did not allow manual *ad hoc* optimization and merged all clusters annotated to the same cell type instead of annotating each cluster to a cell subtype. The first set of subfigures shows the predicted SCPs identified from the sc RNAseq dataset for **(A)** proximal tubule cells, **(B)** glomerular cell types, **(C)** cell types of the Loop of Henle, **(D)** of the distal convoluted tubule, **(E)** of the collecting duct, **(F)** vascular cells and **(G)** non-immune and immune interstitial cells. The second set of subfigures shows the predicted SCPs identified from the sn RNAseq dataset for **(H)** proximal tubule cells, **(I)** glomerular cell types, **(J)** proximal tubule/descending limb cell, **(K)** cell types of the Loop of Henle, **(L)** of the distal convoluted tubule, **(M)** of the collecting duct and **(N)** vascular cells.

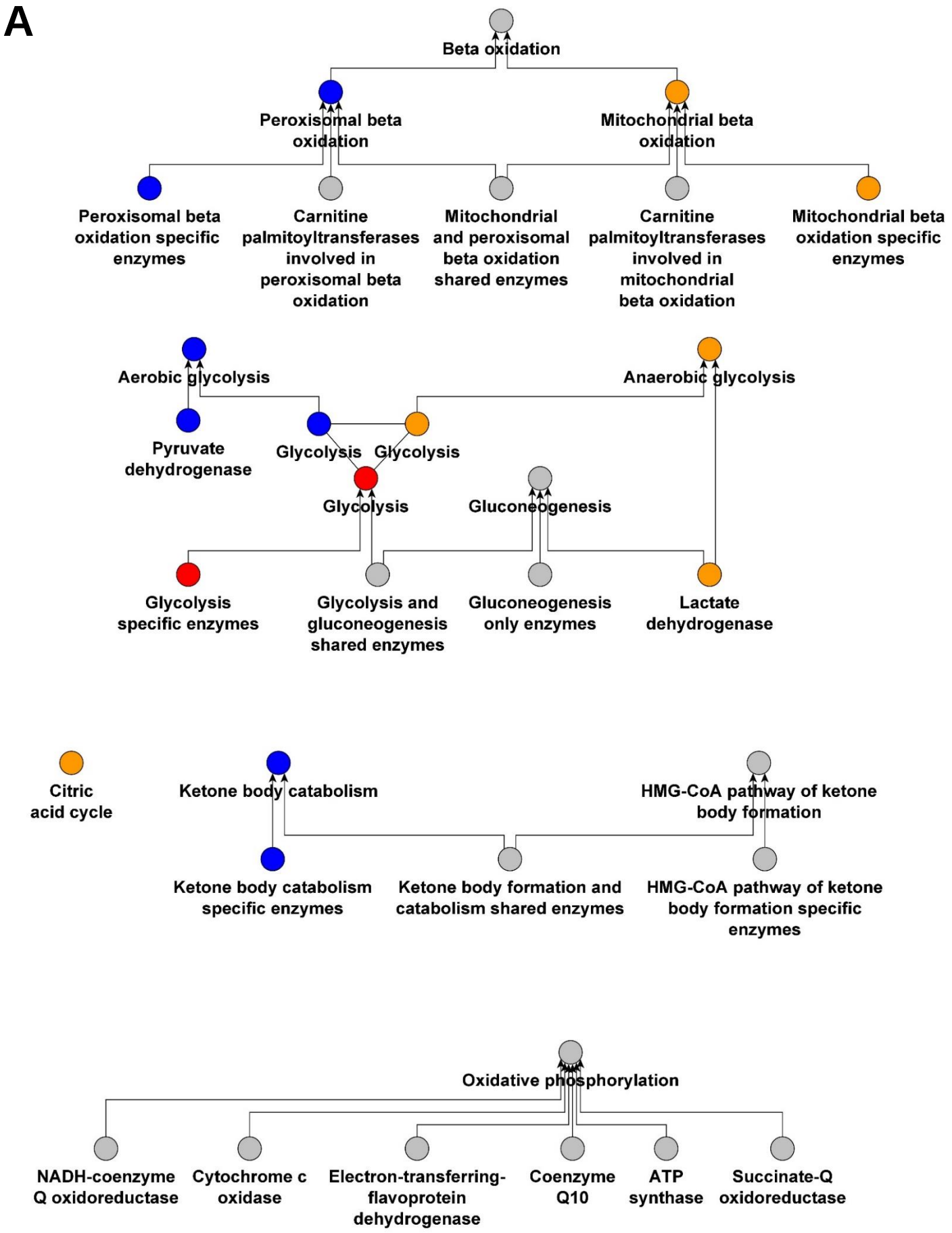

Supplemental Figure S18

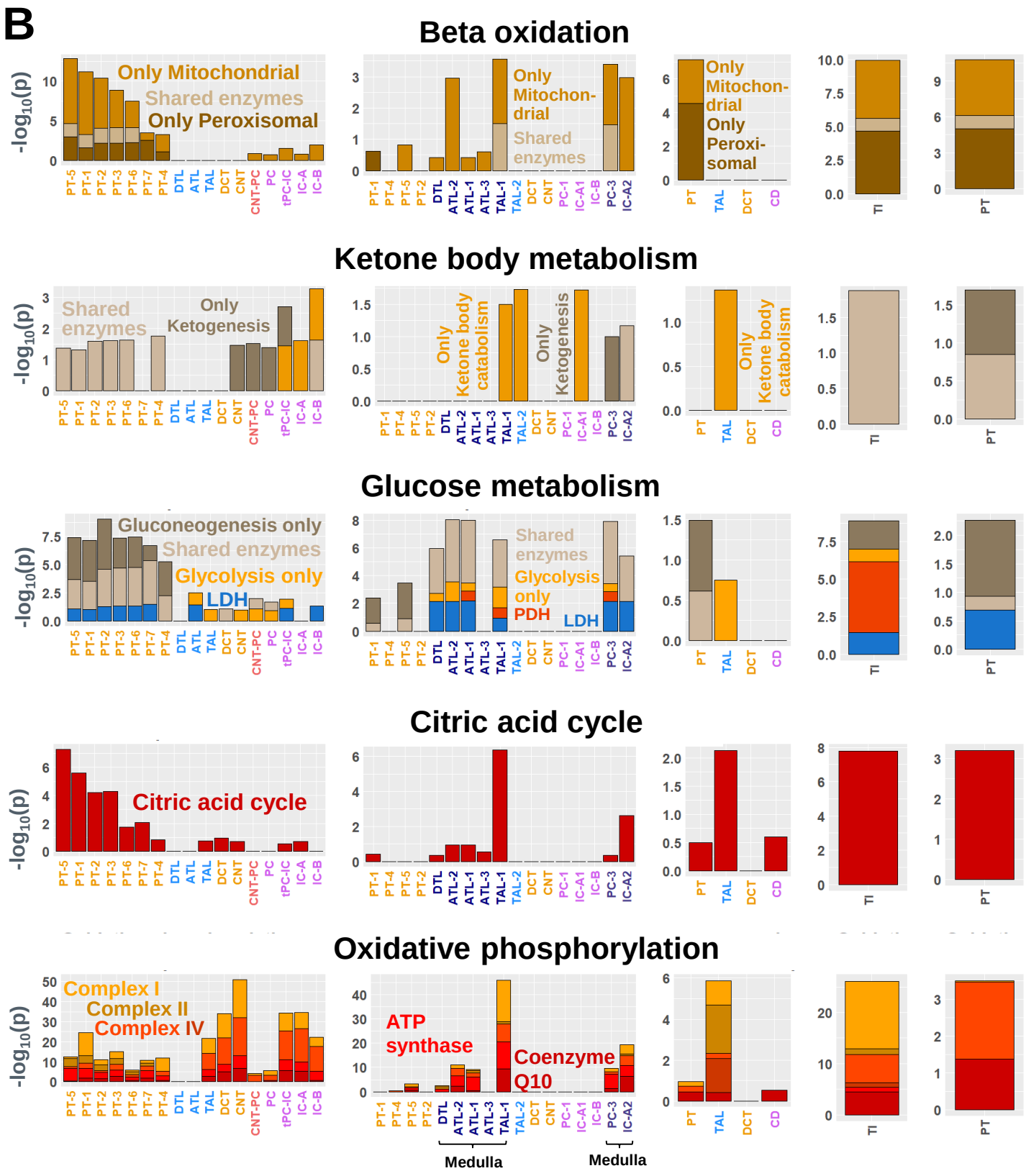
B
Beta oxidation
Only Mitochondrial
Shared enzymes
Only Peroxisomal
Only Mitochon-drial
Shared enzymes
Only Mitochon-drial
Only Peroxi-somal
Ketone body metabolism
Shared enzymes
Only Ketogenesis
Only Ketone body catabolism
Only Ketogenesis
Only Ketone body catabolism
Glucose metabolism
Gluconeogenesis only
Shared enzymes
Glycolysis only
LDH
Shared enzymes
Glycolysis only
PDH
LDH
Citric acid cycle
Citric acid cycle
Oxidative phosphorylation
Complex I
Complex II
Complex IV
ATP synthase
Coenzyme Q10
-log10(p)
PT-5 PT-1 PT-2 PT-3 PT-6 PT-7 PT-4 DTL ATL TAL DCT CNT CNT-PC PC tPC-IC IC-A IC-B
PT-1 PT-4 PT-5 PT-2 DTL ATL-2 ATL-1 ATL-3 TAL-1 TAL-2 DCT CNT PC-1 IC-A1 IC-B PC-3 IC-A2
PT TAL DCT CD
TI
PT
Medulla
Medulla
Sc RNAseq
Sn RNAseq
LMD RNAseq
LMD Proteomics
NSC Proteomics
Supplemental Figure S18

Supplemental Figure S18: Prediction of cellular dependencies on aerobic and anaerobic metabolic pathway activities. (A) We designed a small ontology that allows distinguishing between aerobic and anaerobic as well as catabolic and anabolic reactions. Shown is the annotated pathway hierarchy. Colored pathways indicate parent and child pathway pairs, where the child contains only enzymes that are specifically involved in the function of its parent and of any other parent. Pathways were populated with genes by literature curation. Parents are populated with all genes of the child pathways. **(B)** Top 500 cell type, cell subtype and subsegment specific marker genes and proteins were subjected to enrichment analysis using the leaf pathways shown in A. Initial enrichment results determined with pathways were used for the analysis shown in figure 6. For each cell type, subtype and subsegment we only considered a higher level pathway, if the child pathway that contains the enzymes specifically involved in the higher level pathway activity was also predicted (as indicated by the colored pathway pairs in A). Cell types that contain many cells obtained from medullary samples are marked. See figure 2A for cell type abbreviations.

A

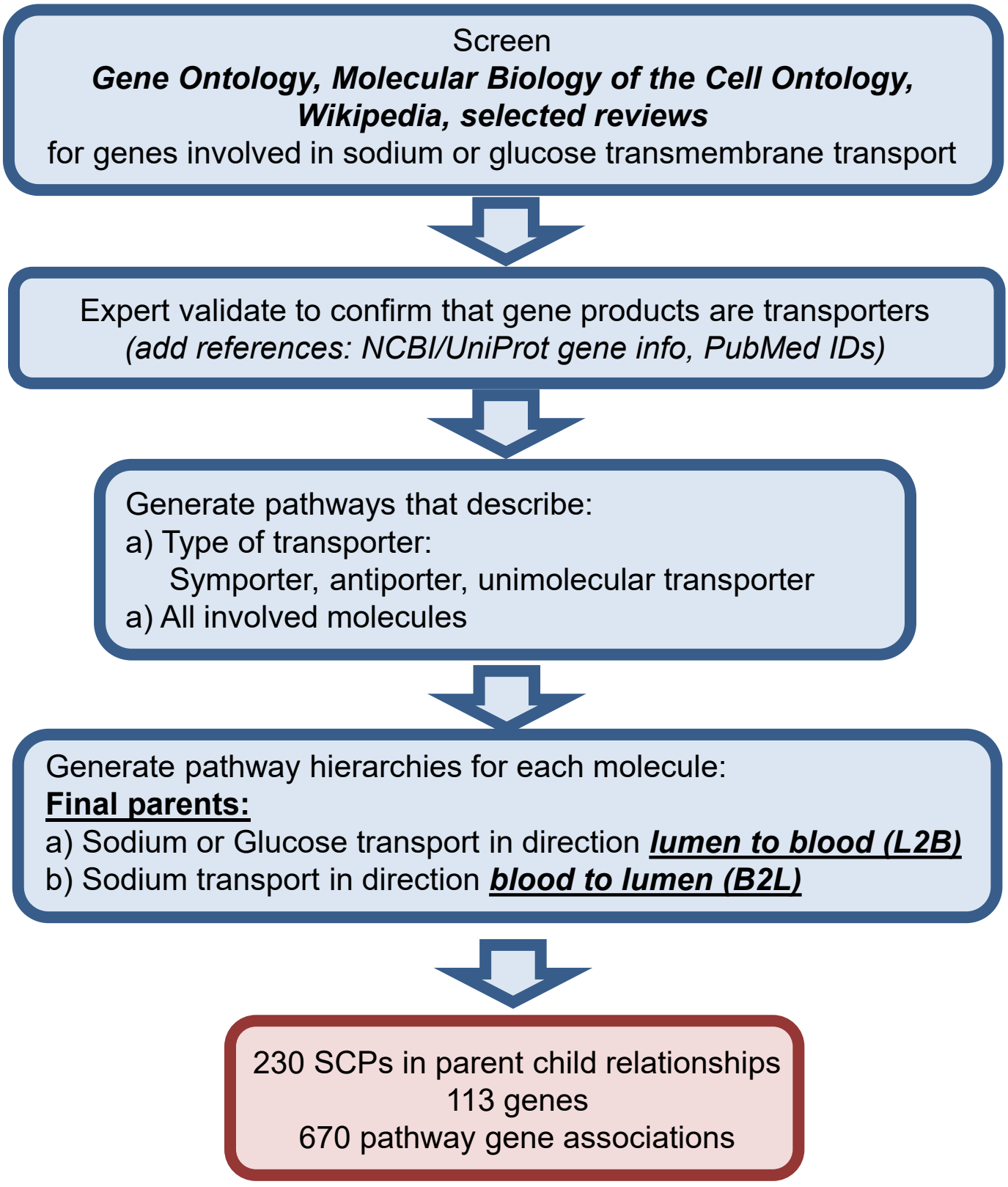

Supplemental Figure S19

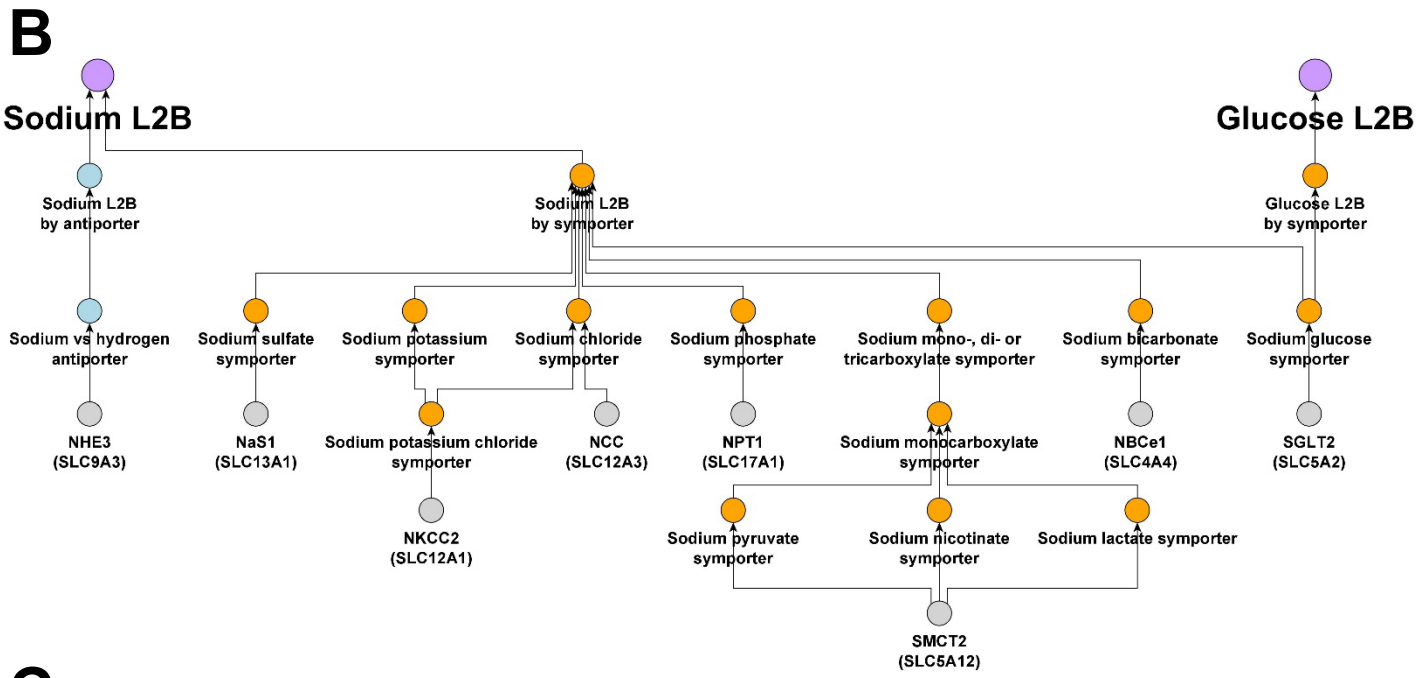

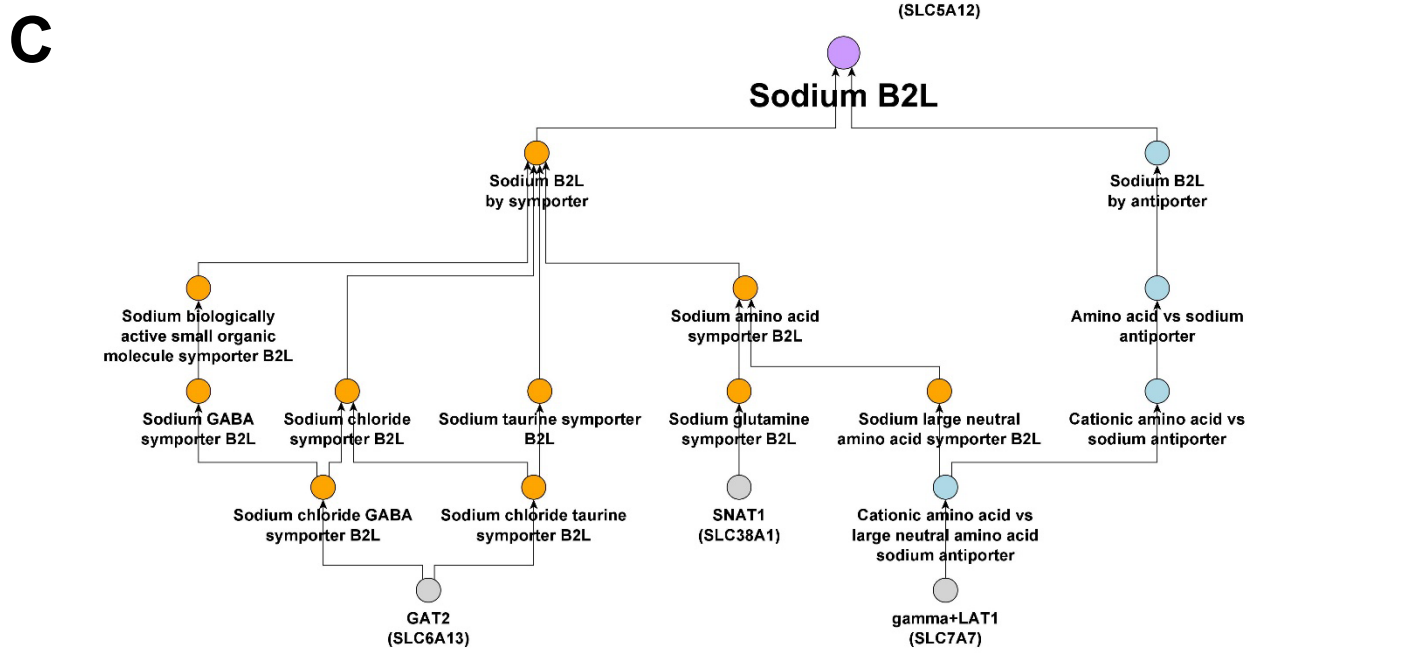

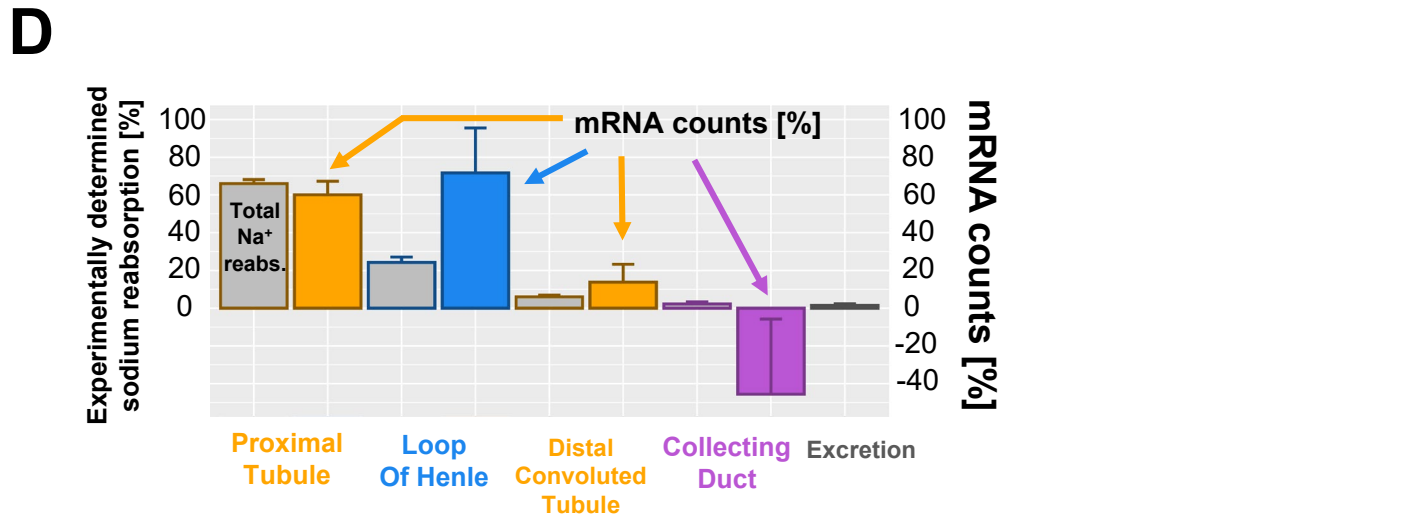

Supplemental Figure S19

E

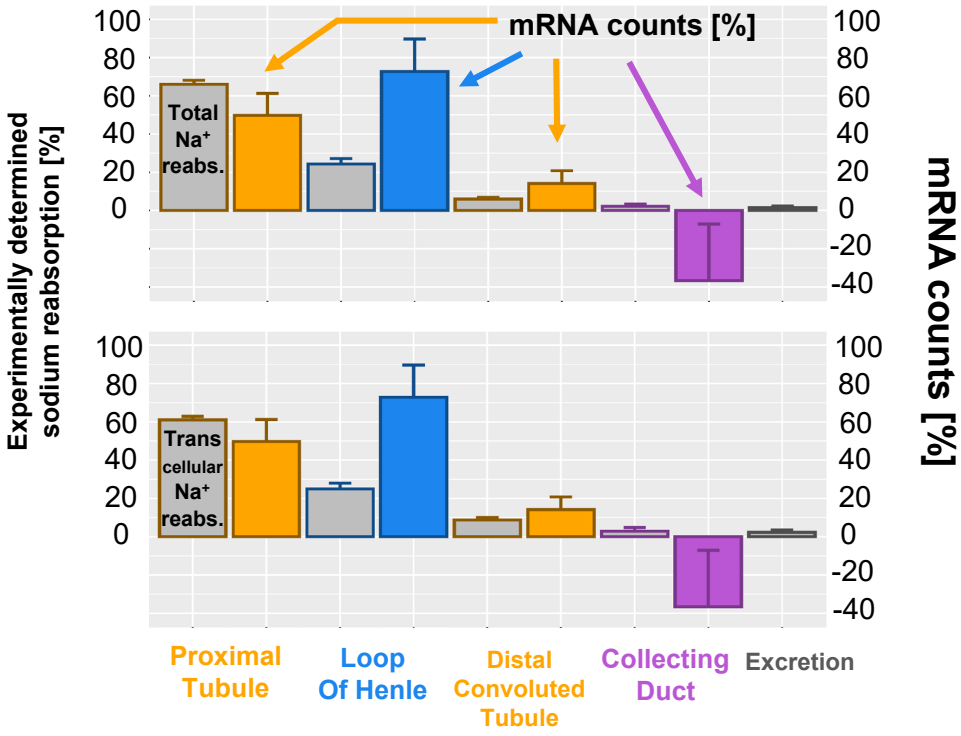

F

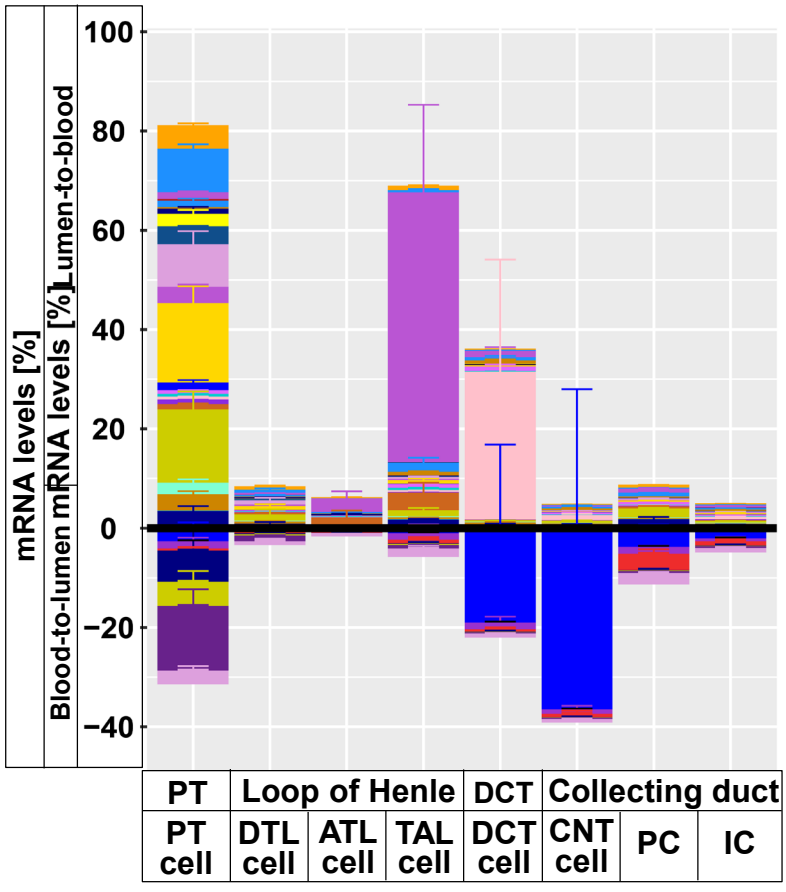

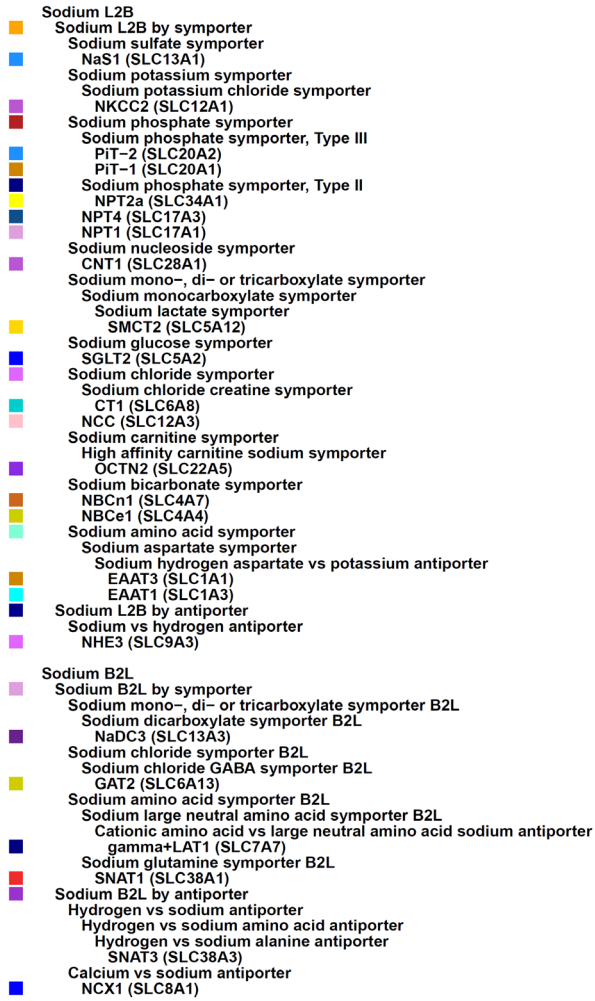

Supplemental Figure S19

G

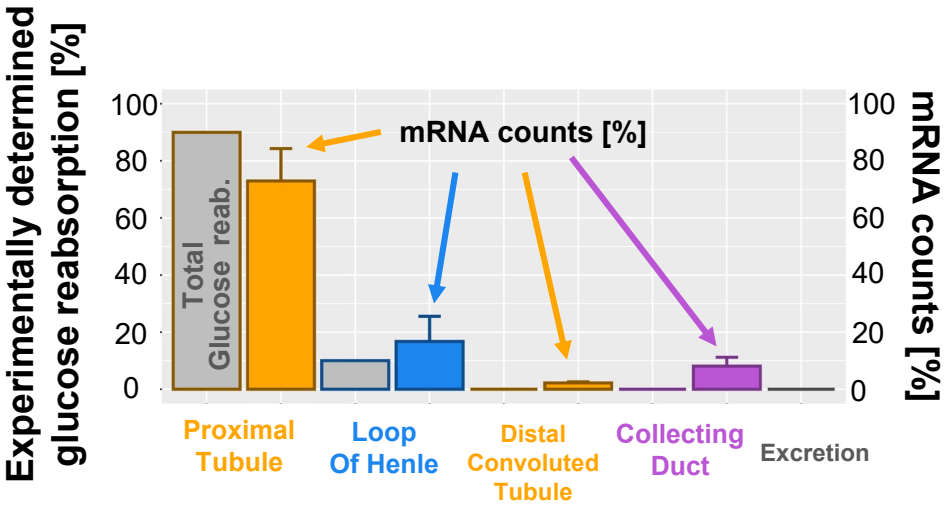

H

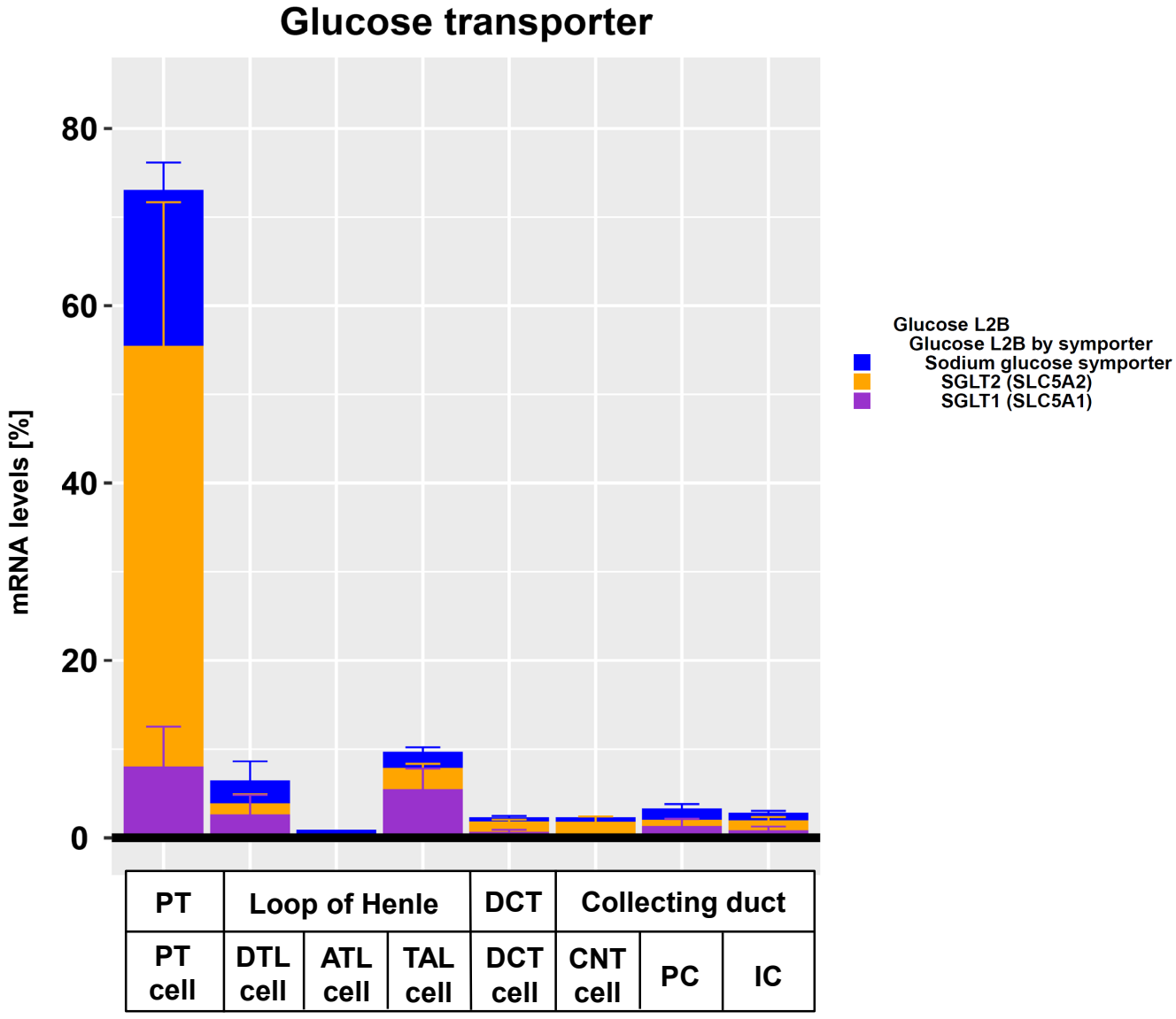

Supplemental Figure S19

I

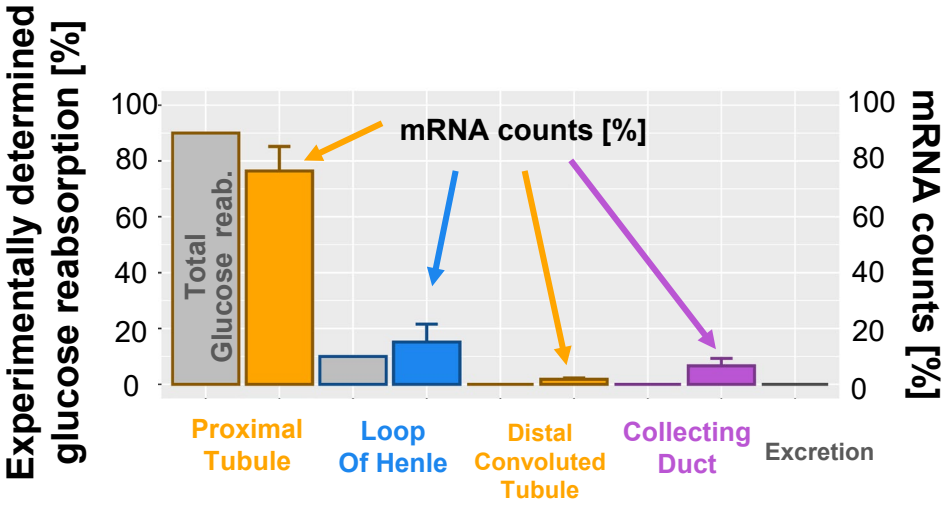

J

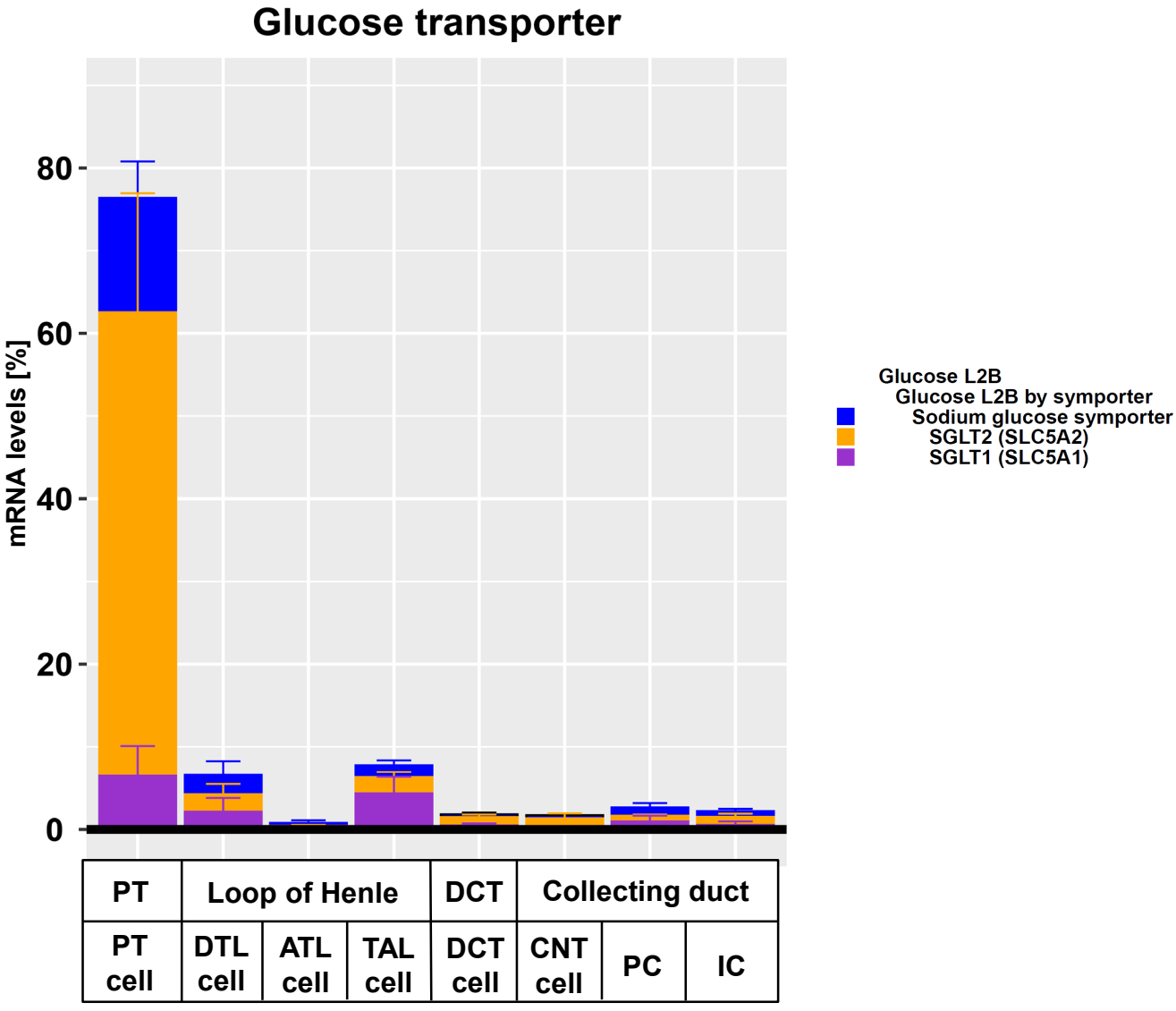

Supplemental Figure S19

Supplemental figure S19: Prediction of transmembrane ion and molecule movements. (A) Flow chart documenting the steps involved in the generation of the ontology for transmembrane sodium and glucose transport. Shown are example transporters (gray) involved in **(B)** sodium and glucose lumen-to-blood (L2B) and **(C)** sodium blood to lumen (B2L) transport and how they integrate into the hierarchy to finally converge on sodium and glucose L2B and B2L transport. Symporter mechanisms are colored in orange, antiporter mechanisms in blue. **(D)** Net reabsorption capacities for sodium (colored bars) were determined as describe in figure legend 7 and compared to experimentally determined total sodium reabsorption. **(E)** Comparison between experimentally measured total and transcellular sodium reabsorption profiles and reabsorption capacities that were predicted from the three sn RNAseq datasets used in figure 7 and the KPMP sc RNAseq dataset. See figure 7 for details. **(F)** Sodium reabsorption mechanisms were predicted based on all four datasets (three single nucleus and one single cell RNAseq datasets). See figure 2A for cell type abbreviations. **(G)** Reabsorption capacities for glucose transmembrane transport were calculated using the three sn RNAseq datasets as described in figure 7 and compared to experimentally determined glucose reabsorption profiles. Since only one physiology textbook documented the glucose reabsorption profiles, there is no standard error for the experimental values. Facilitated glucose transporters were excluded. **(H)** As for sodium, we analyzed the transport mechanisms involved in glucose reabsorption. **(I)** We compared the reabsorption capacities that were calculated using the three sn and the sc RNAseq datasets with the experimental reabsorption profiles, **(J)** followed by visualization of the individual transport mechanisms for glucose.

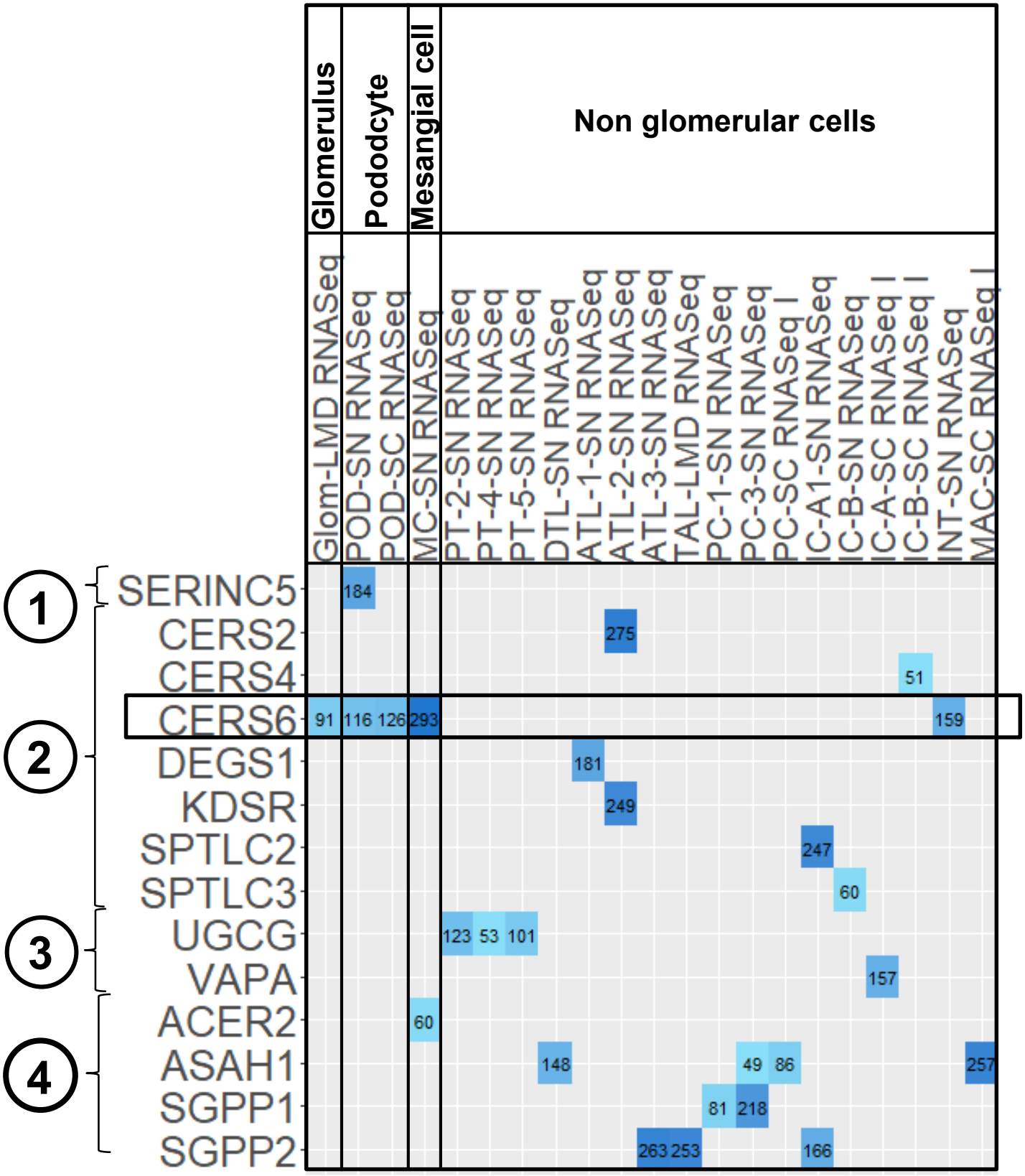

1) Serine incorporation into ER
2) Ceramide synthesis
3) (Stimulation of) Ceramide transport to SM-synthesis sites at Golgi
4) Sphingosin metabolism

Supplemental Figure S20

Supplemental Figure S20: Expression of genes involved in sphingomyelin synthesis and sphingosine metabolism in all kidney cell types and segments. Expression of curated enzymes was detected in the indicated cell types/segments. Genes were ranked by significance and ranks were added to the figure.

SUPPLEMENTARY TABLE CAPTIONS

Supplemental Table S1. Samples used for different analytical pipelines.

Supplemental Table S2. Laser microdissected (LMD) RNAseq gene expression

Supplemental Table S3. Laser microdissected (LMD) Proteomics protein expression

Supplemental Table S4. Near Single Cell (NSC) Proteomics protein expression

Supplemental Table S5. Top 2,000 marker genes and proteins predicted by each assay for each analyzed cell subtype, cell type and tissue subsegment. Marker genes and proteins are differentially expressed genes (DEGs) and proteins (DEPs) that were obtained by comparing each cell type, cell subtype or subsegment to all other cell subtypes, types or subsegments. Initially, we duplicated all subsegmental datasets and added them to each data integration term that describes a cell type localized in that particular segment. For cell type specific assignments of the subsegmental data see results section, Figure 5C and Supplementary Figure 8.

Supplemental Table S6. # of significant marker genes that were subjected to dynamic enrichment analysis.

Supplemental Table S7. Dynamic enrichment analysis results of the top 300 marker genes and proteins. We duplicated all predictions based on the subsegment specific LMD RNAseq and Proteomics and the NSC Proteomics and added them to each integration term that describes a cell type localized in that particular segment. From these results we assigned cell type specificity to the predicted pathways as described in the results sections and documented in Figure 5C and Supplementary Figure 8. Notify that the columns “Experimental_symbols_count” and “Scp_symbols_count” contain the experimental and scp genes after removal of all those genes that are not part of the background list of genes (See methods for details). Hence, they can be smaller than the gene counts documented in supplementary table 6.

Supplemental Table S8. Spatial metabolomics metabolite correlations for subjects 18-139 (A), 18-142 (B) and 18-342 (C).

Supplemental Table S9. Gene Ontology enrichments for modules in the kidney-specific functional network of top DEGs and DEPs in PT, podocytes, and principal cells.

Supplemental Table S10. Literature curated cell-type specific essential genes used for cell type identification.

Supplemental Table S11. Enrichment analysis of the top 500 significant marker genes and proteins using the generated metabolic ontology.

Supplemental Table S12. Sodium transporters identified in the sc and sn RNAseq datasets and their function in kidney sodium reabsorption.

Supplemental Table S13. Overview of cell type specific marker genes.

SUPPLEMENTAL INFORMATION

Cells of the kidney

Proximal tubular cells

Merged proximal tubule SCP networks predict a high level of metabolic activity dependent on β-oxidation of lipids, ammonium metabolism as well as absorption of ions, ion-dependent glucose reabsorption and detoxification mechanisms (Fig. 4A). These SCPs, as shown by the different colors, are inferred from multiple technologies. The size of the SCP circle reflects the number of technology types that support the prediction of the SCP, while pie slices represent the individual technologies. In some physiology functions, cases of multiple pie slices are shown for the same technology indicating that this technology predicts the same SCP for multiple subtypes of the PT cells. The solid lines indicate connections between SCPs predicted by MBCO relationships and the dashed lines indicate additional well-known relationships between SCPs. Typically, these edges can represent functional relationships such as enzyme-substrate relationships or cotransport of molecules by symporters. It should be noted that most SCPs consist of multiple gene/gene products/metabolites of which only some are experimentally determined. Both the LMD proteomics and spatial metabolomics assays only distinguish between glomerular and tubulointerstitial regions in the kidney. SCPs that were predicted by these two assays either overlapped with or described similar functions as the SCPs that were identified by the proximal tubule cell or segment-specific datasets (fig. S7). This agrees with the observation that most tubulointerstitial cells were proximal tubule cells (fig. S4A/B). Consequently, we added all SCPs identified by LMD proteomics and spatial metabolomics to the proximal tubule network as well. The identified predictions are in agreement with the well-established physiological functions of PT cells that include ATP-dependent reabsorption of ions, glucose and other small molecules like amino acids and mono- and dicarboxylates (e.g., lactate or oxalate) (*69*). The pathways also highlight the important role of PT cells in ammonium excretion, drug clearance (*70*) and iron homeostasis pathways (*71*). The latter - among other functions - mitigate kidney damage during AKI (*72*). The prediction of glucose, fructose and glutamine metabolism from integration of transcriptomic, proteomic and metabolomics assays is in agreement with the high levels of PT gluconeogenesis activity (*73, 74*). Beta-oxidation, which is the central pathway for energy generation in the PT cells (*75, 76*), is predicted by four out of six technologies. The identified genes and proteins document involvement of both mitochondrial and peroxisomal beta- oxidation (table S7). These findings support the notion that peroxisomes could be a target in kidney injury.

Both proteomic datasets of the PT subsegments highlight mitochondrial carnitine shuttle pathway that describes a central transport mechanism involved in both peroxisomal (*77*) and mitochondrial (*78*) beta-oxidation. We identify by spatial metabolomics the central carrier molecule carnitine, as well as acetyl-carnitine and palmitoyl-carnitine that are involved in transport processes during peroxisomal and mitochondrial beta-oxidation, respectively. The identification of carnitine biosynthesis and the carnitine precursor 3-Dehydroxycarnitine predicts that adult kidney - besides apical reabsorption of carnitine - also has the biosynthetic capacity for local carnitine production. Loss of beta-oxidation and consequently ATP synthesis is a significant contributor to tubulointerstitial fibrosis (*79*). Hence mapping of the variations in these pathways in different patient populations can provide a basis for molecular stratification of kidney fibrosis. Our data indicate the importance of beta-oxidation for proximal tubule function, since the prediction of local carnitine synthesis suggests an alternative carnitine source to dietary carnitine intake that might gain importance under a strictly vegetarian diet (*80*)**.** Prediction of high levels of ATP generation and turnover rate is supported by the spatial metabolites that enrich for

a pathway involved in the biosynthesis and degradation of adenine nucleotides. The ability of proximal tubule cells to significantly contribute to gluconeogenesis, especially in states of starvation is documented by the identification of many enzymes involved in gluconeogenesis in our datasets. Glycolysis-specific enzymes were not detected, as described by others and in agreement with the low potential for glycolysis in the proximal tubule (*74*). Only a few pathways describing general cell biological functions (such as ECM dynamics, cell adhesion and translation) were predicted by one technology (fig. S8).

Consequently, our analyses show that the different technologies describe the same biology, even though they might detect different genes or proteins and analyzed samples from the overlapping and non-overlapping participants (table S1).

Community clustering of PT marker genes in a kidney-specific functional network (Fig. 4B) identifies four modules enriched for functions including translation (M2), cellular response to metal ion (M4), mitochondrial organization (M1), brush border assembly (M3), and anion transport (M3). The marker genes were identified across five distinct technologies (sc/sn/LMD transcriptomics, and two independent proteomics datasets), and include genes with a corrected p-value of less than 0.01 in each technology. Genes are shaded per number of technologies identifying each marker. Five genes (*ALDH2*, *ANPEP*, *LRP2*, *PDZK1*, and *SHMT1*) were identified as PT markers across all five technologies. Fifty-four genes were identified as PT markers by four of the five technologies, and 106 genes were identified as PT markers by three of the five technologies. Functional enrichments in module clustering provide a picture consistent with the SCP enrichments: key processes enriched in network modules and also identified in SCP enrichments include fatty acid beta-oxidation (M1, M4), ammonium ion metabolic process (M3), glucose metabolic process (M3), detoxification (M1), anion transport (M3), and cellular response to metal ion (M4). While we did not separate between male and female samples in this study, sex specific differences in proximal tubule cells have been described recently (*5*).

Glomerular cells

In agreement with a previous study focusing on human and mouse glomerular cells (*4*) we detected all four different glomerular cell types, podocytes, mesangial cells, endothelial cells and parietal epithelial cells. The sc and sn transcriptomic datasets (Fig. 2) lead to four glomerular cell type specific SCP-networks. We separately analyzed the LMD transcriptomic and LMD and NSC proteomics and spatial metabolomics datasets (that were obtained from the whole glomerulus thus lacking cell type specificity) and identified glomerular SCP networks (fig. S9A). Analyzing the overlap between the glomerular SCP networks with each of the three cell-type specific SCP-networks allows us to assign glomerular SCPs to podocytes, mesangial cells or glomerular endothelial cells (fig. S9B). Ten of the 19 glomerular SCPs are also predicted for at least one glomerular cell-type based on the sc/sn transcriptomic datasets. Seven other SCPs we identified map to particular cell types per functional relationships predicted from the sc/sn RNAseq datasets. These SCPs were added to each of the individual cell type specific SCP-networks. Podocyte SCPs (fig. S9C) focus on cell-cell/cell-matrix adhesion, glomerular basement membrane (GBM) and extracellular matrix (ECM) dynamics as well as actin dynamics. All these pathways are required for foot process maintenance and formation of the glomerular filtration barrier (*81*). Metabolomics data identify sphingolipid metabolism that could be involved in cell-cell adhesions as shown in other cell types (*52, 82*). LMD segmental proteomics and transcriptomics identified key pathways involved in actin dynamics as well as cell-cell and cell-matrix adhesion. Multiple technologies identify tight junction organization, focal adhesion

organization and lamellipodia organization. The glomerular slit diaphragm between mature podocytes develops from epithelial tight and adherens junctions (*53*). It contains many of these junctional protein components and was suggested to be a specialized form of either tight junctions (*26*) or adherens junctions (*27*). This explains the prediction of these two structures from our data, thought they are not morphologically observed in healthy podocytes. We show WNT signaling as a central modulator of podocyte function (*83*). The pathway "Retinol metabolism" was predicted for both sc and sn RNAseq dataset as a regulator of tight junction similar structures. In agreement, retinoic acid has a regulatory effect on tight junctions in the epidermis and plays a significant role in mitigating podocyte apoptosis and dedifferentiation during podocyte injury (*84*).

Community clustering of podocyte marker genes in a kidney-specific functional network identifies six modules (fig. S9D). Functional enrichments in these modules included glomerulus development (M4), vasculature development (M3), cell-substrate adhesion (M1), cell-cell adhesion (M1), and actin cytoskeleton organization (M1). Thirteen genes (*AHNAK*, *CLIC5*, *FERMIT2*, *GOLIM4*, *IQGAP2*, *NES*, *NPHS2*, *PDLIM5*, *PODXL*, *PTPRO*, *SLK*, *SYNPO*, and *TJP1*) were identified as podocyte markers by all five technologies surveyed. Forty-one genes were identified by four of the five technologies and 108 genes were identified by three of the five technologies.

Our datasets identify one mesangial and one transitional mesangial/VSMC cell type from the sn and sc RNASeq assays, respectively (Fig. 2). LMD transcriptomics and proteomics and NSC proteomics along with sc and sn transcriptomics data identify SCPs involved in actin cytoskeleton dynamics, ECM dynamics, cell adhesion and amyloid plaque generation in these mesangial cells (fig. S9E). Our results are in agreement with their well-known function in blood vessel contraction and ECM support (*85*). In addition, one glomerular endothelial cell type was identified by the sc RNAseq data (Fig. 2). Its SCP-network derived from integration of LMD proteomics and transcriptomics and NSC transcriptomics along with sc transcriptomic data identify cytoskeletal, trans-endothelial immune cell migration and antigen presentation pathways (fig. S9F). The assignment of "integrin-mediated leukocyte rolling" to endothelial cells is supported by the presence of the related "leukocyte transmigration through endothelium" SCP by sc and LMD RNA transcriptomics. Sn and sc RNAseq assays identified one parietal epithelial and one parietal epithelial cell type that also shows characteristics of loop of Henle cells, respectively (Fig. 2). Parietal epithelial SCP networks contain pathways involved in cell-cell and cell-matrix adhesion and intermediate filament dynamics (fig. S9G).

Loop of Henle

We identified one descending limb cell subtype by each sc and sn RNAseq assay (Fig. 2A). SCP networks from sc and sn RNAseq data for the descending limb cells identify cell adhesion functions and cytoskeleton dynamics (fig. S10A). The presence of "tight junction organization" is in agreement with barrier formation in the descending limb that can allow for paracellular water reabsorption (*86*) but not for reabsorption of ions such as sodium or chloride (87). Community clustering of descending limb marker genes in a kidney-specific functional network identifies six modules enriched in functions including cell-cell adhesion (M6), epithelium development (M3), tube development (M3), response to endoplasmic reticulum stress (M5), and water homeostasis (M6) (fig. S10B).

Three thin ascending limb (ATL) cell subtypes are identified by sn RNAseq although only one type was identified by sc RNAseq (fig. 2A). SCP-networks obtained for ATL cells from these two technologies describe functions such as cell adhesion, cytoskeleton dynamics and translation (fig. S10C). Overall, these SCP networks agree with the known functions of these cells that initiate the formation of dilute urine by the establishment of a water impermeable barrier that is permeable to low levels of ions (*88*)**.** Community clustering of ATL marker genes in a kidney-specific functional network identifies seven modules enriched in functions including translation (M1), kidney morphogenesis (M6), and cell-cell adhesion (M4) (fig. S10D).

Sc and sn transcriptomics identified one and two thick ascending limb (TAL) cell subtypes, respectively (Fig. 2A). TAL cell SCPs indicate sodium, potassium and chloride transport capabilities as detected by sc, sn and LMD transcriptomic technologies (fig. S10E). Tubulointerstitial SCPs identified by the LMD Proteomics and Spatial Metabolomics assays provide evidence for functional capabilities of the SCPs networks (fig. S7). These findings are in agreement with the known transcellular reabsorption of sodium and chloride that is initiated by the furosemide sensitive sodium chloride potassium symporter NKCC2 and supported by apical potassium recycling (*36*). The “tight junction organization” SCP is involved in the establishment of a physical barrier that makes this region impermeable to water and thus allows the dilution of urine (*32*). Among the tight junction associated genes are *CLDN10* and *CLDN16* that are involved in the paracellular reabsorption of sodium or calcium/magnesium (*36, 40*), respectively, which supports the well-known physiology of this nephron segment. Involvement of “retinol metabolism” suggests that retinol regulated transcription can play an important role in TAL tight junction maintenance, similarly to its contribution to podocyte integrity. SCPs involved in the late secretory and early endocytic pathway support the known morphologic observation of vesicles below the plasma membrane that contain the furosemide sensitive NKCC2 (*36, 89*) allowing its mobilization and retrieval on demand (*37*).

The high energy demand of the TAL cells is reflected by the identification of SCPs involved in mitochondrial energy generation from LMD transcriptomics and proteomics. Spatial metabolomics that identify purine metabolites in the tubulointerstitium also support this conclusion. Community clustering of TAL marker genes in a kidney-specific functional network (fig. S10F) identifies six modules enriched in functions including regulation of ion transport (M6), calcium ion import (M6), sodium ion transport (M6), translation (M1), and mitochondrion organization (M2).

Distal convoluted tubules

One distal convoluted (DCT) cell subtype was identified based on each of sc and sn RNAseq assays (Fig. 2A). Predicted SCPs for the DCT cells from sc, sn and LMD transcriptomics converge on sodium and chloride transmembrane transport (fig. S11A). Our results agree with the well-known sodium and chloride reabsorption by this cell type via the thiazide sensitive sodium chloride symporter NCC (*90*). Additionally, sc/sn transcriptomics highlight reabsorption of calcium, potassium, bicarbonate and phosphate. Community clustering of DCT marker genes in a kidney-specific functional network (fig. S11B) identifies three modules enriched in functions including regulation of ion transport (M3) and metal ion homeostasis (M2). A recent study focusing on the cells in the distal nephron purified by FACS-enrichment of mouse kidney cells further classifies the DCT cells into multiple subtypes (*2*).

Connecting tubules

Each sn and sc assay identified one connecting tubule (CNT) subtype (Fig. 2A). Both sn and sc transcriptomic datasets for CNT cells indicate that SCPs for sodium, potassium and calcium transmembrane transport activities are enriched (fig. S12A), supporting its function in fine tuning electrolyte balances (*91*). Other SCPs indicate signaling, endoplasmic reticulum and energy functions in this cell type. Community clustering of CNT marker genes in a kidney-specific functional network (fig. S12B) identifies three modules enriched in functions including ion transport (M2), receptor-mediated endocytosis (M3), and mitochondrion organization (M1).

Collecting duct

Sc and sn RNAseq show two and three principal cell subtypes, respectively (Fig. 2A). The principal cell SCP networks were obtained by merging the principal cell specific SCPs predicted from sc and sn transcriptomics with the collecting duct (CD) specific SCPs predicted from LMD transcriptomics (fig. S12C). Overlapping or functionally related SCPs identified by LMD Proteomics and Spatial Metabolomics were added as well (fig. S7). Both sc and sn technologies identified “Potassium-“ as well as “Sodium-transmembrane transport” SCPs for the principal cells. The SCP “Water transmembrane transport” was identified by both sn and sc RNAseq assays as well, though with a lower rank for sn RNASeq assays that did not pass our applied cutoff. The LMD transcriptomics and proteomics data identified the energy generation SCPs required for the various transport SCPs identified by the sc and sn transcriptomic data. The spatial metabolomics data sets provided support for energy generation pathways identified by the LMD technologies.

Principal cells play an important role in fine tuning ion and water reabsorption and thereby regulate systemic electrolyte and water balance (*91*). The anti-diuretic hormone working with prostaglandins regulates the levels of AQP2 on the apical plasma membrane (*92*) stimulating water reabsorption by the principal cell. Apically reabsorbed water is exported by basal water transporters AQP3 and AQP4. We detect both *AQP2* and *AQP3* in our datasets. Sodium reabsorption is regulated by the amiloride-sensitive sodium channel EnaC whose expression and protein turnover is regulated by aldosterone (*93*). The aldosterone-stimulated reabsorption of sodium is coupled with secretion of potassium , as highlighted by our data. Additionally, we show calcium transmembrane transport for one cell subtype by both sn and sc RNAseq assays. Both sc and sn technologies identify SCPs involved in drug and toxin transmembrane movement in one of the subtypes of the principal cell, although drug excretion is generally described to occur in the proximal tubule (*70*). Furthermore, community clustering of PC marker genes in a kidney-specific functional network (fig. S12D) identifies seven modules enriched in functions including ion transport and homeostasis (M7), regulation of vesicle-mediated transport (M4), and water homeostasis (M6).

We identified multiple subclusters of intercalated cells that could be assigned to IC-A, IC-B and one transitionary subtype, tPC-IC, as well as IC-A1, IC-A2 and IC-B in the sc and sn transcriptomic datasets, respectively (Fig. 2A). SCPs networks were identified by merging sc and sn transcriptomic data with LMD transcriptomic data obtained from the collecting duct (fig. S12E). Additionally we added overlapping or functionally related SCPs predicted by LMD Proteomics and Spatial Metabolomics (fig. S7). We find the SCP “Bicarbonate transmembrane transport” in all three sc subtypes and one sn subtype (fig. S12E), documenting the importance of the intercalated cells in the regulation of systemic acid-base homeostasis (*94*). Apical and basolateral bicarbonate transport is driven by exchange for chloride (*94*), as indicated by the

“Chloride transmembrane transport” SCP identified for one subtype in both sn and sc RNAseq datasets. Community clustering of IC marker genes in a kidney-specific functional network (fig. S12F) identifies six modules enriched in functions including regulation of body fluid levels (M3), translation (M1), mitochondrion organization (M2), bicarbonate transport (M5), and cell-cell adhesion (M4). Enrichment analysis using Gene Ontology predicts phagocytic activity (phagosome maturation and acidification) based on subunits of the vacuolar H^+ATPase (*94*) (fig. S12G). In combination with the prediction of SCP involved in actin cytoskeleton our data supports the recent observation of phagocytic activity of the intercalated cells (*95*).

Interstitium and the vasculature

Endothelial Cells: We find four types of endothelial cells by sn transcriptomics and two by sc transcriptomics, in addition to glomerular endothelial cell identified sc transcriptomics (Fig. 2A). SCP networks for endothelial cells identified from sc and sn transcriptomic data sets contain pathways involved in cellular adhesion, trans-endothelial migration, actin cytoskeleton dynamics, caveolin-mediated endocytosis, signaling and antigen presentation (fig. S13A).

Vascular smooth muscle cells: We identified a single type of VSMC by sn RNAseq assay (Fig. 2A). The sc transcriptomic technology identified a variant of mesangial cells that has VSMC markers. We classified this subtype as a glomerular cell subtype. SCP networks from sn technology highlight cell contraction capabilities for the VSMC (fig. S13B).

Fibroblasts: We identified a single type of fibroblast from sc and sn RNAseq assays (Fig. 2). SCPs in fibroblasts identified from sc, sn and LMD transcriptomics data describe pathways related to ECM dynamics, cell adhesion, cytoskeleton dynamics and the complement pathways (fig. S14). The proteomic assays did not detect ECM components related SCPS among the highly ranked pathways.

Immune cells: Four types of immune cells are detected by sc or sn RNAseq technologies. These include natural killer cells, three types of T-cells, B-Cells and three types of macrophages and monocytes (Fig. 2A). SCP-networks for macrophages contains pathways involved in antigen presentation, actin cytoskeleton dynamics and translation (fig. S15A). Connection of the SCPs involved in actin cytoskeleton dynamics to the SCP ‘Macrophage migration inhibitory factor (MIF) signaling pathway indicates the potential for chemotactic activity. Macrophage migration is driven by rearrangements in the actin cytoskeleton that are activated by stimulation of the MIF receptor proteins CD74 and CXCR4 (*96, 97*) as identified in our data.

The SCP ‘Cellular iron uptake and export’ documents the central role of macrophages in iron homeostasis . It is predicted based on SLC39A8, a transmembrane transporter involved in transport of multiple divalent metal ions including iron (*98*) and the scavenger receptor CD163 that is also involved in removing hemoglobin or haptoglobin-hemoglobin complexes by splenic red pulp macrophages and Kupffer cells (*99*). This SCP and the SCPs involved in actin dynamics are also identified by LMD transcriptomics of the interstitium. SCPs in the natural killer cells identify antigen presentation, cell migration and actin cytoskeleton dynamics (fig. S15B). Similarly, SCP-networks predicted for B-cells and T-cells contain pathways involved in antigen presentation and the immunoproteasome and translation (fig. S15C and S15D, respectively). A detailed study of immune cell zonation of the human kidney has been published (*8*), while another single cell sequencing study characterized twelve myeloid cell subtypes associated with progression and regression of kidney disease in an animal injury model (*3*).

Since immune activity was documented for all cell types along the nephron (*8*), we analyzed the fraction of cell type and subtype specific marker genes and proteins that were annotated to immune pathways in Gene Ontology. In agreement with the indicated study, about 5-15% of all marker genes participate in immune cell functions (fig. S16). We want to emphasize that in the immune zonation study (14) the highest immune activity was predicted for epithelial cells of the pelvis, while our samples do not contain tissue from the pelvis.

REFERENCES AND NOTES

1. J. Park, C. L. Liu, J. Kim, K. Susztak, Understanding the kidney one cell at a time. *Kidney Int.* **96**, 862–870 (2019).

2. L. Chen, C. L. Chou, M. A. Knepper, Targeted single-cell RNA-seq identifies minority cell types of kidney distal nephron. *J. Am. Soc. Nephrol.* **32**, 886–896 (2021).

3. B. R. Conway, E. D. O'Sullivan, C. Cairns, J. O'Sullivan, D. J. Simpson, A. Salzano, K. Connor, P. Ding, D. Humphries, K. Stewart, O. Teenan, R. Pius, N. C. Henderson, C. Bénézech, P. Ramachandran, D. Ferenbach, J. Hughes, T. Chandra, L. Denby, Kidney single-cell atlas reveals myeloid heterogeneity in progression and regression of kidney disease. *J. Am. Soc. Nephrol.* **31**, 2833–2854 (2020).

4. B. He, P. Chen, S. Zambrano, D. Dabaghie, Y. Hu, K. Möller-Hackbarth, D. Unnersjö-Jess, G. G. Korkut, E. Charrin, M. Jeansson, M. Bintanel-Morcillo, A. Witasp, L. Wennberg, A. Wernerson, B. Schermer, T. Benzing, P. Ernfors, C. Betsholtz, M. Lal, R. Sandberg, J. Patrakka, Single-cell RNA sequencing reveals the mesangial identity and species diversity of glomerular cell transcriptomes. *Nat. Commun.* **12**, 2141 (2021).

5. L. Huang, J. Liao, J. He, S. Pan, H. Zhang, X. Yang, J. Cheng, Y. Chen, Z. Mo, Single-cell profiling reveals sex diversity in human renal PTs. *Gene* **752**, 144790 (2020).

6. C. Kuppe, M. M. Ibrahim, J. Kranz, X. Zhang, S. Ziegler, J. Perales-Patón, J. Jansen, K. C. Reimer, J. R. Smith, R. Dobie, J. R. Wilson-Kanamori, M. Halder, Y. Xu, N. Kabgani, N. Kaesler, M. Klaus, L. Gernhold, V. G. Puelles, T. B. Huber, P. Boor, S. Menzel, R. M. Hoogenboezem, E. M. J. Bindels, J. Steffens, J. Floege, R. K. Schneider, J. Saez-Rodriguez, N. C. Henderson, R. Kramann, Decoding myofibroblast origins in human kidney fibrosis. *Nature* **589**, 281–286 (2021).

7. J. Park, R. Shrestha, C. Qiu, A. Kondo, S. Huang, M. Werth, M. Li, J. Barasch, K. Suszták, Single-cell transcriptomics of the mouse kidney reveals potential cellular targets of kidney disease. *Science* **360**, 758–763 (2018).

8. B. J. Stewart, J. R. Ferdinand, M. D. Young, T. J. Mitchell, K. W. Loudon, A. M. Riding, N. Richoz, G. L. Frazer, J. U. L. Staniforth, F. A. Vieira Braga, R. A. Botting, D.M. Popescu, R. Vento-Tormo, E. Stephenson, A. Cagan, S. J. Farndon, K. Polanski, M. Efremova, K. Green, M. del Castillo Velasco-Herrera, C. Guzzo, G. Collord, L. Mamanova, T. Aho, J. N. Armitage, A. C. P. Riddick, I. Mushtaq, S. Farrell, D. Rampling, J. Nicholson, A. Filby, J. Burge, S. Lisgo, S. Lindsay, M. Bajenoff, A. Y. Warren, G. D. Stewart, N. Sebire, N. Coleman, M. Haniffa, S. A. Teichmann, S. Behjati, M. R. Clatworthy, Spatiotemporal immune zonation of the human kidney. *Science* **365**, 1461–1466 (2019).

9. P. C. Wilson, H. Wu, Y. Kirita, K. Uchimura, N. Ledru, H. G. Rennke, P. A. Welling, S. S. Waikar, B. D. Humphreys, The single-cell transcriptomic landscape of early human diabetic nephropathy. *Proc. Natl. Acad. Sci. U.S.A.* **116**, 19619–19625 (2019).

10. H. Wu, Y. Kirita, E. L. Donnelly, B. D. Humphreys, Advantages of single-nucleus over single-cell RNA sequencing of adult kidney: Rare cell types and novel cell states revealed in fibrosis. *J. Am. Soc. Nephrol.* **30**, 23–32 (2019).

11. M. D. Young, T. J. Mitchell, F. A. Vieira Braga, M. G. B. Tran, B. J. Stewart, J. R. Ferdinand, G. Collord, R. A. Botting, D.M. Popescu, K. W. Loudon, R. Vento-Tormo, E. Stephenson, A. Cagan, S. J. Farndon, M. del Castillo Velasco-Herrera, C. Guzzo, N. Richoz, L. Mamanova, T. Aho, J. N. Armitage, A. C. P. Riddick, I. Mushtaq, S. Farrell, D. Rampling, J. Nicholson, A. Filby, J. Burge, S. Lisgo, P. H. Maxwell, S. Lindsay, A. Y. Warren, G. D. Stewart, N. Sebire, N. Coleman, M. Haniffa, S. A. Teichmann, M. Clatworthy, S. Behjati, Single-cell transcriptomes from human kidneys reveal the cellular identity of renal tumors. *Science* **361**, 594–599 (2018).

12. I. H. de Boer, C. E. Alpers, E. U. Azeloglu, U. G.J. Balis, J. M. Barasch, L. Barisoni, K. N. Blank, A. S. Bomback, K. Brown, P. C. Dagher, A. L. Dighe, M. T. Eadon, T. M. el-Achkar, J. P. Gaut, N. Hacohen, Y. He, J. B. Hodgin, S. Jain, J. A. Kellum, K. Kiryluk, R. Knight, Z. G. Laszik, C. Lienczewski, L. H. Mariani, R. L. McClelland, S. Menez, D. G. Moledina, S. D. Mooney, J. F. O'Toole, P. M. Palevsky, C. R. Parikh, E. D. Poggio, S. E. Rosas, M. R. Rosengart, M. M. Sarwal, J. A. Schaub, J. R. Sedor, K. Sharma, B. Steck, R. D. Toto, O. G. Troyanskaya, K. R. Tuttle, M. A. Vazquez, S. S. Waikar, K. Williams, F. P. Wilson, K. Zhang, R. Iyengar, M. Kretzler, J.

Himmelfarb, R. Knight, S. Lecker, I. Stillman, S. Waikar, G. Mcmahon, A. Weins, S. Short, N. Hacohen, P. Hoover, M. Aulisio, L. Cooperman, L. Herlitz, J. O'Toole, E. Poggio, J. Sedor, S. Jolly, P. Appelbaum, O. Balderes, J. Barasch, A. Bomback, P. A. Canetta, V. D. d'Agati, K. Kiryluk, S. Kudose, K. Mehl, J. Radhakrishnan, C. Weng, L. Barisoni, T. Alexandrov, T. Ashkar, D. Barwinska, P. Dagher, K. Dunn, M. Eadon, M. Ferkowicz, K. Kelly, T. Sutton, S. Winfree, S. Menez, C. Parikh, A. Rosenberg, P. Villalobos, R. Malik, D. Fine, M. Atta, J. M. Monroy Trujillo, A. Slack, S. Rosas, M. Williams, E. Azeloglu, C. (J.) He, R. Iyengar, J. Hansen, S. Parikh, B. Rovin, C. Anderton, L. Pasa-Tolic, D. Velickovic, J. Lukowski, G. (H.) Oliver, J. Ardayfio, J. Bebiak, K. Brown, T. Campbell, C. Campbell, L. Hayashi, N. Jefferson, R. Koewler, G. Roberts, J. Saul, A. Shpigel, E. C. Stutzke, L. Wright, L. Miegs, R. Pinkeney, R. Sealfon, O. Troyanskaya, K. Tuttle, D. Dobi, Y. Goltsev, B. Lake, K. Zhang, M. Joanes, Z. Laszik, A. Schroeder, M. Sarwal, T. Sigdel, U. Balis, V. Blanc, O. He, J. Hodgin, M. Kretzler, L. Mariani, R. Menon, E. Otto, J. Schaub, B. Steck, C. Lienczewski, S. Eddy, M. Elder, D. Hall, J. Kellum, M. Kruth, R. Murugan, P. Palevsky, P. Randhawa, M. Rosengart, S. Sims-Lucas, M. Stefanick, S. Stull, M. Tublin, C. Alpers, I. de Boer, A. Dighe, J. Himmelfarb, R. Mcclelland, S. Mooney, S. Shankland, K. Williams, K. Blank, J. Carson, F. Dowd, Z. Drager, C. Park, K. Sharma, G. Zhang, S. Bansal, M. Venkatachalam, A. Kermani, S. Lee, C. Lu, T. Miller, O. Moe, H. Park, K. Sambandam, F. Sanchez, J. Torrealba, T. Robert, M. Vazquez, N. Wang, J. Gaut, S. Jain, A. Vijayan, R. Luciano, D. Moledina, U. Ugochukwu, F. P. Wilson, S. Alfano, Rationale and design of the Kidney Precision Medicine Project. *Kidney Int.* **99**, 498–510 (2021).

13. T. M. El-Achkar, M. T. Eadon, R. Menon, B. B. Lake, T. K. Sigdel, T. Alexandrov, S. Parikh, G. Zhang, D. Dobi, K. W. Dunn, E. A. Otto, C. R. Anderton, J. M. Carson, J. Luo, C. Park, H. Hamidi, J. Zhou, P. Hoover, A. Schroeder, M. Joanes, E. U. Azeloglu, R. Sealfon, S. Winfree, B. Steck, Y. He, V. D'Agati, R. Iyengar, O. G. Troyanskaya, L. Barisoni, J. Gaut, K. Zhang, Z. Laszik, B. H. Rovin, P. C. Dagher, K. Sharma, M. M. Sarwal, J. B. Hodgin, C. E. Alpers, M. Kretzler, S. Jain, A multimodal and integrated approach to interrogate human kidney biopsies with rigor and reproducibility: Guidelines from the Kidney Precision Medicine Project. *Physiol. Genomics* **53**, 1–11 (2021).

14. B. B. Lake, S. Chen, M. Hoshi, N. Plongthongkum, D. Salamon, A. Knoten, A. Vijayan, R. Venkatesh, E. H. Kim, D. Gao, J. Gaut, K. Zhang, S. Jain, A single-nucleus RNA-sequencing

pipeline to decipher the molecular anatomy and pathophysiology of human kidneys. *Nat. Commun.* **10**, 2832 (2019).

15. R. Menon, E. A. Otto, P. Hoover, S. Eddy, L. Mariani, B. Godfrey, C. C. Berthier, F. Eichinger, L. Subramanian, J. Harder, W. Ju, V. Nair, M. Larkina, A.S. Naik, J. Luo, S. Jain, R. Sealfon, O. Troyanskaya, N. Hacohen, J.B. Hodgin, M. Kretzler, K.P.M.P. Kpmp; Nephrotic Syndrome Study Network (NEPTUNE)., Single cell transcriptomics identifies focal segmental glomerulosclerosis remission endothelial biomarker. *JCI Insight* **5**, e133267 (2020).

16. H. Wu, A. F. Malone, E. L. Donnelly, Y. Kirita, K. Uchimura, S. M. Ramakrishnan, J. P. Gaut, B. D. Humphreys, Single-cell transcriptomics of a human kidney allograft biopsy specimen defines a diverse inflammatory response. *J. Am. Soc. Nephrol.* **29**, 2069–2080 (2018).

17. Y. Muto, P. C. Wilson, N. Ledru, H. Wu, H. Dimke, S. S. Waikar, B. D. Humphreys, Single cell transcriptional and chromatin accessibility profiling redefine cellular heterogeneity in the adult human kidney. *Nat. Commun.* **12**, 2190 (2021).

18. L. G. Palmer, J. Schnermann, Integrated control of Na transport along the nephron. *Clin. J. Am. Soc. Nephrol.* **10**, 676–687 (2015).

19. D. Barwinska, T. M. el-Achkar, R. Melo Ferreira, F. Syed, Y.H. Cheng, S. Winfree, M. J. Ferkowicz, T. Hato, K. S. Collins, K. W. Dunn, K. J. Kelly, T. A. Sutton, B. H. Rovin, S. V. Parikh, C. L. Phillips, P. C. Dagher, M. T. Eadon; for the Kidney Precision Medicine Project, Molecular characterization of the human kidney interstitium in health and disease. *Sci. Adv.* **7**, eabd3359 (2021).

20. C. Buccitelli, M. Selbach, mRNAs, proteins and the emerging principles of gene expression control. *Nat. Rev. Genet.* **21**, 630–644 (2020).

21. R. C. Calizo, S. Bhattacharya, J. G. C. van Hasselt, C. Wei, J. S. Wong, R. J. Wiener, X. Ge, N. J. Wong, J.J. Lee, C. M. Cuttitta, G. Jayaraman, V. H. Au, W. Janssen, T. Liu, H. Li, F. Salem, E. A. Jaimes, B. Murphy, K. N. Campbell, E. U. Azeloglu, Disruption of podocyte cytoskeletal biomechanics by dasatinib leads to nephrotoxicity. *Nat. Commun.* **10**, 2061 (2019).

22. J. Hansen, D. Meretzky, S. Woldesenbet, G. Stolovitzky, R. Iyengar, A flexible ontology for inference of emergent whole cell function from relationships between subcellular processes. *Sci. Rep.* **7**, 17689 (2017).

23. J. Xia, N. Psychogios, N. Young, D. S. Wishart, MetaboAnalyst: A web server for metabolomic data analysis and interpretation. *Nucleic Acids Res.* **37**, W652–660 (2009).

24. C. S. Greene, A. Krishnan, A. K. Wong, E. Ricciotti, R. A. Zelaya, D. S. Himmelstein, R. Zhang, B. M. Hartmann, E. Zaslavsky, S. C. Sealfon, D. I. Chasman, G. A. FitzGerald, K. Dolinski, T. Grosser, O. G. Troyanskaya, Understanding multicellular function and disease with human tissue-specific networks. *Nat. Genet.* **47**, 569–576 (2015).

25. A. Krishnan, R. Zhang, V. Yao, C. L. Theesfeld, A. K. Wong, A. Tadych, N. Volfovsky, A. Packer, A. Lash, O. G. Troyanskaya, Genome-wide prediction and functional characterization of the genetic basis of autism spectrum disorder. *Nat. Neurosci.* **19**, 1454–1462 (2016).

26. H. Fukasawa, S. Bornheimer, K. Kudlicka, M. G. Farquhar, Slit diaphragms contain tight junction proteins. *J. Am. Soc. Nephrol.* **20**, 1491–1503 (2009).

27. J. Reiser, W. Kriz, M. Kretzler, P. Mundel, The glomerular slit diaphragm is a modified adherens junction. *J. Am. Soc. Nephrol.* **11**, 1–8 (2000).

28. H. Scholz, F. J. Boivin, K. M. Schmidt-Ott, S. Bachmann, K.U. Eckardt, U. I. Scholl, P. B. Persson, Kidney physiology and susceptibility to acute kidney injury: Implications for renoprotection. *Nat. Rev. Nephrol.* **17**, 335–349 (2021).

29. S. Bagnasco, D. Good, R. Balaban, M. Burg, Lactate production in isolated segments of the rat nephron. *Am. J. Physiol.* **248**, F522–526 (1985).

30. R. M. Berne, M. N. Levy, *Physiology* (Mosby-Year Book, ed. 3, 1993), chap. 42.

31. L. S. Costanzo, *Physiology* (Elsevier, ed. 4, 2010), chap. 6.

32. R. Brandes, F. Lang, R. F. Schmidt, *Physiologie des Menschen* (Springer, 2010).

33. K. Rainer, S. Silbernagl, *Lehrbuch der Physiologie* (Georg Thieme, ed. 2, 1996), chap. 12.

34. S. Muto, M. Hata, J. Taniguchi, S. Tsuruoka, K. Moriwaki, M. Saitou, K. Furuse, H. Sasaki, A. Fujimura, M. Imai, E. Kusano, S. Tsukita, M. Furuse, Claudin-2-deficient mice are defective in the leaky and cation-selective paracellular permeability properties of renal PTs. *Proc. Natl. Acad. Sci. U.S.A.* **107**, 8011–8016 (2010).

35. A. S. L. Yu, Paracellular transport and energy utilization in the renal tubule. *Curr. Opin. Nephrol. Hypertens.* **26**, 398–404 (2017).

36. D. B. Mount, Thick ascending limb of the loop of Henle. *Clin. J. Am. Soc. Nephrol.* **9**, 1974–1986 (2014).

37. G. R. Ares, P. A. Ortiz, Constitutive endocytosis and recycling of NKCC2 in rat thick ascending limbs. *Am. J. Physiol. Renal Physiol.* **299**, F1193–1202 (2010).

38. P. S. Caceres, G. R. Ares, P. A. Ortiz, cAMP stimulates apical exocytosis of the renal Na(+)-K(+)-2Cl(−) cotransporter NKCC2 in the thick ascending limb: Role of protein kinase A. *J. Biol. Chem.* **284**, 24965–24971 (2009).

39. I. Giménez, B. Forbush, Short-term stimulation of the renal Na-K-Cl cotransporter (NKCC2) by vasopressin involves phosphorylation and membrane translocation of the protein. *J. Biol. Chem.* **278**, 26946–26951 (2003).

40. J. van der Wijst, H. Belge, R. J. M. Bindels, O. Devuyst, Learning physiology from inherited kidney disorders. *Physiol. Rev.* **99**, 1575–1653 (2019).

41. B. M. Rotoli, A. Barilli, R. Visigalli, F. Ferrari, V. Dall'Asta, y+LAT1 and y+LAT2 contribution to arginine uptake in different human cell models: Implications in the pathophysiology of lysinuric protein intolerance. *J. Cell Mol. Med.* **24**, 921–929 (2020).

42. R. Sano, Y. Shinozaki, T. Ohta, Sodium-glucose cotransporters: Functional properties and pharmaceutical potential. *J Diabetes Investig.* **11**, 770–782 (2020).

43. J. K. Lukowski, A. Pamreddy, D. Velickovic, G. Zhang, L. Pasa-Tolic, T. Alexandrov, K. Sharma, C. R. Anderton; the Kidney Precision Medicine Project, Storage conditions of human kidney tissue sections affect spatial lipidomics analysis reproducibility. *J. Am. Soc. Mass Spectrom.* **31**, 2538–2546 (2020).

44. D. Velickovic, G. Zhang, D. Bezbradica, A. Bhattacharjee, L. Paša-Tolić, K. Sharma, T. Alexandrov, C. R. Anderton; KPMP Consortium, Response surface methodology as a new approach for finding optimal MALDI matrix spraying parameters for mass spectrometry imaging. *J. Am. Soc. Mass Spectrom.* **31**, 508–516 (2020).

45. M. Inuzuka, M. Hayakawa, T. Ingi, Serinc, an activity-regulated protein family, incorporates serine into membrane lipid synthesis. *J. Biol. Chem.* **280**, 35776–35783 (2005).

46. A. H. Merrill Jr, De novo sphingolipid biosynthesis: A necessary, but dangerous, pathway. *J. Biol. Chem.* **277**, 25843–25846 (2002).

47. S. Merscher, A. Fornoni, Podocyte pathology and nephropathy–Sphingolipids in glomerular diseases. *Front Endocrinol.* **5**, 127 (2014).

48. J. P. Slotte, Biological functions of sphingomyelins. *Prog. Lipid Res.* **52**, 424–437 (2013).

49. F. Hullin-Matsuda, T. Taguchi, P. Greimel, T. Kobayashi, Lipid compartmentalization in the endosome system. *Semin. Cell Dev. Biol.* **31**, 48–56 (2014).

50. D. R. Green, Apoptosis and sphingomyelin hydrolysis. The flip side. *J. Cell Biol.* **150**, F5–F8 (2000).

51. P. Drochmans, C. Freudenstein, J. C. Wanson, L. Laurent, T. W. Keenan, J. Stadler, R. Leloup, W. W. Franke, Structure and biochemical composition of desmosomes and tonofilaments isolated from calf muzzle epidermis. *J. Cell Biol.* **79**, 427–443 (1978).

52. K. Shigetomi, Y. Ono, T. Inai, J. Ikenouchi, Adherens junctions influence tight junction formation via changes in membrane lipid composition. *J. Cell Biol.* **217**, 2373–2381 (2018).

53. D. B. Lee, E. Huang, H. J. Ward, Tight junction biology and kidney dysfunction. *Am. J. Physiol. Renal Physiol.* **290**, F20–F34 (2006).

54. L. E. Mickelsen, M. Bolisetty, B. R. Chimileski, A. Fujita, E. J. Beltrami, J. T. Costanzo, J. R. Naparstek, P. Robson, A. C. Jackson, Single-cell transcriptomic analysis of the lateral hypothalamic area reveals molecularly distinct populations of inhibitory and excitatory neurons. *Nat. Neurosci.* **22**, 642–656 (2019).

55. E. Ong, L. L. Wang, J. Schaub, J. F. O'Toole, B. Steck, A. Z. Rosenberg, F. Dowd, J. Hansen, L. Barisoni, S. Jain, I. H. de Boer, M. T. Valerius, S. S. Waikar, C. Park, D. C. Crawford, T. Alexandrov, C. R. Anderton, C. Stoeckert, C. Weng, A. D. Diehl, C. J. Mungall, M. Haendel, P. N. Robinson, J. Himmelfarb, R. Iyengar, M. Kretzler, S. Mooney, Y. He; Kidney Precision Medicine Project, Modelling kidney disease using ontology: Insights from the Kidney Precision Medicine Project. *Nat. Rev. Nephrol.* **16**, 686–696 (2020).

56. T. Stuart, A. Butler, P. Hoffman, C. Hafemeister, E. Papalexi, W. M. Mauck III, Y. Hao, M. Stoeckius, P. Smibert, R. Satija, Comprehensive integration of single-cell data. *Cell* **177**, 1888–1902.e21 (2019).

57. C. S. McGinnis, L. M. Murrow, Z. J. Gartner, DoubletFinder: Doublet detection in single-cell RNA sequencing data using artificial nearest neighbors. *Cell Syst* **8**, 329–337.e4 (2019).

58. S. Black, D. Phillips, J. W. Hickey, J. Kennedy-Darling, V. G. Venkataraaman, N. Samusik, Y. Goltsev, C. M. Schürch, G. P. Nolan, CODEX multiplexed tissue imaging with DNA-conjugated antibodies. *Nat. Protoc.* **16**, 3802–3835 (2021).

59. E. Y. Chen, C. M. Tan, Y. Kou, Q. Duan, Z. Wang, G. V. Meirelles, N. R. Clark, A. Ma'ayan, Enrichr: Interactive and collaborative HTML5 gene list enrichment analysis tool. *BMC Bioinformatics* **14**, 128 (2013).

60. P. T. Brinkkoetter, T. Bork, S. Salou, W. Liang, A. Mizi, C. Özel, S. Koehler, H Henning Hagmann, C. Ising, A. Kuczkowski, S. Schnyder, A. Abed, B. Schermer, T. Benzing, O. Kretz, V. G. Puelles, S. Lagies, M. Schlimpert, B. Kammerer, C. Handschin, C. Schell, T. B. Huber,Anaerobic glycolysis

maintains the glomerular filtration barrier independent of mitochondrial metabolism and dynamics. *Cell Rep* **27**, 1551–1566.e5 (2019).

61. R. F. Schmidt, G. Thews, *Physiologie des Menschen* (Springer, ed. 27, 1997), chap. 35.

62. S. Islam, A. Zeisel, S. Joost, G. la Manno, P. Zajac, M. Kasper, P. Lönnerberg, S. Linnarsson, Quantitative single-cell RNA-seq with unique molecular identifiers. *Nat. Methods* **11**, 163–166 (2014).

63. B. Aevermann, Y. Zhang, M. Novotny, M. Keshk, T. Bakken, J. Miller, R. Hodge, B. Lelieveldt, E. Lein, R. H. Scheuermann, A machine learning method for the discovery of minimum marker gene combinations for cell type identification from single-cell RNA sequencing. *Genome Res.* **31**, 1767–1780 (2021).

64. A. A. Satoskar, *J. P. Shapiro, C. N. Bott, H. Song, G. M. Nadasdy, S. V. Brodsky, L. A. Hebert, D. J. Birmingham, T. Nadasdy, M. A. Freitas, B. H. Rovin*, Characterization of glomerular diseases using proteomic analysis of laser capture microdissected glomeruli. *Mod. Pathol.* **25**, 709–721 (2012).

65. J. P. Shapiro, S. Biswas, A. S. Merchant, A. Satoskar, C. Taslim, S. Lin, B. H. Rovin, C. K. Sen, S. Roy, M. A. Freitas, A quantitative proteomic workflow for characterization of frozen clinical biopsies: Laser capture microdissection coupled with label-free mass spectrometry. *J. Proteomics* **77**, 433–440 (2012).

66. S. Winfree, S. Khan, R. Micanovic, M. T. Eadon, K. J. Kelly, T. A. Sutton, C. L. Phillips, K. W. Dunn, T. M. el-Achkar, Quantitative three-dimensional tissue cytometry to study kidney tissue and resident immune cells. *J. Am. Soc. Nephrol.* **28**, 2108–2118 (2017).

67. Y. Goltsev, N. Samusik, J. Kennedy-Darling, S. Bhate, M. Hale, G. Vazquez, S. Black, G. P. Nolan, Deep profiling of mouse splenic architecture with CODEX multiplexed imaging. *Cell* **174**, 968–981.e15 (2018).

68. A. Palmer, P. Phapale, I. Chernyavsky, R. Lavigne, D. Fay, A. Tarasov, V. Kovalev, J. Fuchser, S. Nikolenko, C. Pineau, M. Becker, T. Alexandrov, FDR-controlled metabolite annotation for high-resolution imaging mass spectrometry. *Nat. Methods* **14**, 57–60 (2017).

69. P. Bhargava, R. G. Schnellmann, Mitochondrial energetics in the kidney. *Nat. Rev. Nephrol.* **13**, 629–646 (2017).

70. K. Wang, B. Kestenbaum, Proximal tubular secretory clearance: A neglected partner of kidney function. *Clin. J. Am. Soc. Nephrol.* **13**, 1291–1296 (2018).

71. R. P. L. van Swelm, J. F. M. Wetzels, D. W. Swinkels, The multifaceted role of iron in renal health and disease. *Nat. Rev. Nephrol.* **16**, 77–98 (2020).

72. A. Zarjou, S. Bolisetty, R. Joseph, A. Traylor, E. O. Apostolov, P. Arosio, J. Balla, J. Verlander, D. Darshan, L. C. Kuhn, A. Agarwal, Proximal tubule H-ferritin mediates iron trafficking in acute kidney injury. *J. Clin. Invest.* **123**, 4423–4434 (2013).

73. D. Legouis, A. Faivre, P. E. Cippa, S. de Seigneux, Renal gluconeogenesis: An underestimated role of the kidney in systemic glucose metabolism. *Nephrol. Dial. Transplant.* **2020**, gfaa302 (2020).

74. T. Nakagawa, R. J. Johnson, A. Andres-Hernando, C. Roncal-Jimenez, L. G. Sanchez-Lozada, D. R. Tolan, M. A. Lanaspa, Fructose production and metabolism in the kidney. *J. Am. Soc. Nephrol.* **31**, 898–906 (2020).

75. C. Meyer, V. Nadkarni, M. Stumvoll, J. Gerich, Human kidney free fatty acid and glucose uptake: Evidence for a renal glucose-fatty acid cycle. *Am. J. Physiol.* **273**, E650–E654 (1997).

76. S. Minami, T. Yamamoto, Y. Takabatake, A. Takahashi, T. Namba, J. Matsuda, T. Kimura, J.Y. Kaimori, I. Matsui, T. Hamano, H. Takeda, M. Takahashi, Y. Izumi, T. Bamba, T. Matsusaka, F. Niimura, Y. Isaka, Lipophagy maintains energy homeostasis in the kidney proximal tubule during prolonged starvation. *Autophagy* **13**, 1629–1647 (2017).

77. R. J. Wanders, H. R. Waterham, Biochemistry of mammalian peroxisomes revisited. *Annu. Rev. Biochem.* **75**, 295–332 (2006).

78. S. M. Houten, S. Violante, F. V. Ventura, R. J. Wanders, The biochemistry and physiology of mitochondrial fatty acid β-oxidation and its genetic disorders. *Annu. Rev. Physiol.* **78**, 23–44 (2016).

79. H. M. Kang, S. H. Ahn, P. Choi, Y.A. Ko, S. H. Han, F. Chinga, A. S. D. Park, J. Tao, K. Sharma, J. Pullman, E. P. Bottinger, I. J. Goldberg, K. Susztak, Defective fatty acid oxidation in renal tubular epithelial cells has a key role in kidney fibrosis development. *Nat. Med.* **21**, 37–46 (2015).

80. K. Strijbis, F. M. Vaz, B. Distel, Enzymology of the carnitine biosynthesis pathway. *IUBMB Life* **62**, 357–362 (2010).

81. C. Faul, K. Asanuma, E. Yanagida-Asanuma, K. Kim, P. Mundel, Actin up: Regulation of podocyte structure and function by components of the actin cytoskeleton. *Trends Cell Biol.* **17**, 428–437 (2007).

82. M. G. Márquez, N. O. Favale, F. Leocata Nieto, L. G. Pescio, N. Sterin-Speziale, Changes in membrane lipid composition cause alterations in epithelial cell-cell adhesion structures in renal papillary collecting duct cells. *Biochim. Biophys. Acta* **1818**, 491–501 (2012).

83. S. J. Schunk, J. Floege, D. Fliser, T. Speer, WNT–β-catenin signalling—A versatile player in kidney injury and repair. *Nat. Rev. Nephrol.* **17**, 172–184 (2021).

84. S. K. Mallipattu, J. C. He, The beneficial role of retinoids in glomerular disease. *Front. Med.* **2**, 16 (2015).

85. Y. Zhao, Q. Li, Q. Ouyang, L. Wu, X. Chen, Activated mesangial cells acquire the function of antigen presentation. *Cell. Immunol.* **361**, 104279 (2021).

86. L. Zuo, W. T. Kuo, J. R. Turner, Tight junctions as targets and effectors of mucosal immune homeostasis. *Cell. Mol. Gastroenterol. Hepatol.* **10**, 327–340 (2020).

87. G. Gamba, W. Wang, L. Schild, Sodium chloride transport in the loop of Henle, distal convoluted tubule, and collecting duct, in *Seldin and Giebisch's The Kidney*, R. J. Alpern, O. W. Moe, M. Caplan, Eds. (Academic Press, ed. 5, 2013), pp. 1143–1179.

88. A. Guillermo, A. Luis Reuss, in *Seldin and Giebisch's The Kidney*, R. J. Alpern, O. W. Moe, M. Caplan, Eds. (Academic Press, ed. 5, 2013), pp. 95–120.

89. S. Nielsen, A. B. Maunsbach, C. A. Ecelbarger, M. A. Knepper, Ultrastructural localization of Na-K-2Cl cotransporter in thick ascending limb and macula densa of rat kidney. *Am. J. Physiol.* **275**, F885–893 (1998).

90. Y. Maeoka, J. A. McCormick, NaCl cotransporter activity and Mg^{2+} handling by the distal convoluted tubule. *Am. J. Physiol. Renal Physiol.* **319**, F1043–F1053 (2020).

91. A. S. L. Yu, F. Hanner, J. Peti-Peterdi, in *Seldin and Giebisch's The Kidney*, R. J. Alpern, O. W. Moe, M. Caplan, Eds. (Academic Press, ed. 5, 2013), pp. 347–368.

92. C. Gao, P. J. Higgins, W. Zhang, AQP2: Mutations associated with congenital nephrogenic diabetes insipidus and regulation by post-translational modifications and protein-protein interactions. *Cell* **9**, 2172 (2020).

93. P. J. Fuller, M. J. Young, Mechanisms of mineralocorticoid action. *Hypertension* **46**, 1227–1235 (2005).

94. L. L. Hamm, N. Nakhoul, K. S. Hering-Smith, Acid-base homeostasis. *Clin. J. Am. Soc. Nephrol.* **10**, 2232–2242 (2015).

95. V. Saxena, H. Gao, S. Arregui, A. Zollman, M. M. Kamocka, X. Xuei, P. McGuire, M. Hutchens, T. Hato, D. S. Hains, A. L. Schwaderer, Kidney intercalated cells are phagocytic and acidify internalized uropathogenic *Escherichia coli*. *Nat. Commun.* **12**, 2405 (2021).

96. C. Klasen, K. Ohl, M. Sternkopf, I. Shachar, C. Schmitz, N. Heussen, E. Hobeika, E. Levit-Zerdoun, K. Tenbrock, M. Reth, J. Bernhagen, O. el Bounkari, MIF promotes B cell chemotaxis through the receptors CXCR4 and CD74 and ZAP-70 signaling. *J. Immunol.* **192**, 5273–5284 (2014).

97. H. Fan, P. Hall, L. L. Santos, J. L. Gregory, G. Fingerle-Rowson, R. Bucala, E. F. Morand, M. J. Hickey, Macrophage migration inhibitory factor and CD74 regulate macrophage chemotactic responses via MAPK and Rho GTPase. *J. Immunol.* **186**, 4915–4924 (2011).

98. Z. S. Zang, Y. M. Xu, A. T. Y. Lau, Molecular and pathophysiological aspects of metal ion uptake by the zinc transporter ZIP8 (SLC39A8). *Toxicol Res* **5**, 987–1002 (2016).

99. M. J. Nielsen, H. J. Moller, S. K. Moestrup, Hemoglobin and heme scavenger receptors. *Antioxid. Redox Signal.* **12**, 261–273 (2010).